

UNIVERSITY OF CALGARY

Estimating Heavy Oil Viscosity from Seismic Data

by

Fereidoon Vasheghani Farahani

A THESIS

SUBMITTED TO THE FACULTY OF GRADUATE STUDIES
IN PARTIAL FULFILMENT OF THE REQUIREMENTS FOR THE
DEGREE OF DOCTOR OF PHILOSOPHY

DEPARTMENT OF GEOSCIENCE

CALGARY, ALBERTA

APRIL, 2011

© Fereidoon Vasheghani Farahani 2011



UNIVERSITY OF
CALGARY

The author of this thesis has granted the University of Calgary a non-exclusive license to reproduce and distribute copies of this thesis to users of the University of Calgary Archives.

Copyright remains with the author.

Theses and dissertations available in the University of Calgary Institutional Repository are solely for the purpose of private study and research. They may not be copied or reproduced, except as permitted by copyright laws, without written authority of the copyright owner. Any commercial use or re-publication is strictly prohibited.

The original Partial Copyright License attesting to these terms and signed by the author of this thesis may be found in the original print version of the thesis, held by the University of Calgary Archives.

Please contact the University of Calgary Archives for further information:

E-mail: uarc@ucalgary.ca

Telephone: (403) 220-7271

Website: <http://archives.ucalgary.ca>

Abstract

Heavy oils are viscoelastic material; therefore, their shear properties influence the seismic response and should not be ignored. Heavy oil viscosity, among other parameters, controls the attenuation of seismic waves which is measured in terms of quality factor Q . BISQ, a poroviscoelastic model that couples the effects of simultaneous Biot and squirt flow mechanisms, is used to relate Q to the fluid viscosity. The variation of quality factor with respect to fluid viscosity, as predicted by BISQ, matches the laboratory measurements.

Quality factor is a measurable seismic attribute. Higher frequency data are more favourable for Q estimation. Crosswell seismic data from a heavy oil reservoir is used for estimating Q . Travel time tomography followed by attenuation tomography yields the quality factor. The resulting Q tomogram can be converted into the viscosity tomogram if the remaining reservoir parameters are known. Such parameters are populated for the zone of interest using the geostatistical methods from the available log and core data at borehole locations.

Existing BISQ equations can only take one fluid phase into account. However, the porous reservoir rock is saturated with bitumen and water. A slightly modified version of the BISQ relations is used in order to accommodate the presence of a second fluid phase. The estimated viscosity tomogram shows ambiguity because for every given quality factor, more than one viscosity value can be calculated.

Despite the ambiguity, the methodology introduced in this study demonstrates that seismic data have the potential to be used for estimation of fluid viscosity in heavy oil reservoirs, although further research is needed to improve the workflow.

Acknowledgements

I would like to give my special thanks to my supervisor, Dr. Larry Lines, for his great mentorship and supervision throughout my graduate studies. The technical feedback from my other supervisory committee members, Dr. John Bancroft and Dr. Tony Settari is much appreciated.

I would like to thank the Consortium for Heavy Oil Research by University Scientists (CHORUS) and its industry sponsors and also the Alberta Ingenuity Centre for In-situ Energy (AICISE) for supporting this study. Schlumberger offered technical assistance and provided full access to its resources during this research which is appreciated. I would like to thank Dr. Bob Godfrey and Dr. Tom Morgan for their technical support. I would also like to thank Laricina Energy for providing the crosswell seismic data.

I want to thank Joan Embleton for her help as the CHORUS manager during this research, and my friends and colleagues for sharing their ideas with me through discussions.

Lastly, I want to thank my family for being supportive of my education. Their vision of this accomplishment formed 21 years ago, when I started grade one, and their unconditional support and passion have been uninterrupted ever since.

Dedication

To my family.

Table of Contents

Approval Page.....	ii
Abstract.....	iii
Acknowledgements.....	iv
Dedication.....	v
Table of Contents.....	vi
List of Tables.....	viii
List of Figures and Illustrations.....	ix
List of Symbols, Abbreviations and Nomenclature.....	xii
CHAPTER ONE: INTRODUCTION.....	1
CHAPTER TWO: THE WAVE EQUATION.....	8
2.1 Stress.....	8
2.2 Strain.....	10
2.2.1 Dilatation.....	12
2.3 Stress-Strain relationship.....	12
2.3.1 Isotropic medium.....	14
2.4 Equation of motion.....	14
2.5 Wave equation.....	15
2.5.1 Gassmann’s equations.....	16
2.6 Viscoelastic theory.....	18
2.7 Quality factor and frequency.....	23
CHAPTER THREE: POROVISCOELASTICITY.....	25
3.1 Biot’s theory.....	25
3.2 Squirt flow.....	29
3.3 BISQ.....	30
3.3.1 Reference frequency.....	33
3.3.2 Low frequency BISQ.....	33
3.4 Quality factor and frequency.....	34
3.5 Quality factor and viscosity.....	36
3.5.1 Quality factor and temperature.....	37
3.6 Quality factor and permeability.....	40
3.7 Quality factor and mobility.....	41
CHAPTER FOUR: EFFECTS OF ATTENUATION ON SEISMIC RESPONSE.....	44
4.1 Quality factor, amplitude and frequency.....	44
4.2 Quality factor and reflection coefficient.....	48
4.3 Estimation of Q.....	53
4.3.1 Spectral ratio.....	53
4.3.2 Centroid frequency shift.....	54
CHAPTER FIVE: ESTIMATING VISCOSITY FROM CROSSWELL SEISMIC DATA.....	57
5.1 Methodology.....	57

5.2 Tomography	58
5.2.1 Travel time tomography	58
5.2.2 Attenuation tomography	62
5.3 Estimating reservoir properties	64
5.3.1 Kriging	65
5.3.2 Sequential Gaussian simulation	66
5.4 BISQ inversion	66
CHAPTER SIX: CASE STUDY	68
6.1 Geology of the area	69
6.2 Crosswell seismic data	71
6.3 Well data	75
6.4 Tomography	77
6.5 Reservoir parameters	82
6.5.1 Reservoir model preparation	84
6.5.2 Porosity and permeability	85
6.5.3 Bulk and shear moduli	87
6.5.4 Effect of water	90
6.6 Viscosity tomogram	98
6.7 Sensitivity analysis	101
CHAPTER SEVEN: CONCLUSIONS	104
7.1 Future work recommendations	106
7.1.1 Physical models	106
7.1.2 Velocity analysis	107
REFERENCES	109

List of Tables

Table 3-1: Reservoir parameters used for generating the graph of quality factor versus frequency shown in Figure 3-2.	35
Table 3-2: Reservoir parameters used for generating the graph of quality factor versus viscosity shown in Figure 3-3.	36
Table 3-3: Reservoir parameters used for generating the graph of quality factor versus permeability shown in Figure 3-6.	40
Table 3-4: Reservoir parameters used for generating the graph of quality factor versus mobility shown in Figure 3-7.	42
Table 4-1: The maximum amplitude and the frequency of maximum amplitude for the Ricker wavelets modeled at different central frequencies (at the source and receiver locations).	47
Table 4-2: Model properties (from Lines et al., 2008).	49
Table 4-3: Calculated amplitude and phase of the reflection coefficients.	50
Table 6-1: Available core and log data.	76
Table 6-2: Reservoir parameters required as input values for BISQ inversion.	83
Table 6-3: Total volume of each rock component in a unit bulk volume.	84
Table 6-4: The values assumed for the reservoir rock and fluid properties.	85
Table 6-5: Total volume of each rock component in a unit bulk volume.	94
Table 6-6: The base case parameters used in the sensitivity analysis.	102

List of Figures and Illustrations

Figure 1-1: Effect of the vertical viscosity heterogeneity on the simulated productivity of a SAGD operation (from Larter et al., 2008).....	3
Figure 1-2: The workflow for estimating viscosity from seismic data.	6
Figure 2-1: Traction and unit normal vectors.	9
Figure 2-2: Displacements in the medium due to applied stress.	11
Figure 2-3: A spring representing an elastic component.	13
Figure 2-4: A dashpot representing the viscous component.	19
Figure 2-5: Zener model or standard linear solid model.....	20
Figure 2-6: Variation of quality factor with frequency in a Zener element, calculated from $Q_0 = 6.463$ and $\omega_0 = 50\pi$ Hz.	24
Figure 3-1: The representative cylinder with the radius equal to the characteristic squirt flow length (modified from Dvorkin and Nur, 1993).	31
Figure 3-2: Variation of quality factor with frequency predicted by BISQ theory, computed from the reservoir parameters given in Table 3-1.	35
Figure 3-3: Variation of quality factor with fluid viscosity predicted by BISQ theory, computed from the reservoir parameters given in Table 3-2.	37
Figure 3-4: Variation of the shear wave quality factor (red curve) with temperature for extracted oil and rock with oil, measured in the lab (from Behura et al., 2007).	38
Figure 3-5: The effect of constant and variable fluid bulk modulus on attenuation (from Eastwood, 1983).	39
Figure 3-6: Variation of quality factor with permeability predicted by BISQ theory, computed from the reservoir parameters given in Table 3-3.	41
Figure 3-7: Variation of quality factor with mobility predicted by BISQ theory, computed from the reservoir parameters given in Table 3-4.	43
Figure 4-1: The amplitude spectra of the Ricker wavelet at the source location (solid blue) and the receiver location (dashed red), modeled with central frequency of 50 Hz.	46

Figure 4-2: The amplitude spectra of the Ricker wavelet at the source location (solid blue) and the receiver location (dashed red) modeled with central frequency of 100 Hz.	46
Figure 4-3: Two layer geological models showing model (1): contrast in impedance and model (2): contrast in attenuation (from Lines et al., 2008).	50
Figure 4-4: The finite difference seismic responses of the models shown in Figure 3-3 (from Lines et al., 2008).	51
Figure 4-5: Normally incident reflections from three different boundaries. Left: impedance boundary, middle: attenuation boundary, right: impedance and attenuation boundary (from Lines et al., 2008).....	52
Figure 4-6: Crosswell survey configuration. Direct, reflected and refracted rays traveling from source to receiver.	56
Figure 5-1: The workflow for estimating viscosity from crosswell seismic data.	57
Figure 5-2: Total travel time for a ray is the sum of travel times in each cell.	60
Figure 5-3: The area between the wells is divided into layers. Chebyshev polynomials describe the velocity in each layer (Modified from Washbourne et al., 2002).....	61
Figure 5-4: In kriging, neighboring cells are used to estimate an unknown value. The weight of each adjacent cell on the final estimate is proportional to its distance from the unknown cell.	65
Figure 6-1: Athabasca oil sands located in the north eastern part of the province of Alberta in Canada.	68
Figure 6-2: The schematic cross section of the Western Canadian Sedimentary Basin across the Athabasca region (Modified from Zhou et al., 2008). Arrows show the migration paths of the heavy oils from source rock to the reservoirs.	69
Figure 6-3: The regional stratigraphy of the Athabasca oil sands (modified from Wightman et al., 1995).....	70
Figure 6-4: Crosswell survey geometry (schematic).	71
Figure 6-5: Ray density map (straight ray direct arrivals).....	72
Figure 6-6: Common receiver gather, receiver depth: 205 m.	73
Figure 6-7: Signal (top) and its amplitude spectrum (bottom).	74
Figure 6-8: Base map. The configuration of the available wells relative to the source and receiver wells (wells 8 and 9, respectively).	75

Figure 6-9: The log and core data available at the source well (well 8).....	77
Figure 6-10: The log and core data available at the receiver well (well 9).	78
Figure 6-11: The velocity tomogram. The velocity dispersion observed at the well bore is because of the difference between sonic and crosswell seismic frequencies.	79
Figure 6-12: Velocity dispersion observed at the oil sands interval. Circles represent VSP derived interval velocities and the curve shows the sonic log velocity. (from Schmitt, 1999).....	80
Figure 6-13: The attenuation tomogram.	81
Figure 6-14: Q tomogram. The distinct red zone near the top of the tomogram (depth interval 178 m – 188 m) corresponds to the cap rock shales.	82
Figure 6-15: Map view (top) and cross section (bottom) of reservoir porosity.....	86
Figure 6-16: Map view (top) and cross section (bottom) of reservoir permeability.....	87
Figure 6-17: Shale volume logs at the source and receiver wells.....	88
Figure 6-18: Map view (top) and cross section (bottom) of shale volume.	90
Figure 6-19: Map view (top) and cross section (bottom) of water saturation.	91
Figure 6-20: Model A: dry frame saturated with water and bitumen. Model B: wet frame saturated with bitumen.....	92
Figure 6-21: Relative permeability curves for water and oil in an oil-water system.....	95
Figure 6-22: The Hashin-Shtrikman bounds of a two phase medium and the corresponding schematic upper and lower bound curves.	96
Figure 6-23: Viscosity tomogram generated using the left (decreasing) side of the BISQ curves.	100
Figure 6-24: Viscosity tomogram generated using the right (increasing) side of the BISQ curves.	100
Figure 6-25: Sensitivity plot corresponding to the left side of the BISQ curve.	103
Figure 6-26: Sensitivity plot corresponding to the right side of the BISQ curve.	103
Figure 7-1: Variation of P-wave velocity with viscosity predicted by BISQ theory, computed from the reservoir parameters given in Table 3-2.	107

List of Symbols, Abbreviations and Nomenclature

Symbol	Definition
a	<i>Acceleration</i>
a	<i>Biot coefficient</i>
\tilde{a}	<i>Pore size parameter</i>
e	<i>Strain</i>
f	<i>Frequency</i>
k	<i>Permeability</i>
l	<i>Length</i>
m	<i>Mass</i>
n	<i>Unit normal vector</i>
p	<i>Pressure</i>
q	<i>Flow rate</i>
s	<i>Slowness</i>
t	<i>Time</i>
u	<i>Particle displacement</i>
\dot{u}	<i>Particle velocity</i>
v	<i>Wave velocity</i>
A	<i>Flow area</i>
D	<i>Dilatation</i>
E	<i>Energy</i>
F	<i>Force</i>
K	<i>Bulk modulus</i>
L	<i>Length</i>
M	<i>Mobility</i>
M_R	<i>Relaxed modulus</i>
\bar{M}	<i>Complex modulus</i>
Q	<i>Quality factor</i>
R	<i>Characteristic squirt flow length</i>
S	<i>Saturation</i>
\bar{S}	<i>Surface</i>
T	<i>Time</i>
Tr	<i>Traction</i>
U	<i>Amplitude</i>
V	<i>Volume</i>
α	<i>Attenuation factor</i>
α_0	<i>Attenuation coefficient</i>
δ	<i>Kronecker delta</i>
ε	<i>Rotation</i>
φ	<i>Porosity</i>
η	<i>Viscosity</i>

Symbol	Definition
κ	<i>Complex wave number</i>
$\bar{\kappa}$	<i>Wave number</i>
λ	<i>Lamé Constant</i>
$\bar{\lambda}$	<i>Wave length</i>
μ	<i>Lamé Constant (shear modulus)</i>
ρ	<i>Density</i>
σ	<i>Stress</i>
τ	<i>Relaxation time</i>
$\tilde{\tau}$	<i>Tortuosity</i>
ω	<i>Angular frequency</i>

Chapter One: Introduction

Elevated energy prices and higher demands for hydrocarbon have increased the focus of the oil and gas industry on the unconventional resources such as heavy oils or shale gas reservoirs. Unconventional resources impose complicated challenges which require unconventional measures for exploration, delineation and production. One challenge with the heavy oils, which are abundantly found in Alberta, Canada, is the higher oil viscosities. The viscosity of such oils is in the range of tens of thousand to several million centipoise. These viscosities are several orders of magnitude greater than the viscosity of the conventional oils.

The main implication with heavy oils is that such fluids are practically immobile at the original reservoir condition and therefore, more energy is required to produce such oils. As a comparison, the viscosity of pure water is 1 cp and the viscosity of honey is around 10,000 cp. One could imagine how difficult it is to drink honey using a straw as compared to drinking water.

In order to make the production of the heavy oils possible, the viscosity has to be lowered. This is usually done by heating the oil in-situ. Viscosity of the heavy oil decreases as the temperature increases. The amount of heat required to mobilize the oil to a degree that it is commercially producible depends on the original viscosity of the oil at reservoir conditions. The heat is added to the reservoir by injecting steam into the reservoir in processes such as SAGD (steam assisted gravity drainage) or CSS (cyclic steam stimulation). In SAGD, two horizontal wells are drilled above one another, about five meters apart, near the bottom of the reservoir. Steam is injected through the upper well, and the heated and mobile oil is produced from the lower well. The heated oil drains

toward the production well at the edges of the steam zone. In CSS, there are three consecutive stages. First the steam is injected into the reservoir without any production. Next, the injection is stopped and the reservoir is left to absorb the heat from the steam. Finally, the well is opened to production until there is no mobile oil in the vicinity of the well. These steps are repeated in a cyclic manner. Other extraction methods include VAPEX (vapour extraction) in which a solvent is used to reduce the heavy oil viscosity in the reservoir, or THAI (toe to heel air injection) where the heavier components of the oil are burnt in-situ using combustion methods in order to heat the bitumen and upgrade it into lighter oil.

The main purpose of all of the above mentioned recovery methods is to mobilize the oil by reducing its viscosity. The performance of such production scenarios depends on the understanding of the variation of the heavy oil viscosity within the reservoir. Flow of the fluids in porous media is governed by Darcy's law. In a linear, one dimensional flow of an incompressible fluid, in steady state conditions, the Darcy's law for a single fluid component in a porous media can be written as

$$q = \frac{kA}{\eta_f} \frac{dp}{dx}, \quad (1.1)$$

where in the above, q is the flow rate, k is the permeability, A is the flow area, η_f is the fluid viscosity and dp/dx is the pressure gradient along the flow path. In this case, the flow rate, or production rate, is inversely proportional to viscosity. For a complex reservoir with various degrees of heterogeneity, the flow regimes are complicated and the

effect of each parameter on the production rate can be analyzed through computer reservoir simulation.

In a recent study (Larter et al., 2008), it is shown that the vertical heterogeneity in the heavy oil viscosity can decrease the oil production by a factor of two. In other words, ignoring the heterogeneity of the heavy oil viscosity can lead to over estimation of the production rate or similarly the cumulative oil production, by a factor of two (Figure 1-1).

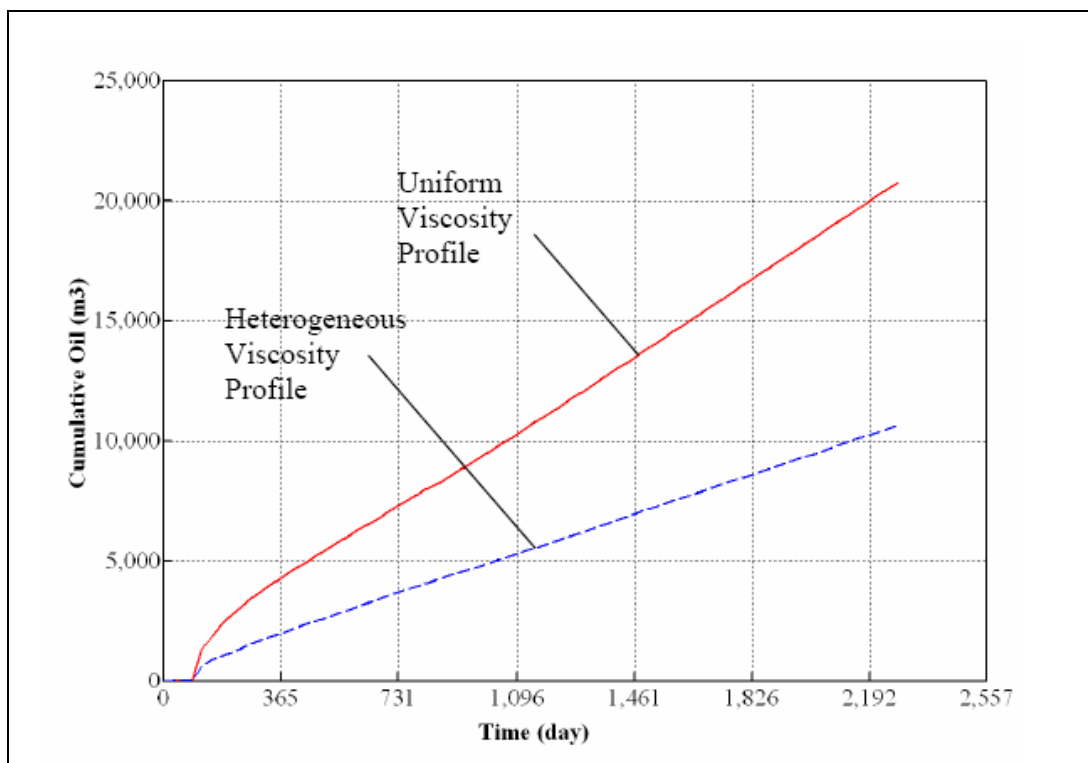


Figure 1-1: Effect of the vertical viscosity heterogeneity on the simulated productivity of a SAGD operation (from Larter et al., 2008).

Viscosity can be estimated from well data through well testing analysis, or it can be measured in the lab from fluid samples. However, availability of such data on the reservoir scale is very limited and these sources of information provide a few data points

over a large area. Seismic data, on the other hand, are acquired on a larger scale than well data and therefore provide a valuable reservoir characterization potential. Whether seismic response is sensitive enough to the shear properties of the fluids or not should be assessed before seismic data can be used for the purpose of viscosity estimation.

Viscosity is a measure of fluid's resistance to flow. The higher the viscosity, the more energy is required to move the fluid. In a simple one dimensional case, when a film of fluid is placed between two parallel plates, where the bottom plate is fixed and the top plate is moving at a constant speed \dot{u} , the shear stress σ_s is a function of the velocity gradient in the fluid. This can be written in the form of equation (1.2):

$$\sigma_s = f\left(\frac{d\dot{u}}{dy}\right). \quad (1.2)$$

The simplest scenario for equation (1.2) is when the shear stress and the velocity gradient are linearly proportional through a constant of proportionality, C :

$$\sigma_s = C \frac{d\dot{u}}{dy}. \quad (1.3)$$

In the case of ideal fluids, the constant of proportionality is zero, which means that ideal fluids do not support shear. However, this constant cannot be ignored for real fluids. For the Newtonian fluids equation (1.2) will be written as

$$\sigma_s = \eta_f \frac{d\dot{u}}{dy}, \quad (1.4)$$

where η_f is the fluid viscosity.

Traditionally in seismic rock physics, it is assumed that shear modulus of the fluids is zero, or fluids do not support shear. While the assumption of zero or negligible fluid shear modulus is accepted for fluids with lower viscosities such as conventional oils or water, it might not be an appropriate approach in the case of heavy oils of Alberta. This topic has gained more attention in recent years and researchers have conducted modeling analyses and lab measurements to understand the effects of the shear properties of the fluids on seismic response.

Nur et al. (1984) studied the effect of temperature on velocity and attenuation of seismic waves. Schmitt (1999) observed that over a heavy oil interval, there is a difference between the sonic log velocities and VSP interval velocities. In a study by Watson et al. (2001), elastic wave velocities were used for delineating the steam zones in a heavy oil reservoir. Shear wave velocity in heavy oil reservoirs was measured and analyzed in Han et al. (2005). Batzle et al. (2005, 2006a, and 2006b) measured velocity and attenuation of seismic waves in heavy oils. Behura et al. (2007) explained the shear properties of the heavy oils, and Best et al. (2008) related the attenuation of high frequency seismic waves to the pore fluid viscosity. Most of the measurements in the above mentioned studies are in the sonic or ultrasonic frequency range.

In this thesis, the objective is to investigate a workflow for estimating heavy oil viscosity from seismic data using the attenuation of seismic waves. The main question that is going to be answered is:

“Do seismic data have the potential to be used for estimating the viscosity of heavy oils?”

Figure 1-2 illustrates the workflow used in this study. The three major steps involved in this process are shown schematically. Quality factor, which is inversely proportional to attenuation, should be estimated from seismic data. Reservoir rock and fluid properties are also required and can be estimated from the well log or core data. Once these parameters are known, the BISQ relations can be used for calculating the viscosity of the reservoir fluid.

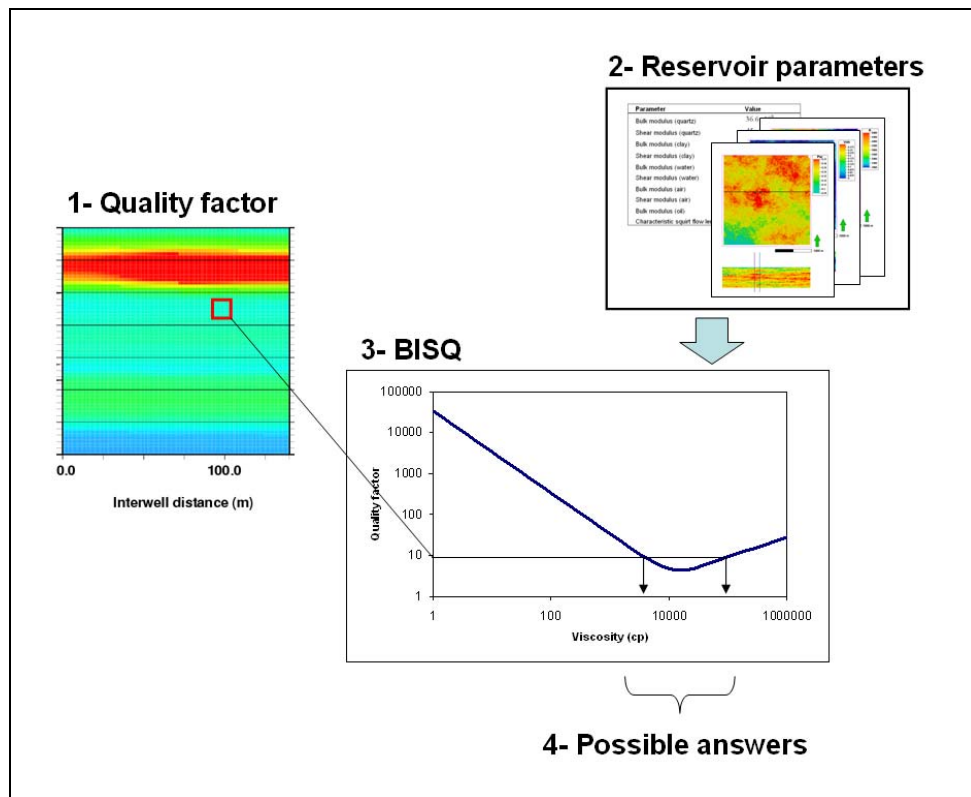


Figure 1-2: The workflow for estimating viscosity from seismic data.

In Chapter 2, the seismic wave equation is explained and the insufficiency of the existing elastic models for fluid characterization is discussed. Also, it is shown that while viscoelastic models can be used to establish a relationship between viscous properties of

the reservoir material and the seismic response, they cannot be used for estimating the viscosity of pore fluids. In Chapter 3, the effects of viscosity on the attenuation of seismic waves are shown through the use of poroviscoelastic relations. In this chapter, it is explained that poroviscoelastic models consider the fluid and solid properties separately and therefore are ideal for seismic characterization of pore fluids. In Chapter 4, the effects of attenuation on seismic response are summarized and the best seismic data candidate for the viscosity estimation is identified. A workflow for estimating viscosity from seismic data is introduced in Chapter 5, and it is tested on a real data set in Chapter 6. Finally, the conclusions of the current research and a few recommendations for future work are given in Chapter 7.

Chapter Two: The wave equation

The wave equation is a partial differential equation that describes the propagation of waves in the material in terms of particle displacement. In order to derive the wave equation, two constitutive equations are required: equation of motion (Newton's second law of motion), and a stress-strain relationship (generalized Hooke's law).

2.1 Stress

If an element of force $d\mathbf{F}$ is acting on an element of surface $d\bar{S}$ in an arbitrary direction, the force per unit surface is defined as traction \mathbf{Tr} :

$$\mathbf{Tr} = \frac{d\mathbf{F}}{d\bar{S}}. \quad (2.1)$$

\mathbf{Tr} varies with position on the surface and can be written as

$$\mathbf{Tr} = \mathbf{Tr}(\mathbf{n}) = \mathbf{Tr}(n_1, n_2, n_3), \quad (2.2)$$

where \mathbf{n} is the unit vector normal to the surface (Figure 2-1).

The simplest relationship between the components of traction and components of vector \mathbf{n} is a linear relationship:

$$Tr_1 = an_1 + bn_2 + cn_3, \quad (2.3)$$

where a , b and c are parameters whose values vary with location in space (Krebes, 2004).

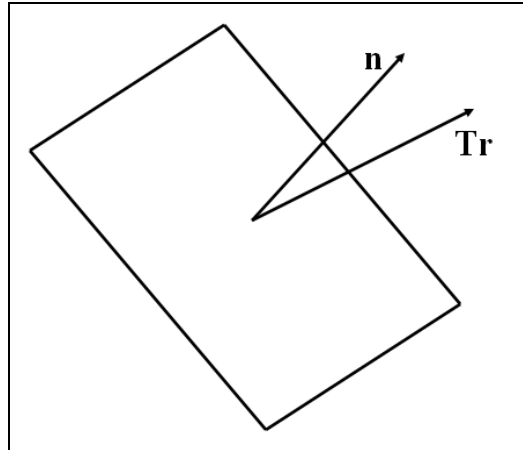


Figure 2-1: Traction and unit normal vectors.

There are three components of traction which will result in nine such parameters. If they are denoted by σ_{ij} , $i, j = 1, 2, 3$, then equation (2.3) can be written in the following matrix form:

$$\begin{bmatrix} Tr_1 \\ Tr_2 \\ Tr_3 \end{bmatrix} = \begin{bmatrix} \sigma_{11} & \sigma_{12} & \sigma_{13} \\ \sigma_{21} & \sigma_{22} & \sigma_{23} \\ \sigma_{31} & \sigma_{32} & \sigma_{33} \end{bmatrix} \begin{bmatrix} n_1 \\ n_2 \\ n_3 \end{bmatrix}, \quad (2.4)$$

or similarly

$$Tr_i = \sum_{j=1}^3 \sigma_{ij} n_j, \quad i = 1, 2, 3. \quad (2.5)$$

The three by three matrix given in equation (2.4) is called the stress tensor.

Components σ_{11} , σ_{22} and σ_{33} are called the normal stresses and the other components are called the shear stresses. Out of these nine components, six are independent. This is due to the following symmetries in the stress tensor (Aki and Richards, 2002):

$$\sigma_{12} = \sigma_{21}, \quad \sigma_{13} = \sigma_{31}, \quad \sigma_{23} = \sigma_{32}. \quad (2.6)$$

2.2 Strain

When stress is applied to an element of volume, the element undergoes two forms of deformation. In one type, the sides of the unit will change in length. This will result in a change in the volume of the unit but the shape of the unit will not necessarily change. In the other form of deformation, the sides of the unit will change orientation. This will result in the change in the shape of the unit; however, the volume of the unit will not necessarily change. The strain tensor therefore consists of components describing the relative linear displacements and components describing the relative angular displacements.

Considering points A and B , infinitesimally close in a medium, as shown in Figure 2-2, where point A is located at $\mathbf{x} = (x_1, x_2, x_3)$ and point B is located at $\mathbf{x} + d\mathbf{x}$, under applied stress, point A moves to A' and point B moves to B' . Figure 2-2 illustrates that not only the length of the vector connecting the two points has changed after the displacements, but also its orientation has changed. This is summarized in the properties of the vector $d\mathbf{u}$ which can be written as

$$du_i(\mathbf{x}) = \sum_{j=1}^3 \frac{\partial u_i}{\partial x_j} dx_j, \quad i = 1, 2, 3. \quad (2.7)$$

The components du_i can be re-written in the following format:

$$du_i = \sum_{j=1}^3 (e_{ij} - \varepsilon_{ij}) dx_j, \quad i = 1, 2, 3, \quad (2.8)$$

where

$$e_{ij} = \frac{1}{2} \left(\frac{\partial u_i}{\partial x_j} + \frac{\partial u_j}{\partial x_i} \right), \quad (2.9)$$

and

$$\varepsilon_{ij} = \frac{1}{2} \left(\frac{\partial u_j}{\partial x_i} - \frac{\partial u_i}{\partial x_j} \right). \quad (2.10)$$

The e_{ij} components form a three by three matrix which is called the strain tensor.

e_{11} , e_{22} and e_{33} are called the normal strains and the other components are the shear strains.

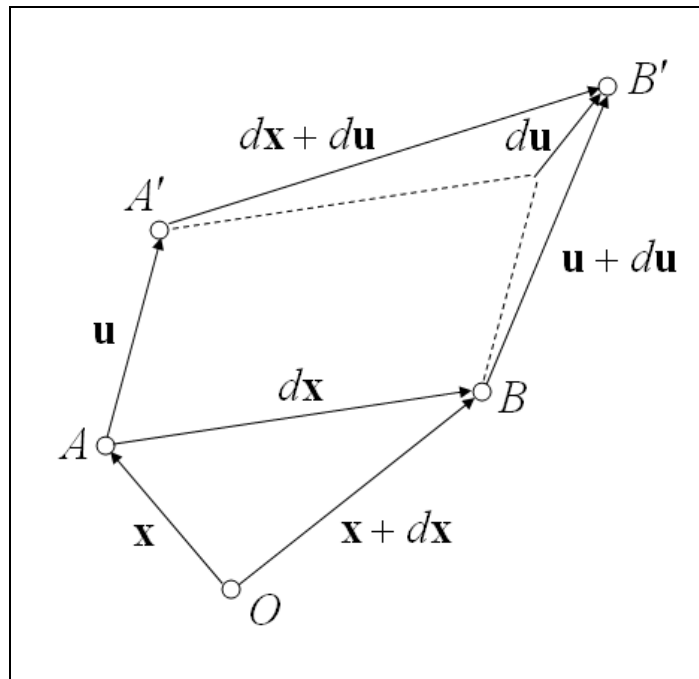


Figure 2-2: Displacements in the medium due to applied stress.

Similar to the stress tensor, there are only six independent components in the strain tensor which is due to the following symmetries (Aki and Richards, 2002):

$$e_{12} = e_{21}, \quad e_{13} = e_{31}, \quad e_{23} = e_{32}. \quad (2.11)$$

2.2.1 Dilatation

The change in the volume of the unit relative to the initial volume is called the dilatation. If the volume is infinitesimally small, then the dilatation can be calculated as total relative change in the lengths of the sides of the unit, which are in turn given by the normal strains. It can be written as

$$D = \nabla \cdot \mathbf{u} = e_{11} + e_{22} + e_{33}. \quad (2.12)$$

Positive D represents an increase in volume while negative dilatation corresponds to a reduction in volume.

2.3 Stress-Strain relationship

For relatively small stresses and strains, strain is linearly related to the applied stress (Slawinski, 2003). In a simple example, the length of a spring changes when a force is applied to the spring. Hooke's law states that the relative change in the length of the spring with respect to its original length is proportional to the applied force or stress.

The generalization of Hooke's law for a linearly elastic material will result in the following linear relationship between each stress tensor component σ_{ij} and all components of strain tensor e_{ij} :

$$\sigma_{ij} = \sum_{k=1}^3 \sum_{l=1}^3 c_{ijkl} e_{kl}, \quad i, j = 1, 2, 3. \quad (2.13)$$

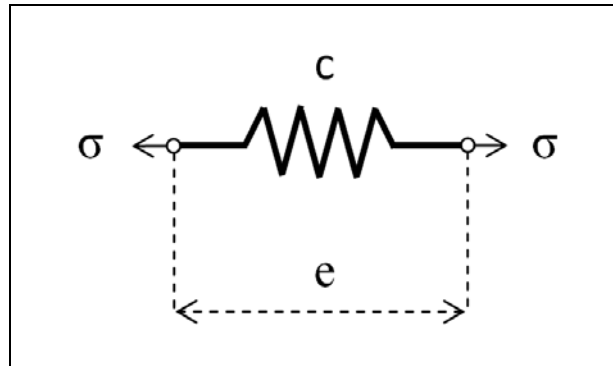


Figure 2-3: A spring representing an elastic component.

Figure 2-3 shows a component that responds elastically to the changes in the stresses and therefore is governed by equation (2.13). The quantities c_{ijkl} are called elastic constants and form the elasticity tensor of rank four. Since there are nine stress components, each linearly related to nine strain components, there are 81 elastic constants in total; however, due to the following symmetries, only 21 of them are independent. The rest can be derived from these 21 independent ones.

$$c_{ijkl} = c_{jikl}, \quad c_{ijkl} = c_{ijlk}, \quad c_{ijkl} = c_{klij}. \quad (2.14)$$

Using the above symmetries and the definition of strain given in equation (2.9) it can be shown that the stress-strain relation in equation (2.13) can be re-written as:

$$\sigma_{ij} = \sum_{k=1}^3 \sum_{l=1}^3 c_{ijkl} \frac{\partial u_l}{\partial x_k}, \quad i, j = 1, 2, 3. \quad (2.15)$$

The stress-strain relation allows us to link fundamental principles of wave propagation to the elastic properties of material.

2.3.1 Isotropic medium

In an isotropic medium, the physical properties are the same in all directions. For an isotropic medium, the elastic constants can be calculated as:

$$c_{ijkl} = \lambda \delta_{ij} \delta_{kl} + \mu (\delta_{ik} \delta_{jl} + \delta_{il} \delta_{jk}), \quad (2.16)$$

where λ and μ are known as Lamé constants and δ_{ij} is called the Kronecker delta.

$\delta_{ij} = 0$ when $i \neq j$ and $\delta_{ij} = 1$ when $i = j$. This means that in an isotropic elastic medium, the behavior of the material can be fully described using only two independent elastic parameters. Substituting equation (2.16) in equation (2.13), the stress-strain relation for an elastic isotropic material is given by:

$$\sigma_{ij} = \lambda D \delta_{ij} + 2\mu e_{ij}, \quad i, j = 1, 2, 3, \quad (2.17)$$

where D is the dilatation.

2.4 Equation of motion

Equation of motion describes the motion of a given volume when it is subject to stresses and strains that vary in time and space. Newton's second law of motion is used for this purpose:

$$\mathbf{F} = m\mathbf{a}, \quad (2.18)$$

Where \mathbf{F} is the force acting on a body with mass m , and \mathbf{a} is the acceleration resulting from force \mathbf{F} . The force acting on the unit volume, dV , is the sum of all the tractions acting on the surface of the unit volume and the body forces acting on the body of a medium, such as gravity. Therefore equation (2.18) can be written in an integral form as:

$$\int_{\bar{S}} \sum_{j=1}^3 \sigma_{ij} n_j d\bar{S} + \int_V F_i dV = \int_V \rho \frac{\partial^2 u_i}{\partial t^2} dV, \quad i=1,2,3, \quad (2.19)$$

where the first term denotes the sum of the tractions and the second term is the sum of all the body forces. Using the definition of traction (equation 2.5) and the Gauss's divergence theorem, after some algebraic calculations, the equation of motion can be written as:

$$\sum_{j=1}^3 \frac{\partial \sigma_{ij}}{\partial x_j} + F_i = \rho \frac{\partial^2 u_i}{\partial t^2}, \quad i=1,2,3. \quad (2.20)$$

These equations are called Cauchy's equations of motion (Slawinski, 2003).

2.5 Wave equation

Equations (2.17) and (2.20) provide a coupled set of equations that relate the displacement of particles to the applied stress. A fundamental attribute of the wave motion is that the energy is transmitted in the form of particle displacement, and therefore there is no net transfer of mass. It is common to use these equations separately to model the propagation of waves in a medium. Substituting equation (2.17) into equation (2.20), and assuming that the body forces are negligible, the equation of motion for homogeneous isotropic elastic medium is obtained as:

$$(\lambda + \mu) \frac{\partial D}{\partial x_i} + \mu \nabla^2 u_i = \rho \frac{\partial^2 u_i}{\partial t^2}, \quad i=1,2,3, \quad (2.21)$$

or in the vector form:

$$(\lambda + \mu) \nabla (\nabla \cdot \mathbf{u}) + \mu \nabla^2 \mathbf{u} = \rho \frac{\partial^2 \mathbf{u}}{\partial t^2}. \quad (2.22)$$

The P- and S-wave equations can be separated by taking the divergence and curl of equation (2.22), respectively. Taking the divergence, the P-wave equation is obtained as:

$$(\lambda + 2\mu)\nabla^2 D = \rho \frac{\partial^2 D}{\partial t^2}. \quad (2.23)$$

These waves travel at the speed of:

$$v_p = \sqrt{\frac{\lambda + 2\mu}{\rho}}. \quad (2.24)$$

Taking the curl of equation (2.22) will result in the following equation for the S-waves:

$$\mu\nabla^2 (\nabla \times \mathbf{u}) = \rho \frac{\partial^2}{\partial t^2} (\nabla \times \mathbf{u}), \quad (2.25)$$

which propagate with the speed of:

$$v_s = \sqrt{\frac{\mu}{\rho}}. \quad (2.26)$$

2.5.1 Gassmann's equations

Lamé's constants define the speed of the waves in the media, however, in order to perform reservoir characterization, they have to be linked to the properties of saturated porous media. Gassmann (1951) used the shear and bulk moduli to relate the effective properties of saturated material to the properties of the solid porous frame and the fluids inside the pores. While the shear modulus μ is one of the original Lamé's constants, the bulk modulus is related to the Lamé's constants through the following relation:

$$K = \lambda + \frac{2}{3}\mu. \quad (2.27)$$

In the derivation of Gassmann's equations, it is assumed that the shear properties of the fluids do not influence the overall shear properties of the saturated medium and therefore, the shear modulus of the saturated rock is the same as shear modulus of the dry rock, or

$$\mu_{sat} = \mu_{fr}, \quad (2.28)$$

where subscripts *sat* and *fr* represent saturated rock and dry frame, respectively. On the other hand, the bulk modulus of the saturated rock is related to the bulk moduli of its constituents using the following equation:

$$K_{sat} = K_{fr} + \frac{\left(1 - \frac{K_{fr}}{K_m}\right)^2}{\frac{\varphi}{K_f} + \frac{1-\varphi}{K_m} - \frac{K_{fr}}{K_m^2}}, \quad (2.29)$$

where K_m , K_f and K_{fr} are the grain, fluid and the dry frame bulk moduli, respectively, and φ is porosity. The density of the saturated porous medium can be calculated using the porosity weighted arithmetic average of the fluid and solid densities:

$$\rho_{sat} = (1-\varphi)\rho_m + \varphi\rho_f, \quad (2.30)$$

where ρ_f and ρ_m are fluid and grain densities, respectively.

Using equations (2.28) to (2.30), the seismic wave velocities (equations 2.24 and 2.26) of the fluid saturated media can be related to the elastic properties of the fluid and solid components in the porous media. However, in this case, the relationships are only expressed in terms of the elastic properties of the fluids, and therefore, such relations cannot be used for directly estimating the viscosity of the pore fluid.

2.6 Viscoelastic theory

Equations (2.23) and (2.25) represent the P- and S-wave equations for a homogeneous isotropic elastic medium. The effects of heterogeneity, anisotropy and anelasticity can be introduced into the wave equation by using proper stress-strain relationships.

Hooke's law in the lossless case was used to derive the elastic wave equation. The mechanical element in the derivation of the Hooke's law, shown in Figure 2-3, is assumed to be fully elastic, acting similar to a spring. The response of a spring to the changes in stress is instantaneous. Some materials do not behave elastically. For example heavy oils are viscoelastic material (Behura et al., 2007). Therefore, in addition to the elastic component, another mechanical element is needed for modeling the behavior of such materials.

Viscoelastic behavior is a time dependent, mechanical non-instantaneous response of a material body to variations of applied stress (Carcione, 2007). That means the response of the medium to stress is not immediate and the delay is due the viscous behavior of the material. It is said that the material has memory. A good example of a viscoelastic response is the suspension system of a vehicle. There is a spring which acts as the elastic part and a shock absorber which absorbs the energy and imposes a delay in the elastic response. Figure 2-4 illustrates a dashpot (viscous component).

To formulate the viscoelastic behavior, rock physicists have used springs and dashpots as the components of viscoelasticity. Response of the dashpot component to the applied stress is given as:

$$\sigma_{ij} = \sum_{k=1}^3 \sum_{l=1}^3 \eta_{ijkl} \frac{\partial e_{kl}}{\partial t}, \quad i, j = 1, 2, 3, \quad (2.31)$$

where η is the viscosity of the medium. Presence of time derivative in equation (2.31) demonstrates that the viscous response is time dependant.

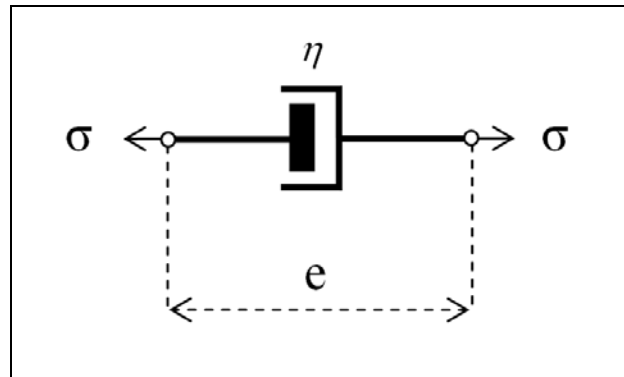


Figure 2-4: A dashpot representing the viscous component.

Different configurations of the elastic and viscous components are available for viscoelastic studies. Three of the main models widely used for different applications are Maxwell, Kelvin-Voigt and Zener models. In the Maxwell model, one spring and one dashpot are connected in series. The stresses applied on spring and dashpot are identical and equal to the total stress but they produce different deformations. The total deformation of the system is the sum of the deformations of the spring and the dashpot. In Kelvin-Voigt model one spring and one dashpot are connected in parallel. In this model, the deformations of components are the same and equal to the total deformation, but the stresses applied to the spring and dashpot are different. A combination of a spring and a Kelvin-Voigt model, connected in series, will create the Zener model (Figure 2-5).

This model, introduced by Poynting and Thomson (1902), is the most appropriate model for studying the real earth and is also known as the standard linear solid model (Carcione, 2007).

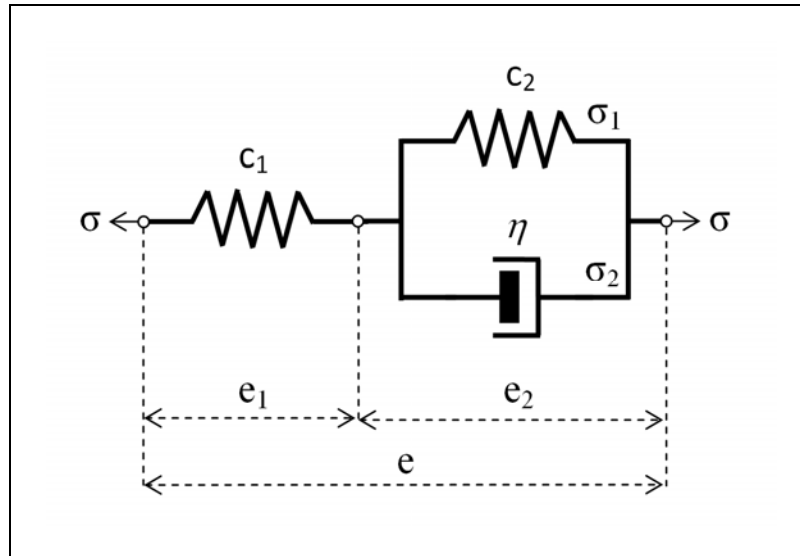


Figure 2-5: Zener model or standard linear solid model.

The stress-strain relations for the elements of this model, in the one dimensional case, are given as:

$$\begin{aligned}\sigma &= c_1 e_1 \\ \sigma_1 &= c_2 e_2 \\ \sigma_2 &= \eta \frac{\partial e_2}{\partial t}\end{aligned}\quad (2.32)$$

Also, from the configuration of the elements, the relationship between fractional and total stresses and strains are as follows:

$$\sigma = \sigma_1 + \sigma_2, \quad e = e_1 + e_2. \quad (2.33)$$

The stress-strain relation for the Zener component is obtained by the solution of the above equations:

$$\sigma + \tau_{\sigma} \frac{\partial \sigma}{\partial t} = M_R \left(e + \tau_e \frac{\partial e}{\partial t} \right), \quad (2.34)$$

where τ_{σ} and τ_e are relaxation times:

$$\begin{aligned} \tau_e &= \frac{\eta}{c_2}, \\ \tau_{\sigma} &= \frac{\eta}{c_1 + c_2}, \end{aligned} \quad (2.35)$$

and M_R is the relaxed modulus and is given by:

$$M_R = \frac{c_1 c_2}{c_1 + c_2}. \quad (2.36)$$

Taking the Fourier transform of equation (2.34) yields the complex and frequency dependant modulus that relates stress to strain:

$$\sigma = \bar{M}(\omega) e, \quad (2.37)$$

where ω is the angular frequency and

$$\bar{M}(\omega) = M_R \left(\frac{1 + i\omega\tau_e}{1 + i\omega\tau_{\sigma}} \right). \quad (2.38)$$

A complex and frequency dependant modulus will result in a complex and frequency dependant velocity. This means that different frequencies travel at different velocities. This phenomenon is called velocity dispersion and the medium under such conditions is called dispersive.

In a viscoelastic medium, due to the presence of internal friction, the propagating waves experience a frequency dependant energy loss as well (Krebes, 2004). Such a medium is called a dissipative medium. Dissipation can be quantified by a parameter called the quality factor, Q . The quality factor is the inverse of the dissipation factor and therefore the lower the Q , the greater the dissipation. The quality factor is defined as (Aki and Richards, 2002):

$$Q = \frac{\text{Re}(\bar{M}(\omega))}{\text{Im}(\bar{M}(\omega))}. \quad (2.39)$$

Substituting the complex modulus given in equation (2.38) in equation (2.39), and using the definitions of the relaxation times given in equation (2.35), the quality factor for the Zener model can be derived as:

$$Q(\omega) = \frac{1 + \omega^2 \tau_e \tau_\sigma}{\omega(\tau_e - \tau_\sigma)}. \quad (2.40)$$

This equation shows how the quality factor, which is a measureable seismic attribute, can be related to the viscosity of the viscoelastic medium. It is important to know that this viscosity is different from the viscosity of the fluid inside the pores because in the derivation of this equation, the combined effects of fluid and solid parts are considered. Therefore, while this model proves that the seismic response is sensitive to viscosity, it does not provide us with a tool for fluid viscosity characterization.

Quality factor in equation (2.40) reaches its minimum when the frequency is

$$\omega_0 = \frac{1}{\tau_0} = \frac{1}{\sqrt{\tau_e \tau_\sigma}}. \quad (2.41)$$

ω_0 is called the characteristic frequency, τ_0 is the characteristic relaxation time. The quality factor at $\omega = \omega_0$ is called characteristic quality factor Q_0 . Relaxation times for the Zener element (equation 2.35) can be written as functions of characteristic relaxation time and quality factor (Carcione, 2007):

$$\begin{aligned}\tau_e &= \frac{\tau_0}{Q_0} \left(\sqrt{Q_0^2 + 1} + 1 \right) = \frac{1}{Q_0 \omega_0} \left(\sqrt{Q_0^2 + 1} + 1 \right) \\ \tau_\sigma &= \frac{\tau_0}{Q_0} \left(\sqrt{Q_0^2 + 1} - 1 \right) = \frac{1}{Q_0 \omega_0} \left(\sqrt{Q_0^2 + 1} - 1 \right).\end{aligned}\tag{2.42}$$

From equations (2.40) and (2.42), it is concluded that knowledge of the characteristic frequency and characteristic quality factor is sufficient for relating Q to frequency.

2.7 Quality factor and frequency

The variation in the quality factor of a Zener element with angular frequency is shown in Figure 2-6. For this graph, it is assumed that $Q_0 = 6.463$ and $\omega_0 = 50\pi$ Hz. The quality factor decreases with frequency at frequencies less than the characteristic frequency and increases afterward. Such behavior is in agreement with the experimental results (Zener, 1948).

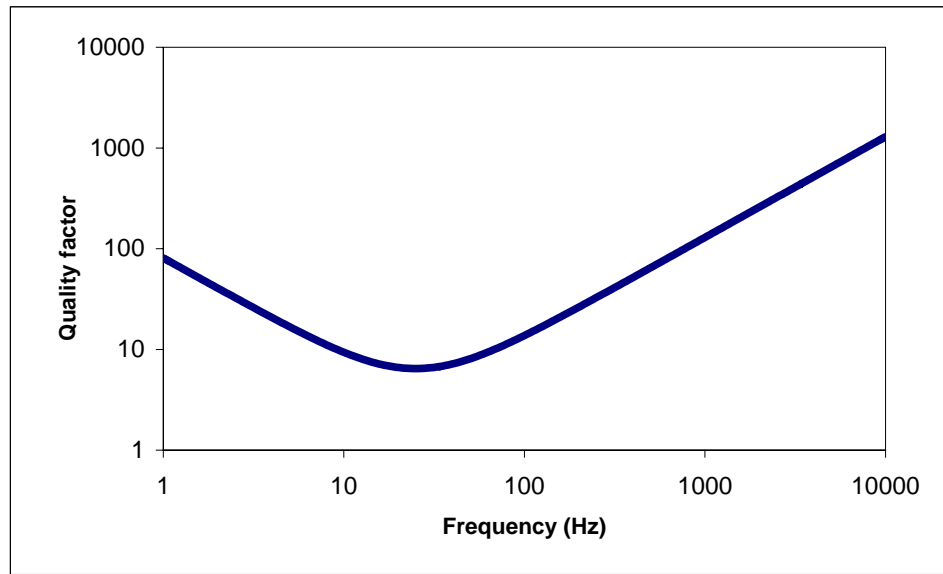


Figure 2-6: Variation of quality factor with frequency in a Zener element, calculated from $Q_0 = 6.463$ and $\omega_0 = 50\pi$ Hz.

Chapter Three: Poroviscoelasticity

In Chapter 2, the effects of viscosity on the attenuation of seismic waves were explained. The response of a viscoelastic material is non instantaneous and frequency dependant. The viscoelastic theory is insufficient for the modeling and inversion studies of heavy oils because the material properties such as elastic parameters and viscosity are combined into an effective medium's properties in this theory. That means it is not possible to distinguish between the fluid properties and rock properties using viscoelastic approach. In order to perform a full scale reservoir analysis that aims to characterize or monitor the fluids in the reservoir, it is required that the properties of fluid and rock are taken into account separately.

A reservoir rock is generally formed of porous frame as the host with fluids in the pores. Laboratory measurements show that heavy oils are viscoelastic materials (Eastwood, 1993; Han et al., 2007) which have non-negligible shear modulus and support shear wave propagation (Das and Batzle, 2008). When a rock is saturated with heavy oils, its behavior becomes viscoelastic consequently (Behura et al., 2007).

3.1 Biot's theory

Biot (1962) explained the theory of propagation of stress waves in the medium for elastic porous frame filled with viscous fluid. In his theory, the solid part is assumed to behave perfectly elastically. In a perfectly elastic medium, loss of energy due to friction does not occur; therefore, in Biot's theory, losses caused by solid frame are ignored (Wyllie et al., 1962). Another assumption is that the fluid is compressible and can flow relative to the solid frame. The motion of the fluid particles is formulated using the

Navier-Stokes equations (Mavko et al., 2003). Similar to the equation of motion in the solid phase, the Newton's second law of motion is used in the derivation of the Navier-Stokes equations. In the Biot's model, the fluid is forced to participate in an oscillatory motion by viscous forces and inertial coupling (Dvorkin and Nur, 1993). This motion will cause friction hence the energy will be lost in the form of heat. Biot's theory predicts that two forms of compressional waves and one rotational wave will be generated.

The two compressional waves travel at different speeds. The faster wave is the standard classical P-wave which shows little dispersion and attenuation compared to the slower P-wave. The slow P-wave propagates in the form of a diffusion wave at low frequencies and its velocity approaches zero at low frequencies. As frequency increases, this wave takes the form of a propagating wave (Dutta and Odé, 1979).

In Biot's theory, it is shown that rocks behave differently at high and low frequencies. These frequencies are separated by characteristic frequency or reference frequency which depends on the rock and fluid properties.

$$\omega_c = \frac{\eta_f \varphi}{k \rho_f}, \quad (3.1)$$

where in this equation η_f is fluid viscosity, k is permeability, φ is porosity and ρ_f is fluid density.

Velocities and attenuations for the entire frequency band can be obtained from the roots of the dispersion relations given by (Mavko et al., 2003):

$$\begin{aligned} \left(\frac{H}{v_p^2} - \rho_{sat} \right) \left(\hat{q} - \frac{\hat{M}}{v_p^2} \right) - \left(\rho_f - \frac{C}{v_p^2} \right) \left(\frac{C}{v_p^2} - \rho_f \right) &= 0 \\ \hat{q} \left(\rho_{sat} - \frac{\mu_{fr}}{v_s^2} \right) - \rho_f^2 &= 0 \end{aligned} \quad (3.2)$$

The terms in these equations are

$$H = K_{fr} + \frac{4}{3} \mu_{fr} + \frac{(K_m - K_{fr})^2}{(\hat{D} - K_{fr})}$$

$$C = \frac{(K_m - K_{fr}) K_m}{(\hat{D} - K_{fr})}$$

$$\hat{M} = \frac{K_m^2}{(\hat{D} - K_{fr})}$$

$$\hat{D} = K_m \left[1 + \varphi \left(\frac{K_m}{K_f} - 1 \right) \right]$$

$$\rho_{sat} = (1 - \varphi) \rho_m + \varphi \rho_f$$

$$\hat{q} = \frac{\tilde{\tau} \rho_f}{\varphi} - \frac{i \eta_f f(\zeta)}{\omega k}$$

$$f(\zeta) = \frac{\zeta^2 h(\zeta)}{4\zeta + i8\zeta h(\zeta)}$$

$$h(\zeta) = \frac{e^{\frac{i3\pi}{4}} J_1\left(\zeta e^{-\frac{i\pi}{4}}\right)}{J_0\left(\zeta e^{-\frac{i\pi}{4}}\right)}$$

$$\zeta = \left(\frac{\omega \tilde{a}^2 \rho_f}{\eta_f} \right),$$

where in these equations K_m , K_f and K_{fr} are the grain, fluid and the dry frame bulk moduli, respectively. μ_{fr} is the dry frame shear modulus, $\tilde{\tau}$ is tortuosity, \tilde{a} is a pore size parameter, J_n is Bessel function of order n , and ω is angular frequency. ρ_m and ρ_f represent grain and fluid densities, respectively, and ϕ is porosity.

Complex roots of the dispersion relations given in equation (3.2) are as follows

$$\frac{1}{v_p^2} = \frac{-(H\hat{q} + \hat{M}\rho_{sat} - 2C\rho_f) \pm \sqrt{(H\hat{q} + \hat{M}\rho_{sat} - 2C\rho_f)^2 - 4(C^2 - \hat{M}H)(\rho_f^2 - \rho_{sat}\hat{q})}}{2(C^2 - \hat{M}H)} \quad (3.3)$$

$$\frac{1}{v_s^2} = \frac{\hat{q}\rho_{sat} - \rho_f^2}{\hat{q}\mu_{fr}}, \quad (3.4)$$

Equation (3.3) represents two roots, designated by \pm , which correspond to the fast and slow P-waves. The real and imaginary parts of the complex roots give the velocity and attenuation of the seismic waves, respectively.

Biot's theory alone is not able to explain the high attenuations and velocity dispersions observed during the monitoring of fluid viscosity using well logs or laboratory velocity measurements (Dvorkin et al., 1994).

Another phenomenon that affects the attenuation and velocity dispersion is the squirt flow mechanism. For most crustal rocks, the effect of squirt flow mechanism is comparable with or greater than the Biot's dispersion effect as explained by Mavko and Nur (1979).

3.2 Squirt flow

Pore aspect ratio specifies the shape of the pores and is calculated as the ratio of the smallest dimension to the largest dimension of the pores. For spherical pores, the aspect ratio is equal to one while for small cracks, this ratio could be as low as 10^{-5} (Toksöz et al., 1976). When pressure is applied to a porous material saturated with fluids, pores with lower aspect ratio undergo a bigger change in volume; therefore the fluid inside such cracks has to flow toward the pores with higher aspect ratio. Such flow will affect the viscoelastic behavior of the saturated rock. This mechanism will result in much higher velocity dispersion and attenuation than those predicted by Biot's theory.

The description of squirt flow mechanism is based on the microscopic properties of rocks, while the scope of reservoir characterization requires that the behavior of the rock be related to the macroscopic and measureable properties of the saturated rock. It is possible to treat these two effects (Biot and squirt flow mechanisms) separately and independent of each other, however, these modes of solid-fluid interaction are interconnected and they simultaneously influence each other and the process of seismic wave propagation (Dvorkin and Nur, 1993).

3.3 BISQ

Dvorkin and Nur (1993) developed an integrated Biot plus squirt flow theory or BISQ. In this theory both mechanisms are simultaneously considered and the poroelastic behavior of rocks is related to measurable and macroscopic reservoir and fluid properties such as porosity, permeability, viscosity, compressibility, and density. Formulation of BISQ is based on uniaxial stress conditions, and explains the effect of reservoir parameters on P-wave attributes. These influences are all frequency dependent.

Figure 3-1 illustrates a cylinder that represents the unit volume with its axis parallel to the direction of P-wave propagation. The radius of the cylinder is equivalent to the characteristic squirt flow length. This length is the effective distance that produces the same squirt effect identical to the cumulative effect of pores of different sizes and shapes in the cylinder. This property cannot be measured directly and should be determined experimentally. It is assumed that this parameter is a fundamental property of the rock and does not depend on the frequency or fluid properties.

This concept is similar to that of absolute permeability of rocks. Absolute permeability is a fundamental property of rocks and does not depend on the fluid properties or pressure. On the other hand, permeability cannot be directly measured and should be estimated using the Darcy's law of fluid flow in porous media.

As shown in Figure 3-1, the fluid motion parallel to the P-wave propagation creates the Biot flow effect and the traverse motion generates the squirt flow effect. The combined Biot-Squirt flow effects results in the following equations for fast P-wave velocity and quality factor:

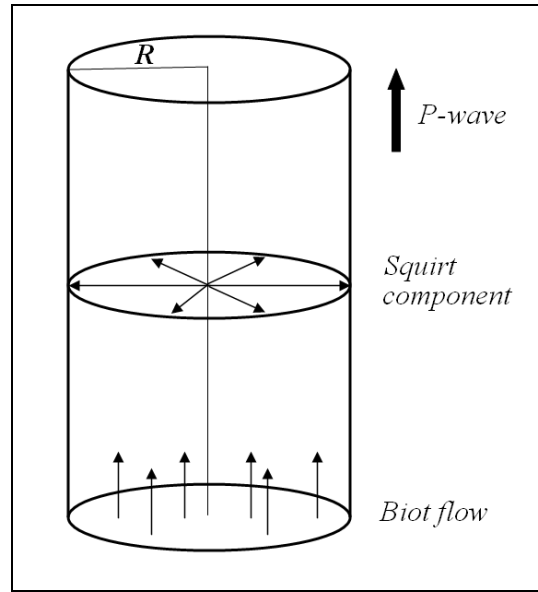


Figure 3-1: The representative cylinder with the radius equal to the characteristic squirt flow length (modified from Dvorkin and Nur, 1993).

$$v_p = \frac{1}{\text{Re}(\sqrt{Y})}, \quad (3.5)$$

$$Q = \frac{\text{Re}(\sqrt{Y})}{2 \text{Im}(\sqrt{Y})}, \quad (3.6)$$

where ω_c is the reference frequency given in equation (3.1) and

$$Y = -\frac{B}{2A} - \sqrt{\left(\frac{B}{2A}\right)^2 - \frac{C}{A}} \quad (3.7)$$

$$A = \frac{\varphi \hat{F}_{sq} (K_{fr} + 4/3 \mu_{fr})}{\rho_2^2}$$

$$B = \frac{\hat{F}_{sq} \left(2a - \varphi - \varphi \frac{\rho_1}{\rho_2} \right) - \left(K_{fr} + 4/3 \mu_{fr} + \hat{F}_{sq} \frac{a^2}{\varphi} \right) \left(1 + \frac{\rho_a}{\rho_2} + i \frac{\omega_c}{\omega} \right)}{\rho_2}$$

$$C = \frac{\rho_1}{\rho_2} + \left(1 + \frac{\rho_1}{\rho_2} \right) \left(\frac{\rho_a}{\rho_2} + i \frac{\omega_c}{\omega} \right)$$

$$\hat{F}_{sq} = \hat{F} \left[1 - \frac{2J_1(\gamma R)}{\gamma R J_0(\gamma R)} \right]$$

$$\gamma^2 = \frac{\omega^2}{\hat{F}} \left(\frac{\rho_f \varphi + \rho_a}{\varphi} + i \frac{\omega_c}{\omega} \rho_f \right)$$

$$\rho_1 = (1 - \varphi) \rho_m$$

$$\rho_2 = \varphi \rho_f$$

$$a = 1 - \frac{K_{fr}}{K_m}$$

$$\hat{F} = \frac{1}{\varphi} \left(\frac{\varphi}{K_f} + \frac{1 - \varphi}{K_m} - \frac{K_{fr}}{K_m^2} \right).$$

In these equations a is the Biot coefficient, R is the characteristic squirt flow length, ρ_a is an apparent density introduced by Biot as an internal coupling factor between solid and liquid (Dvorkin et al., 1994). If \hat{F}_{sq} is replaced with \hat{F} in these equations, the result will be reduced to that of the Biot theory expressions.

3.3.1 Reference frequency

In the low frequency range, it is assumed that the motion of the fluid is of laminar Poiseuille type. This assumption is valid only below a specific frequency (Biot, 1962). Reference frequency determines the low frequency range, $\omega \ll \omega_c$, and the high frequency range, $\omega \gg \omega_c$. According to equation (3.1), this reference frequency limit increases with fluid viscosity and porosity, and decreases with fluid density and rock absolute permeability.

In seismic experiments, for typical values of fluid and rock properties, the frequency falls within the low frequency range. For example, in a water saturated rock with $\varphi = 0.3$, $k = 2000 \text{ md}$, $\rho_f = 1000 \text{ kg/m}^3$ and $\eta_f = 1 \text{ cp}$, the low frequency condition is satisfied because

$$\omega_c = 150,000 \text{ Hz}.$$

Common seismic frequencies, which range up to few hundred Hz, are much less than the reference frequency; therefore, the low frequency approximations of BISQ relations can be used which simplify the calculations of P-wave velocity and Q .

3.3.2 Low frequency BISQ

If frequency ω is much smaller than characteristic frequency ω_c , or

$$\frac{\omega_c}{\omega} \gg 1,$$

then equation (3.7) can be simplified to

$$Y = \frac{(1-\varphi)\rho_m + \varphi\rho_f}{K_{fr} + \frac{4}{3}\mu_{fr} + \hat{F}_{sq} \frac{a^2}{\varphi}}, \quad (3.8)$$

where

$$\hat{F}_{sq} = \hat{F} \left[1 - \frac{2J_1(\xi)}{\xi J_0(\xi)} \right],$$

and

$$\xi = \sqrt{\frac{i\omega R^2 \eta_f \varphi}{k\hat{F}}}.$$

This simplified version will be used in this study in order to relate seismic attributes to the reservoir parameters.

3.4 Quality factor and frequency

Variation of quality factor with frequency in the low frequency mode of BISQ theory, for reservoir properties summarized in Table 3-1, is shown in Figure 3-2. Comparison of Figures 3-2 and 2-6 shows that both the BISQ theory of poroviscoelasticity and Zener viscoelastic model generate the same trend in the quality factor of materials. The only difference is that in the poroviscoelastic approach, fluid and solid properties are taken into account separately while in the viscoelastic modeling, the effective (combined) properties of the material are used.

Parameter	Value	Unit
Fluid density	1,000	kg/m^3
Fluid bulk modulus	0.8	GPa
Fluid viscosity	500,000	cp
Fluid saturation	1	
Porosity	0.25	
Permeability	2,000	md
Characteristic length	1	mm
Matrix bulk modulus	35	GPa
Matrix density	2,650	kg/m^3
Dry frame bulk modulus	1.7	GPa
Dry frame shear modulus	1.35	GPa

Table 3-1: Reservoir parameters used for generating the graph of quality factor versus frequency shown in Figure 3-2.

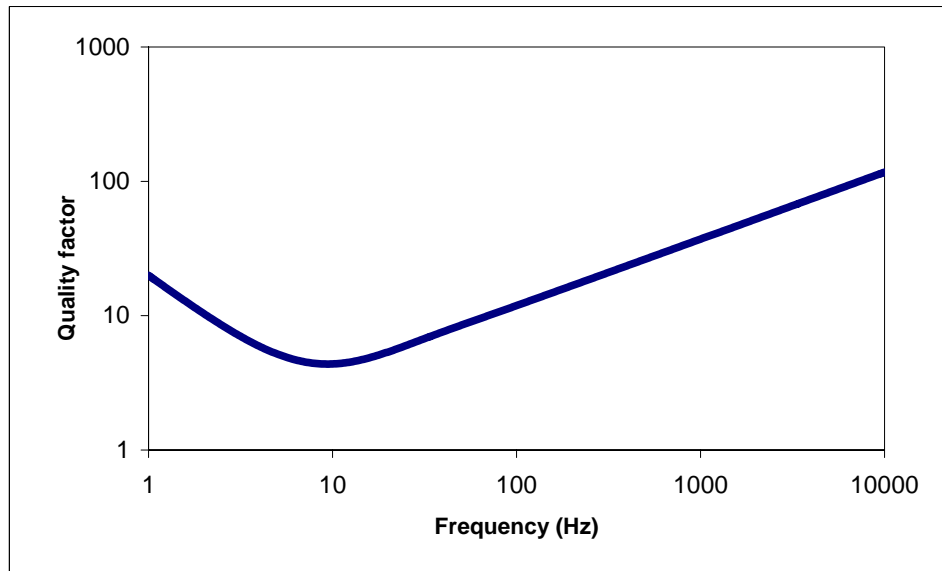


Figure 3-2: Variation of quality factor with frequency predicted by BISQ theory, computed from the reservoir parameters given in Table 3-1.

Between the poroviscoelastic and viscoelastic approaches, the former method appeals more to the heavy oil reservoir characterization because it relates the seismic attributes to the pore fluid viscosity.

3.5 Quality factor and viscosity

Because of the above mentioned advantage of the poroviscoelastic models, changes in the viscosity of the heavy oils in the reservoir can be monitored. Variation of Q with viscosity, given the reservoir parameters summarized in Table 3-2, is shown in Figure 3-3.

The quality factor reaches its minimum at an intermediate viscosity, and increases at higher or lower viscosities. Quality factor is inversely proportional to attenuation. That means at very high quality factors, the attenuation is very low and negligible; therefore, the material acts elastically.

Parameter	Value	Unit
Fluid density	1,000	kg/m^3
Fluid bulk modulus	0.8	GPa
Fluid saturation	1	
Porosity	0.25	
Permeability	2,000	md
Characteristic length	1	mm
Matrix bulk modulus	35	GPa
Matrix density	2,650	kg/m^3
Dry frame bulk modulus	1.7	GPa
Dry frame shear modulus	1.35	GPa
Frequency	300	Hz

Table 3-2: Reservoir parameters used for generating the graph of quality factor versus viscosity shown in Figure 3-3.

In the BISQ theory, it is assumed that the solid frame is elastic and the viscous effect is generated only by the fluids. Figure 3-3 shows that quality factor is high at low and high fluid viscosity values. That means, at these viscosities, the overall behavior of the saturated medium is elastic. In other words, at very low or very high viscosities, fluids behave similar to elastic materials.

3.5.1 Quality factor and temperature

Changes in the viscosity of the fluid during thermal heavy oil production are due to the change in the reservoir temperature. Therefore, researchers have tried to relate the attenuation of seismic waves to temperature (Behura et al., 2007, Eastwood, 1983).

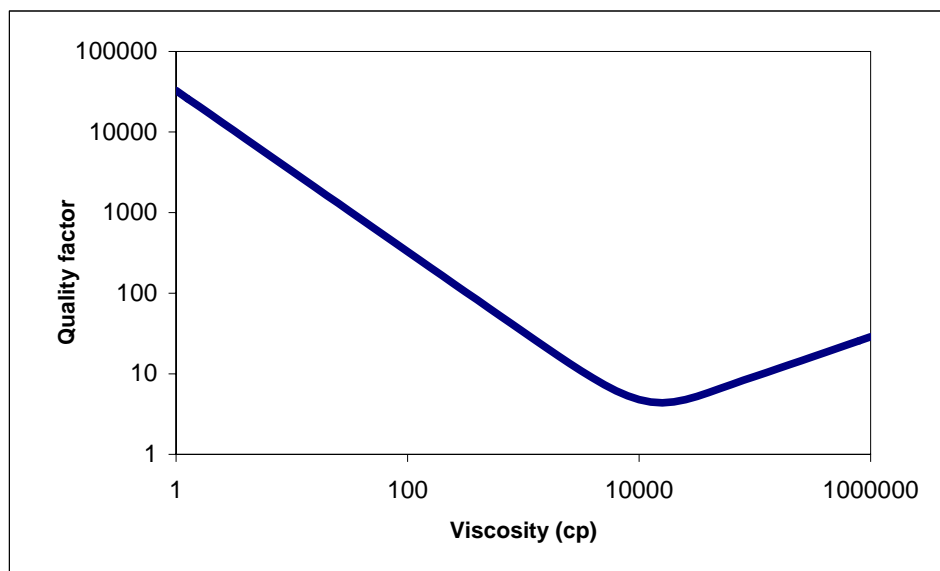


Figure 3-3: Variation of quality factor with fluid viscosity predicted by BISQ theory, computed from the reservoir parameters given in Table 3-2.

The laboratory measurement of quality factor and its variation with temperature is shown in Figure 3-4. The measurements illustrate the same trend as in Figure 3-3.

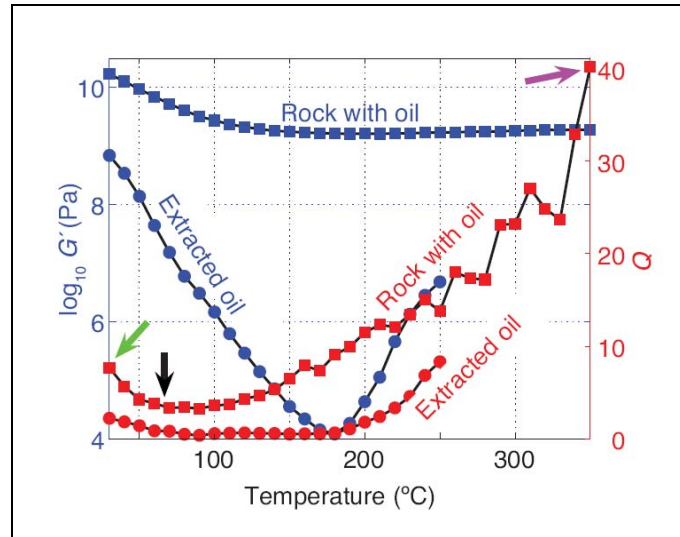


Figure 3-4: Variation of the shear wave quality factor (red curve) with temperature for extracted oil and rock with oil, measured in the lab (from Behura et al., 2007).

Although the laboratory measurements show the changes in shear wave quality factor Q_s with temperature, this curve can be used to validate the trend shown in Figure 3-3. Udías (1999) showed that shear and compressional quality factors are related through the following equation:

$$\frac{Q_s}{Q_p} = \frac{4}{3} \left(\frac{v_s}{v_p} \right)^2, \quad (3.9)$$

therefore, they are linearly proportional to each other. The plot of Q_s versus temperature can be transformed into the plot of Q_p versus temperature by converting the horizontal axes only.

A change in temperature will force the reservoir parameters to change. These parameters include the bulk and shear moduli, density, porosity and fluid viscosity. As explained earlier, changes in the density do not change the attenuation. Also, the effect of

temperature on seismic properties of fluids is greater than its effect on seismic properties of solids (Eastwood, 1983). As such, the change in the solid character is negligible as compared to the change in the fluid character. Ignoring the changes in porosity, the effect of temperature on quality factor can be linked to the changes in the bulk modulus and viscosity of the fluid.

On the other hand, Eastwood (1983) showed that ignoring the variation in the bulk modulus of the fluid, does not dramatically change the trend in the behavior of Q with temperature (Figure 3-5); therefore, the only major influence of the temperature on the quality factor can be modeled with the changes in the viscosity of the fluid. Viscosity decreases when temperature increases, thus moving toward higher temperatures on the x axis in Figure 3-4 is equivalent to moving toward lower viscosities in Figure 3-3.

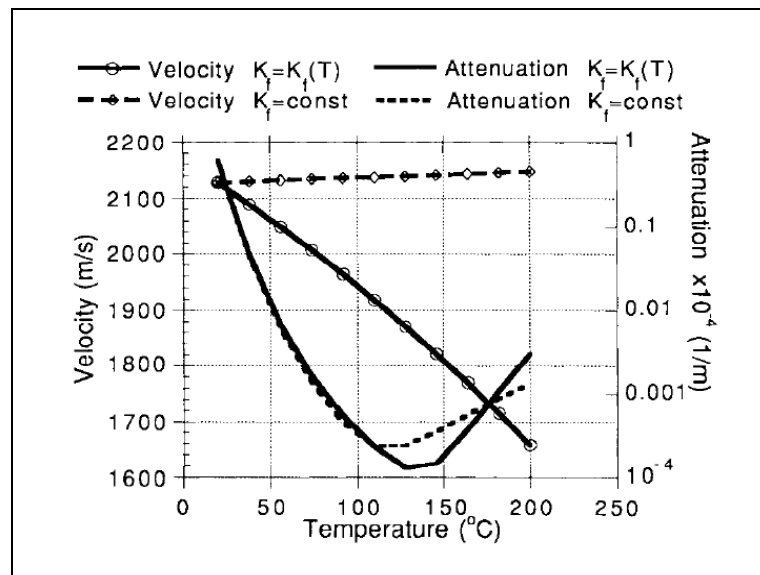


Figure 3-5: The effect of constant and variable fluid bulk modulus on attenuation (from Eastwood, 1983).

From the above explanations, it can be concluded that the quality factor trend obtained from laboratory measurement, shown in Figure 3-4, matches the theoretical trend given in Figure 3-3.

3.6 Quality factor and permeability

The BISQ equations show that the seismic response is not only sensitive to the parameters in Gassmann's relations (equations 2.28 and 2.29) and viscosity, but also it is sensitive to the permeability of the rock. For this reason, poroviscoelastic theories can be used to predict permeability from seismic attributes as well. For the reservoir properties given in Table 3-3, the change in Q with permeability as predicted by BISQ theory is shown in Figure 3-6.

Similar to the previous curves shown in Figures 3-2 and 3-3, the quality factor decreases to a minimum before it starts to increase with permeability.

Parameter	Value	Unit
Fluid density	1,000	kg/m^3
Fluid bulk modulus	0.8	GPa
Fluid saturation	1	
Porosity	0.25	
viscosity	500,000	cp
Characteristic length	1	mm
Matrix bulk modulus	35	GPa
Matrix density	2,650	kg/m^3
Dry frame bulk modulus	1.7	GPa
Dry frame shear modulus	1.35	GPa
Frequency	300	Hz

Table 3-3: Reservoir parameters used for generating the graph of quality factor versus permeability shown in Figure 3-6.

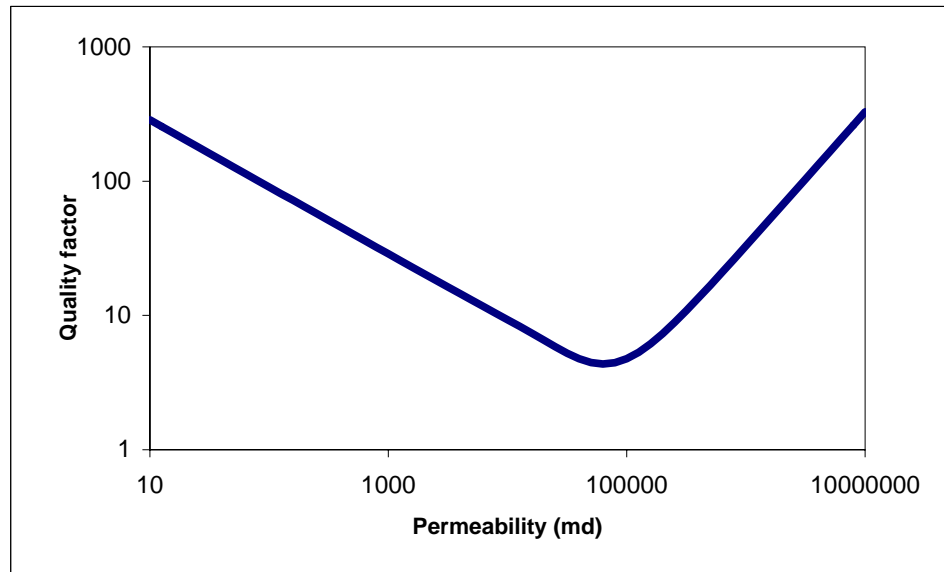


Figure 3-6: Variation of quality factor with permeability predicted by BISQ theory, computed from the reservoir parameters given in Table 3-3.

The graph implies that at both ends of the permeability range, the seismic response of the material is elastic while at an intermediate permeability, the attenuation reaches its maximum which means that the seismic behavior of the material is viscoelastic.

3.7 Quality factor and mobility

In fact, the parameter that drives the viscoelastic behavior of the material is mobility rather than permeability or viscosity alone. Mobility of any fluid is defined as the ratio of rock permeability to fluid viscosity:

$$M = \frac{k}{\eta_f}. \quad (3.10)$$

Viscosity and permeability appear together as the inverse of mobility in the BISQ relations (equation 3.8), and therefore, their combined effect will influence the seismic response. This can be inferred from Figures 3-3 and 3-6 as well, because a constant permeability and a constant viscosity are used to generate the graphs, respectively.

Parameter	Value	Unit
Fluid density	1,000	<i>kg/m³</i>
Fluid bulk modulus	0.8	<i>GPa</i>
Fluid saturation	1	
Porosity	0.25	
Characteristic length	1	<i>mm</i>
Matrix bulk modulus	35	<i>GPa</i>
Matrix density	2,650	<i>kg/m³</i>
Dry frame bulk modulus	1.7	<i>GPa</i>
Dry frame shear modulus	1.35	<i>GPa</i>
Frequency	300	<i>Hz</i>

Table 3-4: Reservoir parameters used for generating the graph of quality factor versus mobility shown in Figure 3-7.

That means, the horizontal axis in Figure 3-3 is inversely proportional to the mobility while it is directly proportional to mobility in Figure 3-6. For the reservoir properties given in Table 3-4, the change in Q with mobility is shown in Figure 3-7.

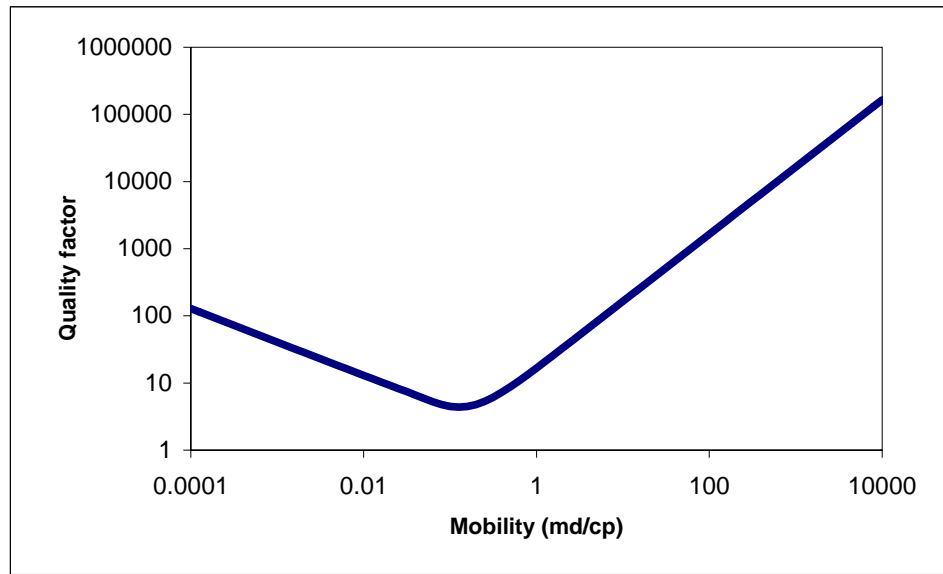


Figure 3-7: Variation of quality factor with mobility predicted by BISQ theory, computed from the reservoir parameters given in Table 3-4.

Chapter Four: Effects of attenuation on seismic response

Quality factor, which is inversely proportional to the attenuation, is defined as the ratio of energy over the loss of energy per cycle (Aki and Richards, 2002).

$$Q = \frac{2\pi E}{\Delta E}, \quad (4.1)$$

where E is the total energy stored in the wave and ΔE is the energy lost in one cycle.

The amplitude of the wave is directly related to its energy, which means that, in a viscoelastic medium, the seismic wave amplitude decreases after each cycle. On the other hand, this decrease in the amplitude is frequency dependant because higher frequency signals have smaller wavelengths and therefore, when traveling between two fixed points, go through more cycles; hence lose more energy. Attenuation of higher frequency components changes the shape of the amplitude spectrum of the recorded signal at the receiver location as compared to its shape at the source location.

The differences in the source and receiver amplitude spectra can be linked to the properties of the medium between the source and receiver. In the current study, the focus is to relate such changes to the quality factor, Q .

4.1 Quality factor, amplitude and frequency

The plane wave solution of the wave equation is given by

$$U = U_0 \exp[i(2\pi ft - \bar{\kappa}x)], \quad (4.2)$$

where $\bar{\kappa}$ is the wave number. Attenuation can be added to the solution by introducing a complex wave number (Lines et al., 2008):

$$\kappa = \bar{\kappa} - i\alpha, \quad (4.3)$$

where α is the attenuation factor and is defined as:

$$\alpha = \frac{\pi f}{Qv}. \quad (4.4)$$

Replacing $\bar{\kappa}$ with κ in equation (4.2) and substituting equations (4.3) and (4.4) into equation (4.2) will result in the plane wave solution of the wave equation in a dissipative media:

$$U = U_0 \exp\left(-\frac{\pi f}{Q}t\right) \exp[i(2\pi ft - \bar{\kappa}x)] = U_0 \exp\left(-\frac{\pi}{Q}\frac{x}{\lambda}\right) \exp[i(2\pi ft - \bar{\kappa}x)], \quad (4.5)$$

which means that the amplitude U of the wave decreases with time or distance as

$$U = U_0 \exp\left(-\frac{\pi f}{Q}t\right) = U_0 \exp\left(-\frac{\pi}{Q}\frac{x}{\lambda}\right). \quad (4.6)$$

The effect of attenuation is shown in Figure 4-1 for a Ricker wavelet with the central frequency of 50 Hz and the sampling interval of 0.002 sec. The figure shows the amplitude spectrum of the wavelet at the source location (solid blue curve), and the amplitude spectrum of the recorded signal (dashed red curve) which has travelled for 0.1 seconds in a medium with the quality factor of $Q = 20$.

From Figure 4-1, it is clear that not only the amplitude of the signal changes, but also the distribution of the frequency content shifts toward lower frequencies, in other words; the attenuating medium acts as a low pass filter. Figure 4-2 shows the results of the same analysis on a Ricker wavelet with the central frequency of 100 Hz.

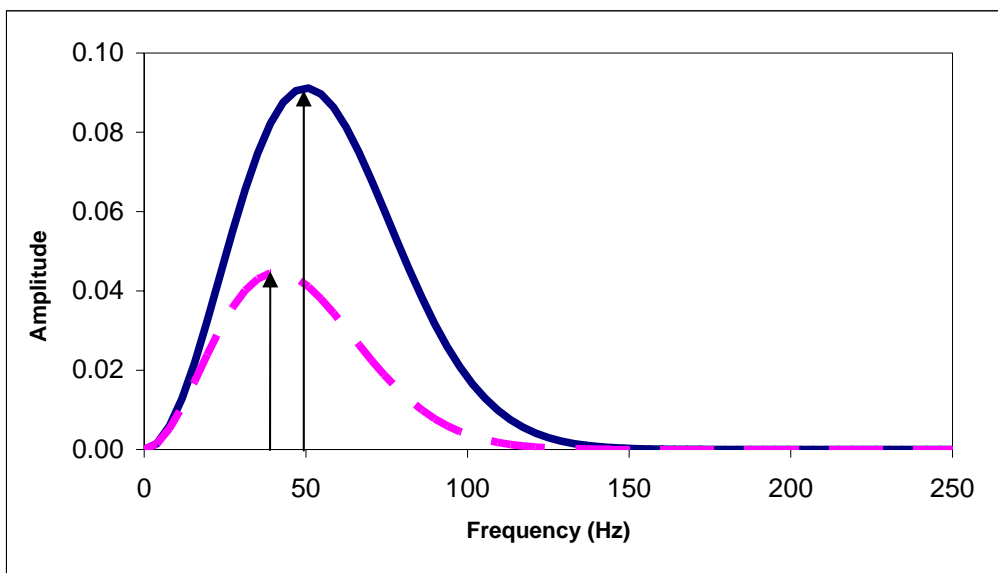


Figure 4-1: The amplitude spectra of the Ricker wavelet at the source location (solid blue) and the receiver location (dashed red), modeled with central frequency of 50 Hz.

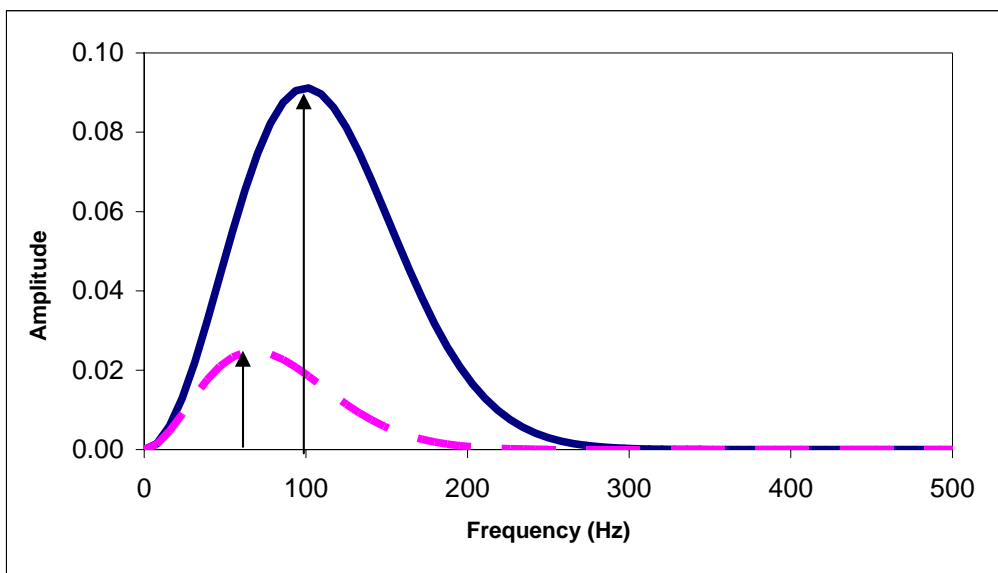


Figure 4-2: The amplitude spectra of the Ricker wavelet at the source location (solid blue) and the receiver location (dashed red) modeled with central frequency of 100 Hz.

The amplitude spectra of Figure 4-2 demonstrate more attenuation compared to the case shown in Figure 4-1. Also, the shift in the central frequency is greater in this case. The arrows in these figures mark the maximum amplitude U_{\max} and the frequency of the maximum amplitude f_{\max} . Table 4-1 summarizes the observed changes.

The maximum amplitude in Case 1 (low frequency scenario) at the receiver location drops to 49% of its value at the source location (51% decrease) while in Case 2 (high frequency scenario) it drops to 27% of the original value (73% decrease). Also, the frequency of maximum amplitude decreases by 6 Hz from source to receiver in the low frequency case while this shift is 29 Hz in the high frequency case. Such variations in the amplitude and frequency content of the data can be used for estimation of quality factor from seismic data.

Central frequency (Hz)		At source		At receiver	
		U_{\max}	f_{\max} (Hz)	U_{\max}	f_{\max} (Hz)
Case 1	50	0.0912	50	0.0446	44
Case 2	100	0.0912	100	0.0248	71

Table 4-1: The maximum amplitude and the frequency of maximum amplitude for the Ricker wavelets modeled at different central frequencies (at the source and receiver locations).

The analysis described above implies that high frequency seismic data are preferred for the Q estimation studies, because the observed changes in the seismic attributes in high frequency scenarios are more significant, and therefore similar noise levels introduce less relative error in such data.

4.2 Quality factor and reflection coefficient

Contrast in acoustical impedance causes reflections at the boundaries. The reflection coefficient at a boundary for a normally incident wave is given by the following familiar equation:

$$R_{AI} = \frac{\rho_2 v_2 - \rho_1 v_1}{\rho_2 v_2 + \rho_1 v_1}. \quad (4.7)$$

Contrasts in the quality factor can also cause reflections. The reflection coefficient for a boundary separating two media with contrasts in both the acoustical impedance and attenuation is given by the following equation (Lines et al., 2008):

$$R_{AI-Q} = \frac{\rho_2 v_2 \left(1 + \frac{i}{2Q_2}\right) - \rho_1 v_1 \left(1 + \frac{i}{2Q_1}\right)}{\rho_2 v_2 \left(1 + \frac{i}{2Q_2}\right) + \rho_1 v_1 \left(1 + \frac{i}{2Q_1}\right)}. \quad (4.8)$$

If there is no contrast in Q , this equation will simplify into equation (4.7), and if there is no contrast in the acoustical impedance, the reflection coefficient equation will reduce to

$$R_Q = \frac{i \left(\frac{1}{Q_2} - \frac{1}{Q_1} \right)}{2 \left[2 + \frac{i}{2} \left(\frac{1}{Q_2} + \frac{1}{Q_1} \right) \right]}. \quad (4.9)$$

The complex nature of the reflection coefficient at the presence of quality factor contrast implies that not only the amplitude of the reflected waves change, but also the phase will change. Another characteristic of the reflection coefficient in these equations

is that due to frequency dependence of quality factor (Futterman, 1962), the reflection coefficient also shows frequency dependence.

Lines et al. (2008) showed that for the model properties given in Table 4-2, the reflection caused by the contrast only in the quality factor is not as significant as the reflection from a boundary with acoustical impedance contrast.

	Quality factor	Velocity (m/s)
Layer 1	40	2000
Layer 2	6.283	3500

Table 4-2: Model properties (from Lines et al., 2008).

Three reflection coefficients, calculated from equations (4.7) to (4.9), for the boundary of the model given in Table 4-2 are as follows:

$$R_{AI} = 0.2727$$

$$R_{AI-Q} = 0.2744 + 0.0310i .$$

$$R_Q = 0.0015 + 0.0335i$$

The amplitude and phase of these reflection coefficients are given in Table 4-3.

The amplitude of R_Q is around 1/8 of the amplitudes of the other reflection coefficients, therefore, it is not considered significant, specially in realistic geological situations where noise is present. On the other hand, the phase rotation related to the cases where both the acoustical impedance contrast and attenuation contrast are present is negligible.

These calculations have been verified using finite difference forward modeling of the SH waves. SH waves have the unique property of no mode change at the boundaries which makes them computationally simpler for simulation as opposed to the case of P-

SV waves in which mode conversion occurs between the P-wave and SV-wave components at each boundary. Shearer (1999) stated that the boundary conditions and reflection coefficients for the SH wave propagation are the same as those of P-waves.

	Amplitude	Phase (degrees)
R_{AI}	0.2727	0
R_{AI-Q}	0.2762	6.44
R_Q	0.0335	87.4

Table 4-3: Calculated amplitude and phase of the reflection coefficients.

Figure 4-3 shows two models created with the parameters given in Table 4-2. Model 1 shows a two layer model with a velocity boundary, while Model 2 shows the same two layer geological model with attenuation boundary.

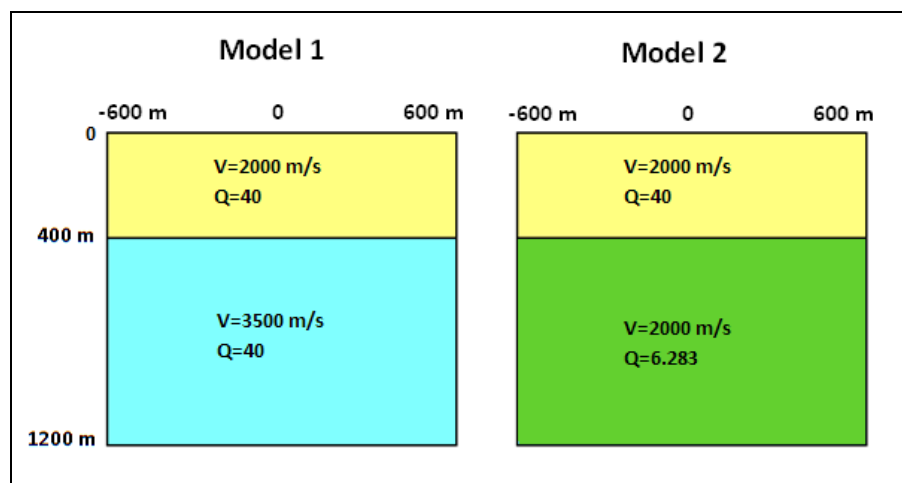


Figure 4-3: Two layer geological models showing model (1): contrast in impedance and model (2): contrast in attenuation (from Lines et al., 2008).

Each model is discretized into 10 m by 10 m cells, the source point is located at the depth of 250 m at $x = 0$, and the receivers are lined up across layer 1 at the depth of 260 m with the spacing of 10 m.

The results of the SH finite difference forward modeling for these input models are shown in Figure 4-4. These seismic sections illustrate two types of arrivals each. Direct arrivals from source to receivers, and reflected arrivals. The vertical axis shows the two way travel time.

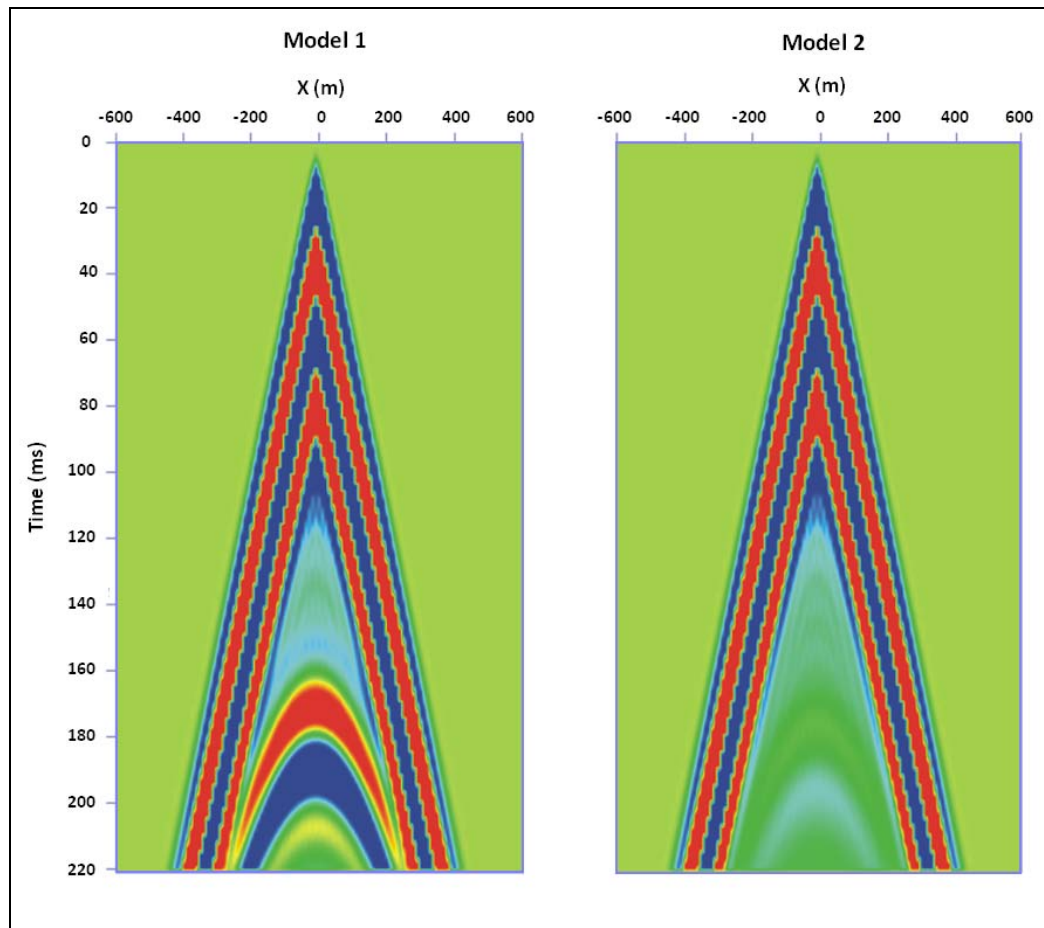


Figure 4-4: The finite difference seismic responses of the models shown in Figure 3-3 (from Lines et al., 2008).

At around 155 ms, Model 1 shows a reflection hyperbola that is caused by the acoustical impedance boundary which is stronger than the same reflection event in Model 2, which is due to the attenuation boundary. The results of the finite difference forward modeling confirms that the reflections from an attenuation boundary are negligible compared to reflections from an acoustical impedance boundary.

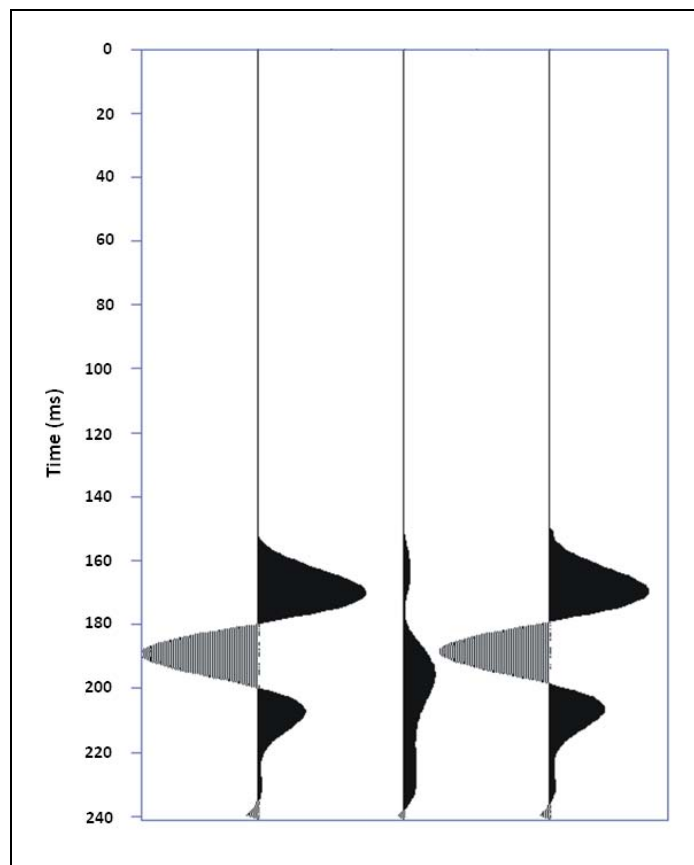


Figure 4-5: Normally incident reflections from three different boundaries. Left: impedance boundary, middle: attenuation boundary, right: impedance and attenuation boundary (from Lines et al., 2008).

The zero offset traces for the three cases of Table 4-3 are shown in Figure 4-5.

The traces show the normal incident reflections from a boundary with acoustical

impedance contrast only (left), attenuation contrast only (middle) and both contrasts (right). The lower reflection amplitude and the phase rotation, calculated in Table 4-3 for the case of attenuation boundary, are observed in the middle trace. These traces also show that there is a small time delay of about 5 ms in the arrival of the middle trace.

The similarity of the amplitude and phase of the reflected arrivals between the leftmost and rightmost traces confirms the calculations shown in the first two rows of Table 4-3. In the case of a boundary with contrast in acoustical impedance and quality factor, the additional change in the reflection coefficient caused by contrast in Q is not significant and if the noise is added to the scenario, which is the case in real seismic data, it is very difficult to measure; therefore, the reflection coefficient approach will not be used for estimating Q in this project.

4.3 Estimation of Q

Quality factor, as shown in Figures 4-1 and 4-2, contributes to two forms of change in the final amplitude spectrum of the recorded signal; change in the amplitudes, and change in the frequency. These changes can be related to the quality factor through equation (4.6). Therefore, two methods for Q estimation can be developed.

4.3.1 Spectral ratio

In this method, the ratio of the amplitudes in the frequency domain will be used in the attempt to estimate Q . For the amplitudes recorded at two locations, it can be shown that (Spencer et al., 1982; Hardage, 1983):

$$\ln\left(\frac{U_2(f)}{U_1(f)}\right) = \frac{-\pi}{Q\bar{\lambda}}(x_2 - x_1) = \frac{-\pi f}{Q}(t_2 - t_1), \quad (4.10)$$

where $\bar{\lambda}$ is the wavelength. Rearranging equation (4.10), Q is calculated from the spectral ratio using

$$Q = \frac{-\pi(x_2 - x_1)}{\bar{\lambda} \ln\left(\frac{U_2(f)}{U_1(f)}\right)} = \frac{-\pi f(t_2 - t_1)}{\ln\left(\frac{U_2(f)}{U_1(f)}\right)}. \quad (4.11)$$

4.3.2 Centroid frequency shift

Centroid frequency indicates the center of mass of the amplitude spectrum. It is defined as

$$f_c = \frac{\int_0^{\infty} fU(f)df}{\int_0^{\infty} U(f)df}. \quad (4.12)$$

The centroid frequency changes as the wave propagates in the medium because the entire amplitude spectrum shifts toward the lower frequencies. Figures 4-1 and 4-2 illustrate this shift in the frequency of the signal. Quan and Harris (1997) showed that quality factor can be calculated from the shift in the centroid frequency of the signal using

$$Q = \frac{\pi(x_2 - x_1)}{(f_{c2} - f_{c1})v} \frac{\int_0^{\infty} (f - f_{c1})^2 U(f)df}{\int_0^{\infty} U(f)df}, \quad (4.13)$$

where f_{c1} and f_{c2} are the centroid frequencies of the signal at locations x_1 and x_2 respectively, calculated using equation (4.12).

The frequency shift method is relatively insensitive to geometric spreading and reflection and transmission effects. This method is applicable to many seismic scenarios where the frequency range is broad enough to cause noticeable losses in the higher frequency contents (Quan and Harris, 1997). Therefore, this technique is assumed to be superior to the spectral ratio method. A recent modeling study shows that the inversion results from the spectral ratio method is in error by a factor of two, while the results from the centroid frequency method is accurate to within 10% (Vasheghani and Lines, 2009).

As mentioned earlier, higher frequency data are more suitable for estimating Q . Crosswell seismic data usually have higher frequency content than surface seismic. Given the existing limits on the frequency content of seismic data, including VSP surveys, the combination of the crosswell data and the centroid frequency method for Q estimation provides the most reliable and accurate tool for viscosity characterization in heavy oil reservoirs.

In a common crosswell survey, sources are located in one well while receivers are in an adjacent well (Figure 4-6). Direct, reflected and refracted signals are recorded at the receiver and are processed for different attributes. Two important measurements are travel time and frequency content of the recorded signal.

Crosswell seismic surveys are performed from within the reservoir or zone of interest instead of surface and therefore provide several practical advantages. The data exhibit higher resolution than the surface seismic data (typically 10-100 times better). Crosswell data is collected directly with reference to depth; therefore the uncertainties associated with time to depth conversion are avoided. The near surface is also bypassed and the problem of near surface effects is eliminated.

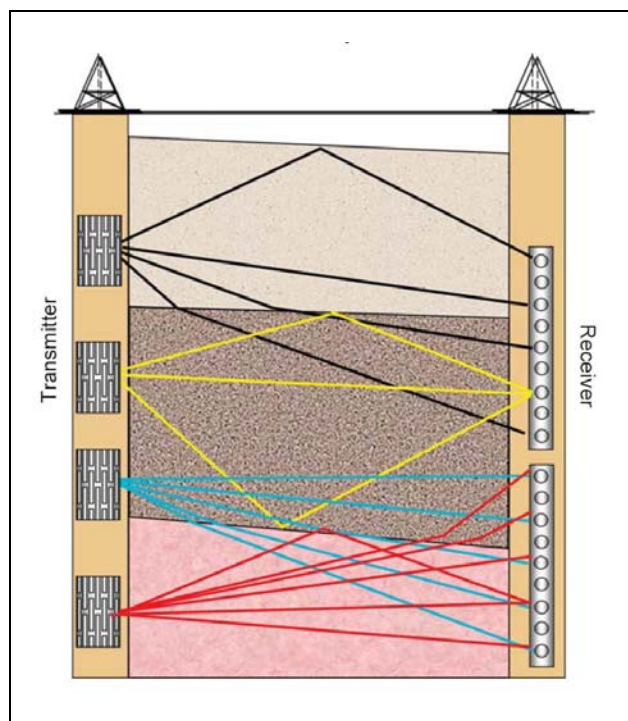


Figure 4-6: Crosswell survey configuration. Direct, reflected and refracted rays traveling from source to receiver.

There are some disadvantages associated with the crosswell data as well.

Although they provide repeatability, this is conditional upon shutting the production or injections wells for the duration of the survey, as the tools might not function properly in the flowing wells. Also the coverage area of a crosswell survey mostly involves the 2D plane between the source and receiver wells. A trade off exists between the resolution and areal coverage of the surveys. Within the constraints of the current technology, higher resolution data such as well logs or crosswell data cover smaller areas than what is covered by lower resolution data such as surface seismic.

Chapter Five: Estimating viscosity from crosswell seismic data

Crosswell seismic data are good candidates for viscosity estimation because they contain higher frequencies which allow greater changes in the recorded signal. Another advantage of the crosswell data is that the rays do not go through the near surface layer which is a highly attenuating zone and absorbs most of the energy; therefore, in crosswell surveys the high frequency content of the data reaches further into the zone of interest.

5.1 Methodology

The first step in the quest for viscosity is to estimate Q from crosswell data. Once Q values are available, the viscosity of the fluid can be calculated using the BISQ relations (equations 3.6 and 3.8). The workflow is shown in Figure 5-1.

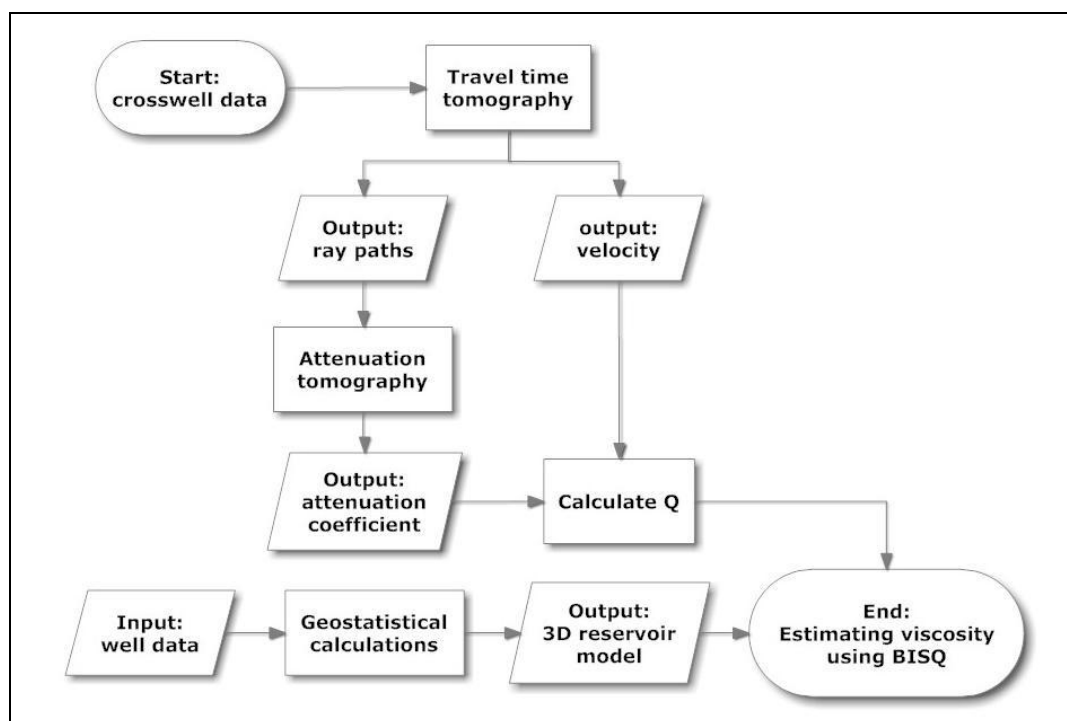


Figure 5-1: The workflow for estimating viscosity from crosswell seismic data.

5.2 Tomography

Tomography is an imaging technique that uses the information carried by penetrating waves, and has applications in many areas such as radiology, geophysics and materials science. Seismic tomography is a method for estimating the earth's properties such as P-wave velocity (using travel time tomography) or attenuation (using attenuation tomography). Such techniques are formulated as an inverse problem in which the properties of the model will be estimated from the measured response of the model.

One application of seismic tomography is in the crosswell seismic data analysis where rays travel from sources in one well to receivers in a nearby well. The three steps involved in the crosswell tomography as explained by Lines (1991) are:

- 1- Identifying the response (travel times or frequency shifts) from the seismic data
- 2- Ray tracing (assuming a set of properties for the model) to formulate the problem
- 3- Solving the equations to estimate or update model properties.

Although travel time tomography and attenuation tomography use the same principles, two different approaches are used in this research in order to formulate the problem (i.e. in the Step 2 of the above).

5.2.1 Travel time tomography

In conventional crosswell travel time tomography, the area between and around wells is divided into a 3D network of grid cells. The objective is to find the velocity for each cell. The advantage of using a 3D approach instead of a 2D plane between the source and receiver wells is that it takes into account the out of plane reflections and refractions. It is also useful in the case of deviated source or receiver wells. An initial velocity model (or slowness model) is assumed and rays are traced from sources to

receivers utilizing Snell's law. In a simple scenario, it is assumed that rays are refracted or reflected at the sides of each cell but because the velocity is constant throughout each cell, rays do not bend inside individual cells. In a simpler case, it is assumed that straight rays connect the sources to receivers. This is illustrated in Figure 5-2. The total travel time for every ray is the sum of all the travel times of that ray in each cell. This can be written as

$$T_i = \sum_j l_{ij} s_j, \quad (5.1)$$

where T_i is the total travel time of ray i , l_{ij} is the length that ray i travels in cell j , and s_j is the slowness in cell j . In matrix form, equation (5.1) takes the following form:

$$\begin{matrix} \mathbf{T} \\ \left[\begin{array}{c} T_1 \\ T_2 \\ \vdots \\ T_M \end{array} \right] \end{matrix} = \begin{matrix} \mathbf{L} \\ \left[\begin{array}{cccc} l_{11} & l_{12} & \cdots & l_{1N} \\ l_{21} & l_{22} & \cdots & l_{2N} \\ \vdots & \vdots & \ddots & \vdots \\ l_{M1} & l_{M2} & \cdots & l_{MN} \end{array} \right] \end{matrix} \begin{matrix} \mathbf{S} \\ \left[\begin{array}{c} s_1 \\ s_2 \\ \vdots \\ s_N \end{array} \right] \end{matrix}. \quad (5.2)$$

M and N in equation (5.2) represent total number of rays and total number of grid cells, respectively. The goal is to find the slowness vector \mathbf{s} and the matrix of ray lengths, \mathbf{L} . Updated slowness vector implies that another ray tracing should be performed as rays travel differently in a new velocity field. Equation (5.2) should be established and solved again which results in a newer version of the slowness vector. This process will be repeated iteratively until the difference between calculated and measured travel times is within an acceptable threshold. This method will be referred to as pixelated inversion.

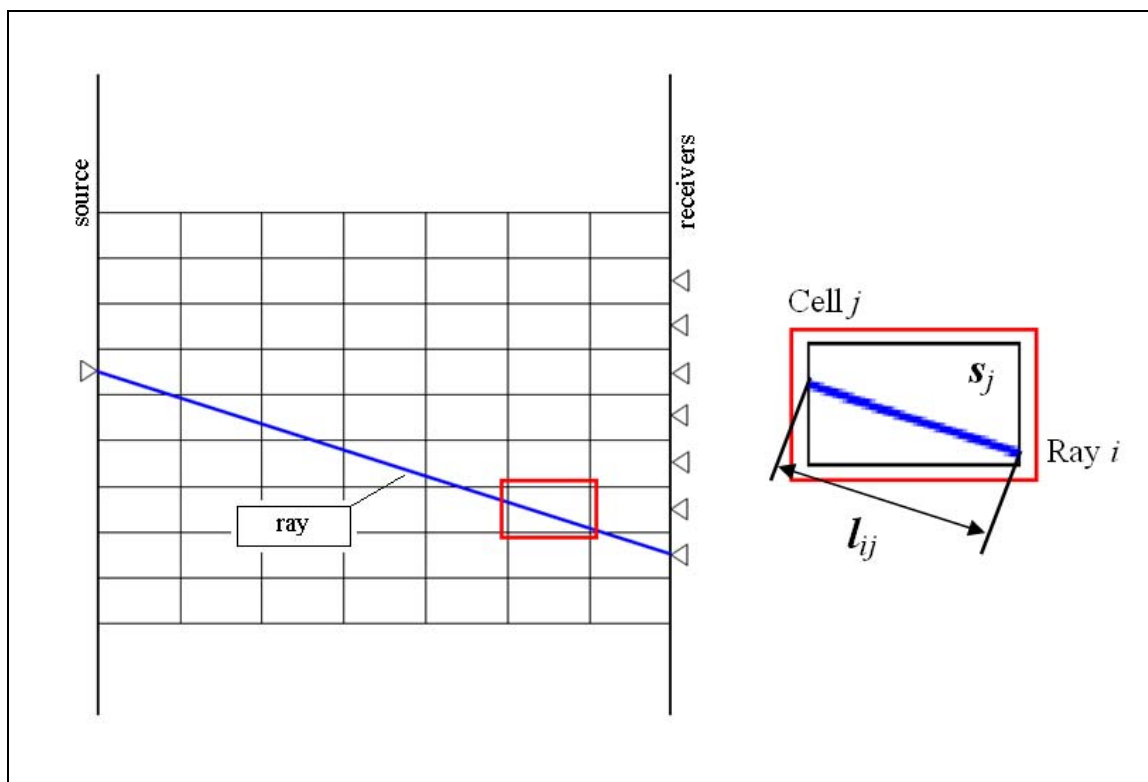


Figure 5-2: Total travel time for a ray is the sum of travel times in each cell.

Another technique uses the Chebyshev polynomials as described by Washbourne et al. (2002). Although the objective in this method is also to find the velocity model between the wells, it uses a different approach in formulating the equations. In this method, the area around and between the wells are divided into layers (Figure 5-3). The layer boundaries will follow the geological structure which is constructed from the well logs. These interfaces remain unchanged during the inversion process and therefore, careful design of each layer is crucial for the accuracy of final results.

Unlike the pixelated model, where the slowness in each cell is assumed to be constant throughout the cell during an iteration, in this method the slowness in each layer varies laterally and is modeled by third order 2D Chebyshev polynomials given as:

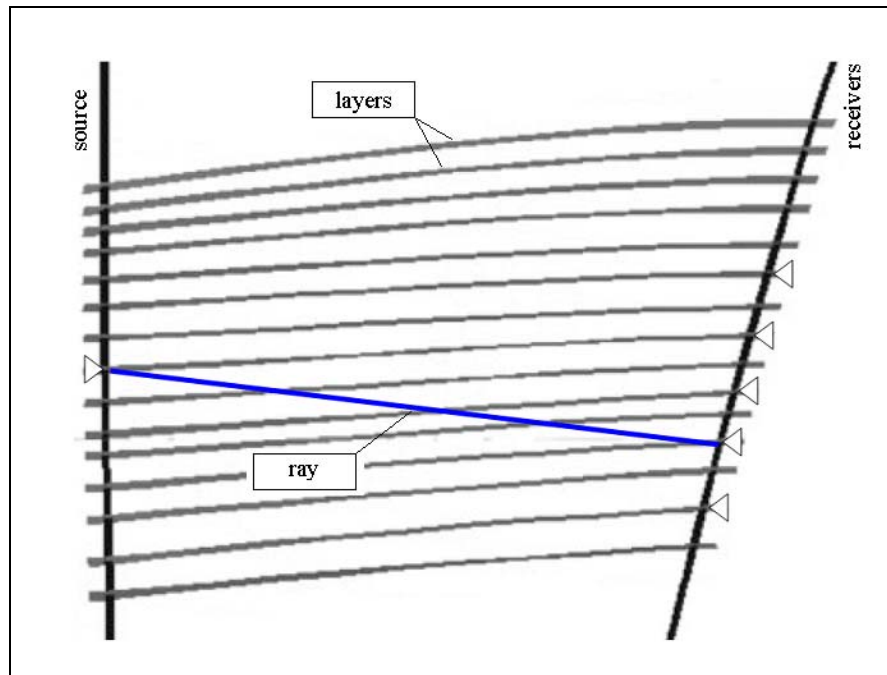


Figure 5-3: The area between the wells is divided into layers. Chebyshev polynomials describe the velocity in each layer (Modified from Washbourne et al., 2002)

$$\begin{aligned}
 s_j(x, y) = & c_0 + c_1x + c_2y + c_3xy + c_4(2x^2 - 1) \\
 & + c_5(2y^2 - 1) + c_6(2x^2 - 1)y \\
 & + c_7(2y^2 - 1)x + c_8(4x^3 - 3x) \\
 & + c_9(4y^3 - 3y)
 \end{aligned} \tag{5.3}$$

The x and y in this equation represent the lateral coordinates of a point in a two dimensional layer. Equation (5.3) will be set up for each layer and therefore, there is no need to introduce the z coordinate. Instead the subscript j is used to denote the layer number for all layers, stacked in the z direction. These polynomials will capture the lateral variations in the slowness of each layer. The travel time of each ray in a layer is calculated using

$$t_{ij} = \int s_j(x, y) dl_i . \quad (5.4)$$

The total travel time of ray i , from source to receiver, is then calculated by adding the travel times from every layer j :

$$T_i = \sum_j t_{ij} . \quad (5.5)$$

The goal of the inversion process is to find the Chebyshev polynomial coefficients $c_0 - c_9$ for each layer. This method has several advantages over the pixelated inversion technique (Washbourne et al., 2002). For each layer, the system has to be solved for only 10 coefficients which is fewer parameters than the pixelated model and results in a more well conditioned inverse. This method also provides high vertical resolution, comparable to the vertical resolution of the wireline logs.

5.2.2 Attenuation tomography

In the current workflow (Figure 5-1), the travel time tomography is performed using the Chebyshev polynomials. Once the velocity tomogram and the ray paths are known, the model is discretized into grid cells and the velocity and ray length for each cell are assigned from the known results of travel time tomography. The attenuation tomography is then performed using the pixelated method. As the rays travel in each cell, their frequency content changes continuously until they reach the receiver. This occurs because of the presence of attenuation. The change in the frequency content of the signal is reflected in the change in its centroid frequency. Variation of the centroid frequency for a signal travelling from source to receiver is related to the attenuation coefficient of all cells using the following equation:

$$\sum_j \alpha_{0j} l_{ij} = \frac{f_s - f_{Ri}}{\sigma_s^2}, \quad (5.6)$$

where α_0 is attenuation coefficient, f_s and f_R are the centroid frequencies at the source and receiver locations, respectively, calculated using equation (4.12), subscripts i and j denote the ray and cell numbers, respectively. σ_s^2 is the variance of the amplitude spectrum of the source signal and is calculated using the following equation (Quan and Harris, 1997):

$$\sigma_s^2 = \frac{\int_0^\infty (f - f_s)^2 A(f) df}{\int_0^\infty A(f) df}. \quad (5.7)$$

In matrix form, equation (5.6) can be written as

$$\begin{bmatrix} \Delta f_1 \\ \Delta f_2 \\ \vdots \\ \Delta f_M \end{bmatrix} = \begin{bmatrix} l_{11} & l_{12} & \cdots & l_{1N} \\ l_{21} & l_{22} & \cdots & l_{2N} \\ \vdots & \vdots & \ddots & \vdots \\ l_{M1} & l_{M2} & \cdots & l_{MN} \end{bmatrix} \begin{bmatrix} \alpha_{01} \\ \alpha_{02} \\ \vdots \\ \alpha_{0N} \end{bmatrix} \quad (5.8)$$

Unlike equation (5.2), the ray length matrix L is known in this case and equation (5.8) is

solved in only one iteration in order to calculate the attenuation coefficient matrix.

Knowing the velocity for each grid cell from the travel time tomography, the attenuation

coefficient is converted to the quality factor Q using the following equation

$$Q = \frac{\pi}{\alpha_0 v}, \quad (5.9)$$

where v is the velocity. One should note that α_0 is related to the attenuation factor α (equation 4.4) through the following relation:

$$\alpha_0 = \frac{\alpha}{f}. \quad (5.10)$$

The result of the above inversion is a Q tomogram. Once the Q tomogram is generated, it can be related to viscosity using BISQ theory (equations 3.6 and 3.8). It is required that the reservoir parameters in equation (3.8) to be known for each grid cell in the tomogram so that a direct relationship between quality factor and viscosity can be established. This direct relationship allows the estimation of the viscosity tomogram from the Q tomogram.

5.3 Estimating reservoir properties

Bore hole data such as logs, fluid samples or core samples are the only sources of information for the reservoir parameters. However, these data are only available at the well locations. Compared to the areal and vertical extent of the heavy oil reservoirs, these data points cover only a small fraction of the entire reservoir. In order to populate reservoir and fluid properties around and in between the wells, geostatistical techniques can be used. Geostatistics is a branch of statistics that focuses on the spatial complexity of the subsurface geology. Geostatistical methods are flexible and relatively easy to use (Jensen et al., 2000). Several methods exist for property estimation, namely kriging and sequential Gaussian simulation.

5.3.1 Kriging

In kriging, the value of any grid cell is estimated using the known values from the neighbouring cells through the following equation:

$$\hat{\gamma} = \sum_i w_i \gamma_i, \quad (5.11)$$

where γ_i denotes the known values at the adjacent locations and coefficients w_i are weighting factors. In a simple case scenario, the weight factor is a function of distance as shown in Figure 5-4.

The weight factors w_i are assigned using the variogram. A variogram is a tool for describing the spatial variation of a parameter. It is based on the principle that closely spaced samples are likely to show more correlation than those located far from each other. Anisotropy can also be introduced into the geostatistical modeling through the variogram.

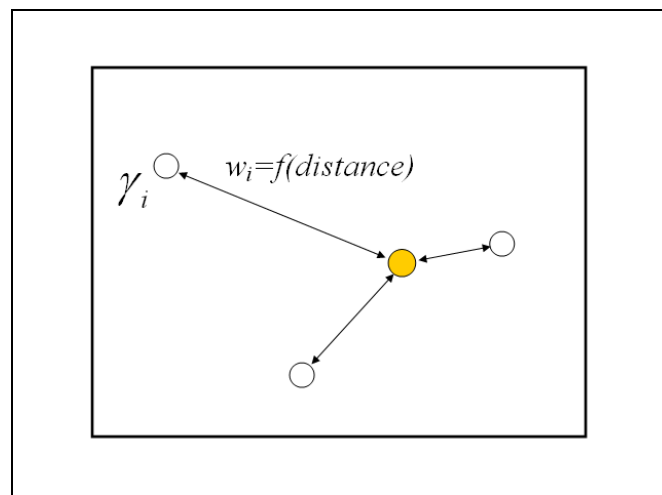


Figure 5-4: In kriging, neighboring cells are used to estimate an unknown value. The weight of each adjacent cell on the final estimate is proportional to its distance from the unknown cell.

Once the variogram is established and the weight factors are determined, a mean and a standard deviation can be calculated for any given grid cell. Kriging tends to produce smooth images of reality. In doing so, short scale variability is poorly reproduced, while it underestimates extremes.

5.3.2 Sequential Gaussian simulation

Unlike kriging, which is smooth and locally accurate, the simulation techniques allow the assessment of uncertainty through the possibility of alternative realizations. Realizations are different because the grid cells to be evaluated are selected in a random order in each realization. The mean and standard deviation for that cell is determined using the kriging method. Knowing the mean and standard deviation for the given cell, the Gaussian curve can be established. A value is drawn randomly from the Gaussian distribution and is assigned to the cell. This algorithm continues until all the cells are evaluated. Since there are two steps that involve random selection, alternative realizations generate different results.

In the current workflow, shown in Figure 5-1, sequential Gaussian simulation is used for the estimation of input reservoir parameters.

5.4 BISQ inversion

Once the reservoir parameters are known, the $Q - \eta_f$ relationship can be established and used for converting Q tomogram to η_f tomogram. Because each grid cell contains a unique set of reservoir and fluid parameters, the function $Q = f(\eta_f)$ is not

universal throughout the zone of interest and should be set up independently for each individual cell.

Another consideration is that the $Q - \eta_f$ relation is not invertible. A function is invertible if and only if it is a one to one function. The graph of Q versus η_f shown in Figure 3-3 clearly demonstrates that the $Q - \eta_f$ relationship is not a one to one function. That is for every given Q there is generally more than one value of η_f ; therefore, the function $\eta_f = f^{-1}(Q)$ is mathematically nonexistent, hence there is no direct way to calculate the viscosity from Q . In order to resolve this issue and convert the Q tomogram to η_f tomogram, the $Q - \eta_f$ relationship can be divided into two one to one and invertible domains (the decreasing side and the increasing side of the curve) so that an inverse function can be calculated for each side. An alternative approach is to set up a lookup table of $Q - \eta_f$ values and look up viscosity values for a given quality factor. Since it is not realistic to create a large table with very small Q increments for each cell, it is possible that the Q value which is going to be looked up falls between two table entries, in such case viscosity values can be calculated by interpolation.

It is important to note that with any of the above mentioned alternative approaches, two viscosity values few orders of magnitude apart can be determined for any given quality factor. At this point the correct one can only be selected based on previous knowledge of fluid properties in the region of study.

Chapter Six: Case study

The workflow for estimating viscosity of oil from crosswell data as described in Figure 5-1 will be applied on a dataset from a heavy oil reservoir in Alberta, Canada. The reservoir is located in the Athabasca region in the north eastern part of the province of Alberta (Figure 6-1). Athabasca oil sands are large deposits of bitumen which are estimated to be 1.7 to 2.5 trillion barrels, out of which 170 billion barrels are economically recoverable.



Figure 6-1: Athabasca oil sands located in the north eastern part of the province of Alberta in Canada.

6.1 Geology of the area

The Athabasca oil sands together with Cold Lake and Peace River oil sands, located south and west of the Athabasca region, respectively, are the three major bitumen deposits in the Western Canadian Sedimentary Basin (Figure 6-1). Most of the hydrocarbon traps in the WCSB are stratigraphic in nature as shown in Figure 6-2.

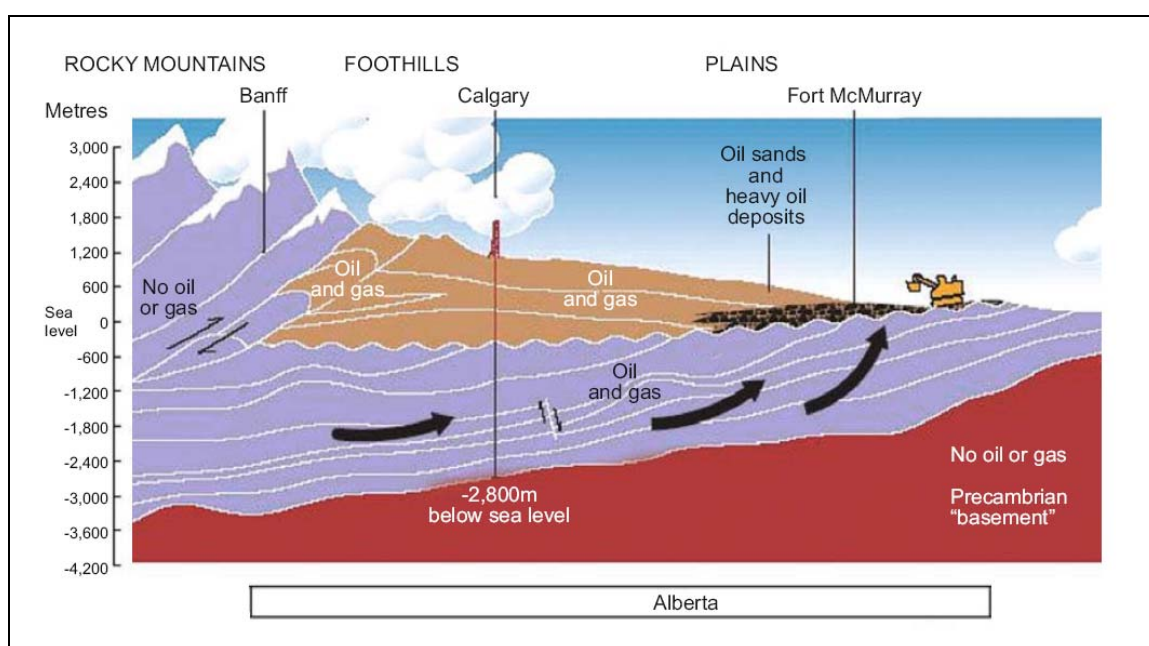


Figure 6-2: The schematic cross section of the Western Canadian Sedimentary Basin across the Athabasca region (Modified from Zhou et al., 2008). Arrows show the migration paths of the heavy oils from source rock to the reservoirs.

The bitumen reserves contain oils with gravities ranging from 8 to 12° API, and viscosities ranging up to several million centipoise, which are hosted in the reservoirs of varying age, ranging from Devonian to early Cretaceous. The regional stratigraphy of the Athabasca oil sands area is shown in Figure 6-3. The heavy oil reservoir of this study is located in the Grand Rapids formation in the western Athabasca area and is within a

sequence of Quaternary, Cretaceous and Devonian sediments on the Precambrian crystalline basement. Cretaceous units include the shales and sands of the Labiche, Viking and Joli Fou formations of the Colorado Group and Grand Rapids, Clearwater and McMurray formations of the Mannville Group.

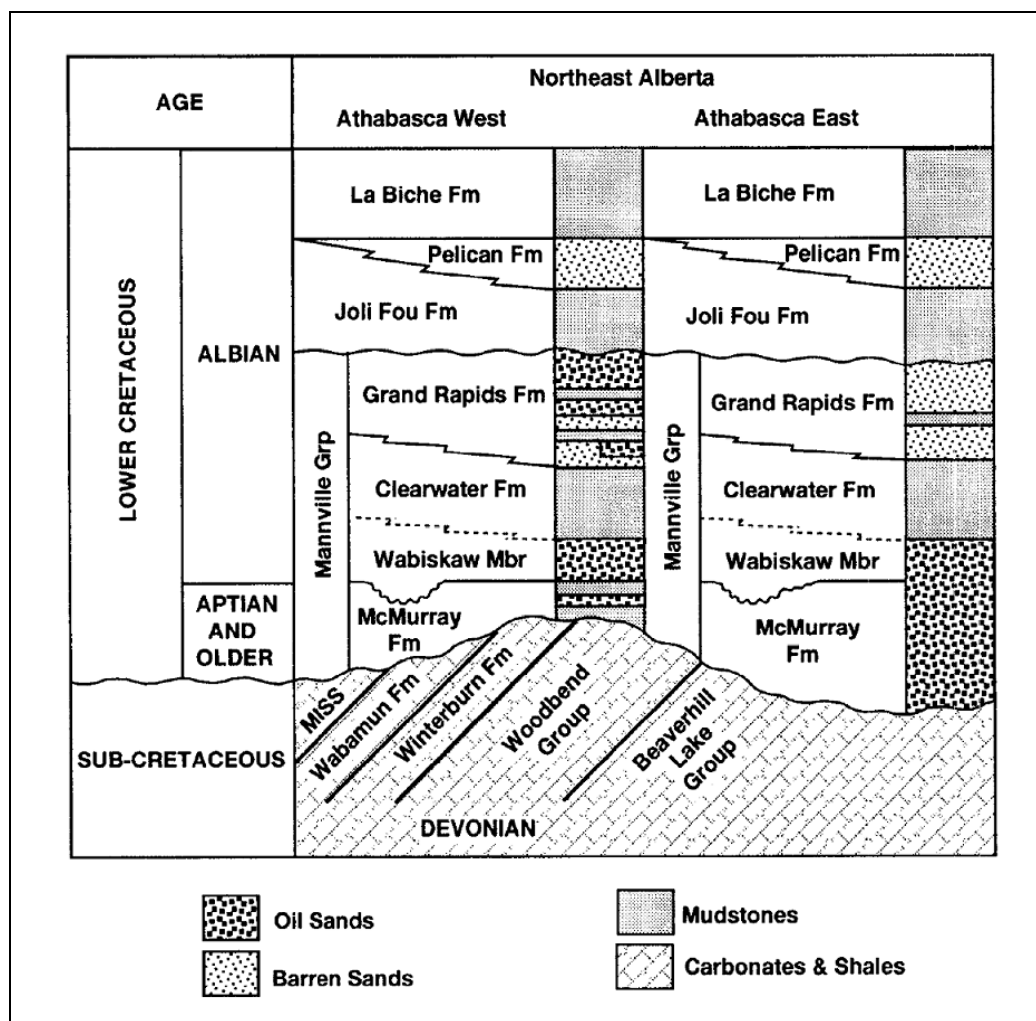


Figure 6-3: The regional stratigraphy of the Athabasca oil sands (modified from Wightman et al., 1995).

The Grand Rapids formation is divided into three main subunits of the upper, middle and lower Grand Rapids. These subunits are separated by shale and silt intervals. The uppermost unit, called the Upper Grand Rapids, is mainly formed of fine to medium grained sand and is bitumen saturated. This subunit forms the zone of interest. The Joli Fou shale which overlies the upper Grand Rapids, acts as the cap rock to the reservoir.

6.2 Crosswell seismic data

Two vertical wells are used as the source and receiver wells. The separation between the source and receiver wells at the surface is 140 meters and the zone of interest is located at the depth interval of 188 m to 218 m.

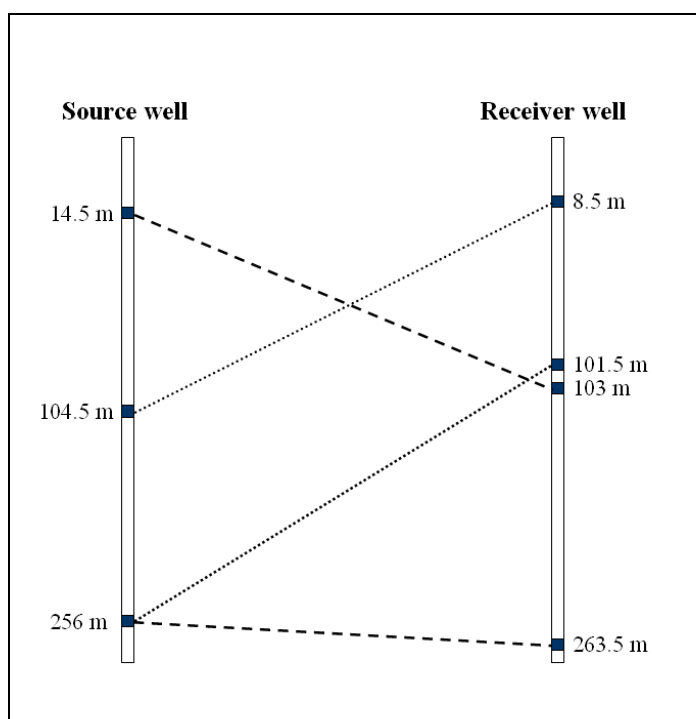


Figure 6-4: Crosswell survey geometry (schematic).

Clamped vibrators type sources and single clamped geophones are used in the survey. The source and receiver spacing is 1.5 meters in both wells, which provides a finely sampled dataset. The crosswell survey geometry is shown in Figure 6-4. The diagram shows that the shallow recorders (63 receivers from depth of 8.5 m to 101.5 m) have only recorded the signal from deeper sources, while the deeper recorders (108 receivers from depth of 103 m to 263.5 m) have recorded the signal from the entire source array.

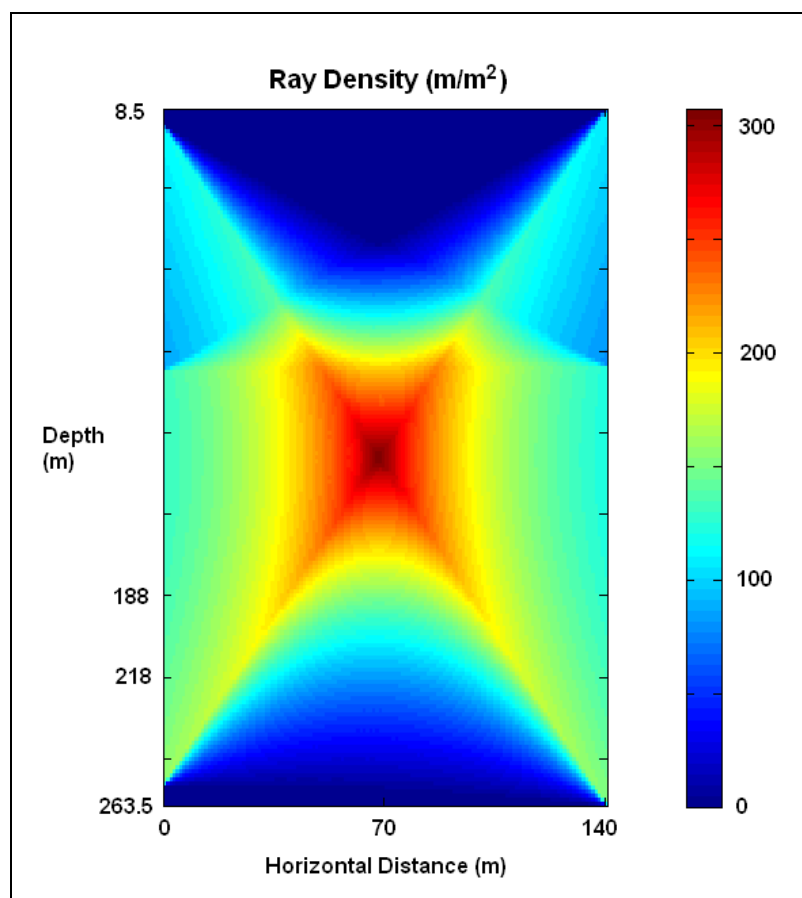


Figure 6-5: Ray density map (straight ray direct arrivals).

The density of the direct arrival rays, calculated using straight rays, is shown in Figure 6-5. The scale represents the total length of rays per unit cross sectional area. Total of 171 receiver gathers have been recorded. The frequency content of the data ranges from 30 Hz to 600 Hz with the dominant frequency of 420 Hz. The sampling interval is 0.5 ms (sampling frequency of 2000 Hz) which allows the Nyquist frequency of 1000 Hz.

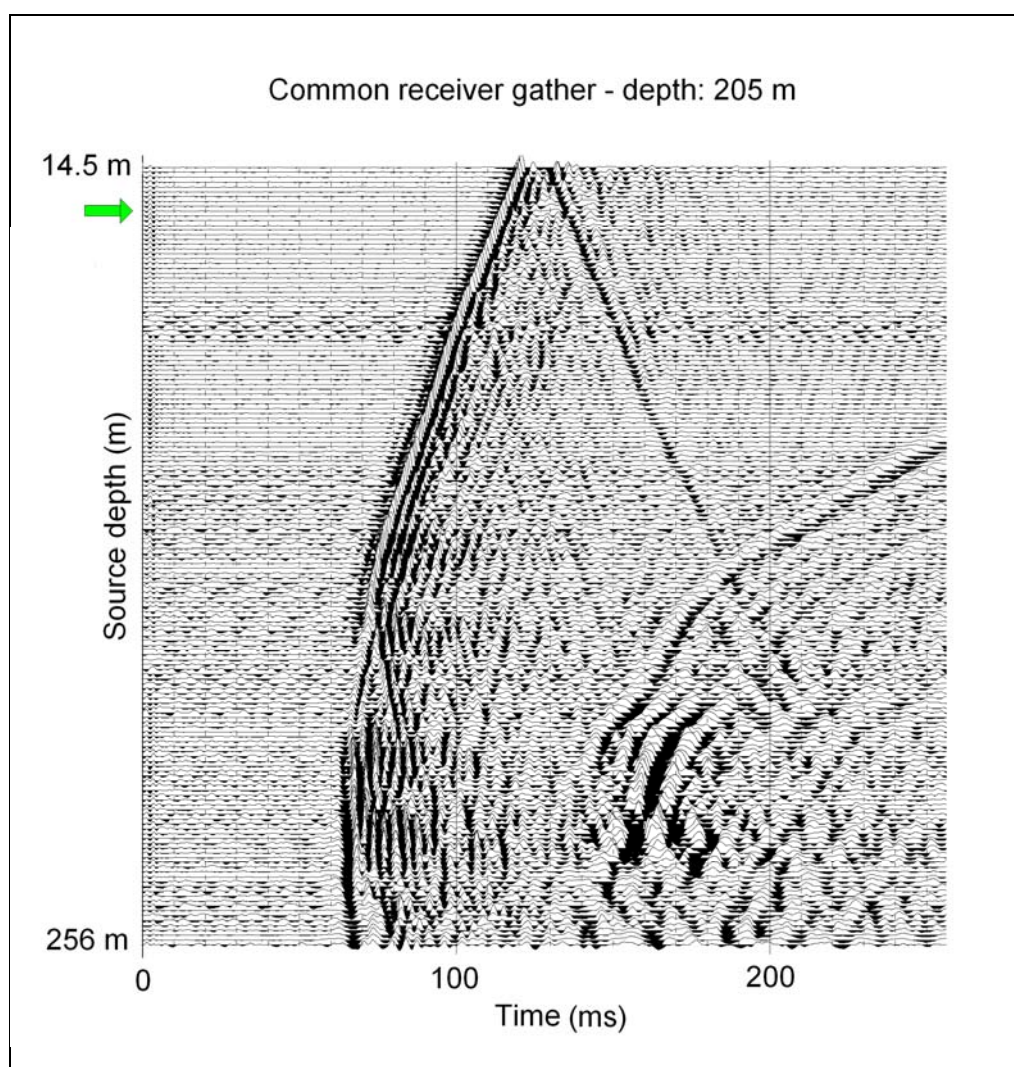


Figure 6-6: Common receiver gather, receiver depth: 205 m.

Figure 6-6 shows a common receiver gather from a receiver at the depth of 205 m. Travel times, which can be obtained by identifying and locating the arrivals, will be used in travel time tomography. Once the travel times are known, the signal can be isolated on the trace by using a window of a specific length. The frequency content of the signal is then calculated through Fourier transform. The centroid frequency is calculated from the resulting amplitude spectrum using equation (4.12).

Figure 6-7 shows a signal (direct arrival) and its amplitude spectrum taken from the trace recorded for a ray travelled between the source at the depth of 28 m and the receiver at the depth of 205 m. The trace is marked with the arrow in Figure 6-6. The centroid frequency for this signal is 227 Hz which will be used as an input in the attenuation tomography.

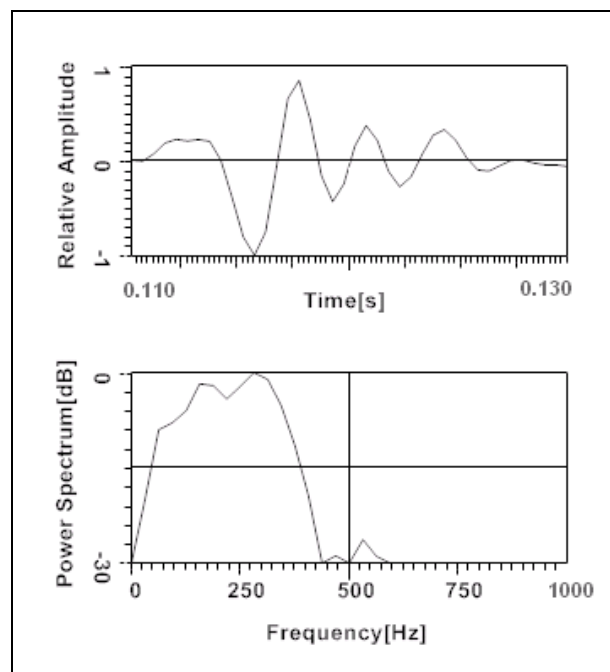


Figure 6-7: Signal (top) and its amplitude spectrum (bottom).

6.3 Well data

Data from 17 wells around the crosswell profile, including the source and receiver wells, are used for the geostatistical construction of the reservoir data.

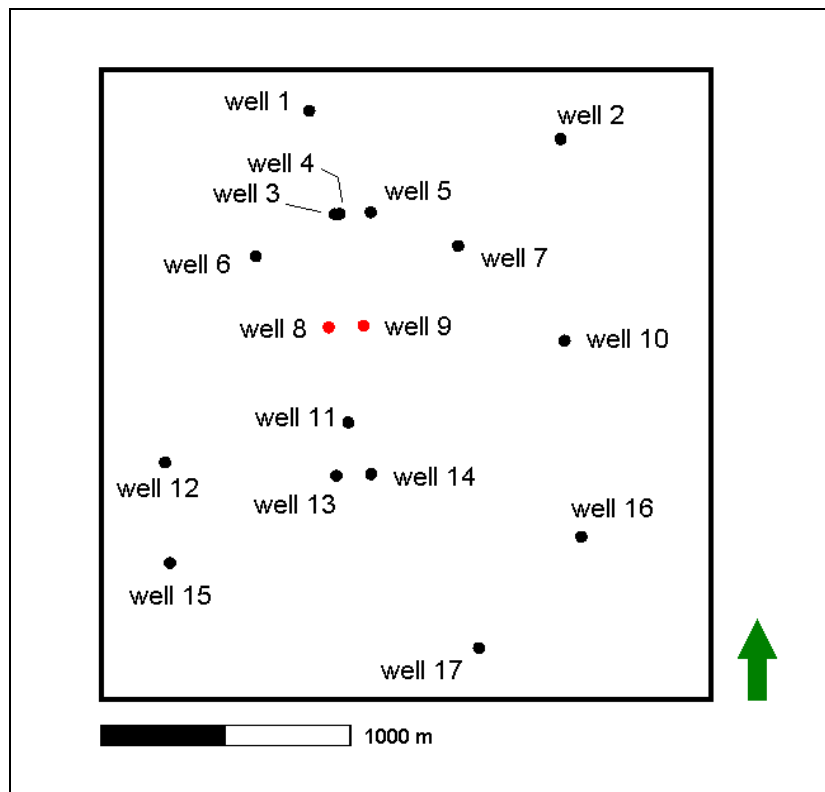


Figure 6-8: Base map. The configuration of the available wells relative to the source and receiver wells (wells 8 and 9, respectively).

The areal distribution of the wells is shown in Figure 6-8. Wells 8 and 9 are the source and receiver wells, respectively. The areal distribution of the wells allows the generation of three dimensional models from available core and log data of these wells. The data availability is summarized in Table 6-1.

Well	Log data			Core data		
	Sonic	GR	Density	Porosity	Permeability	Water saturation
1	x	x	x			
2		x		x	x	x
3		x	x			
4	x	x	x			
5		x				
6	x	x	x	x	x	x
7	x	x	x	x	x	x
Source well 8	x	x	x	x	x	x
Receiver well 9	x	x	x	x	x	x
10	x	x	x			
11	x	x				
12	x	x	x	x	x	x
13	x	x	x			
14	x	x	x	x	x	x
15	x	x	x			
16				x	x	x
17	x	x	x			

Table 6-1: Available core and log data.

Gamma ray log data as well as core measurements of porosity, permeability and water saturation will be used to estimate the reservoir parameters. Figures 6-9 and 6-10 show the core and log data for the source and receiver wells at the depth interval of interest. The high gamma ray readings at the top of the upper Grand Rapids represent the Joli Fou shale which forms the cap rock.

Core data suggest that there is a water zone near the top of the reservoir. The data also illustrate that the correlation between porosity and permeability is not very strong.

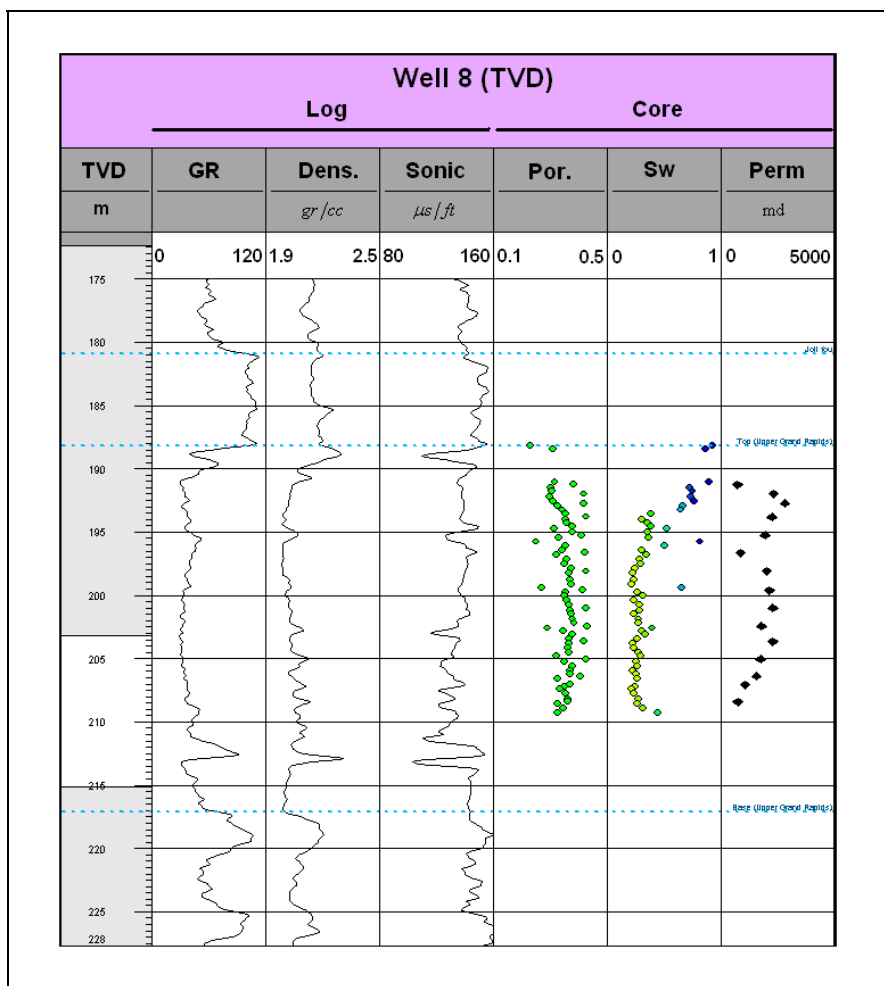


Figure 6-9: The log and core data available at the source well (well 8).

6.4 Tomography

The profile between the source and receiver wells is divided into 1 m thick layers in order to perform the travel time tomography using the Chebyshev polynomials technique. The resulting velocity tomogram is shown in Figure 6-11. The well logs on the sides of the tomogram show the velocity calculated from the sonic log and the velocity estimated from crosswell tomography.

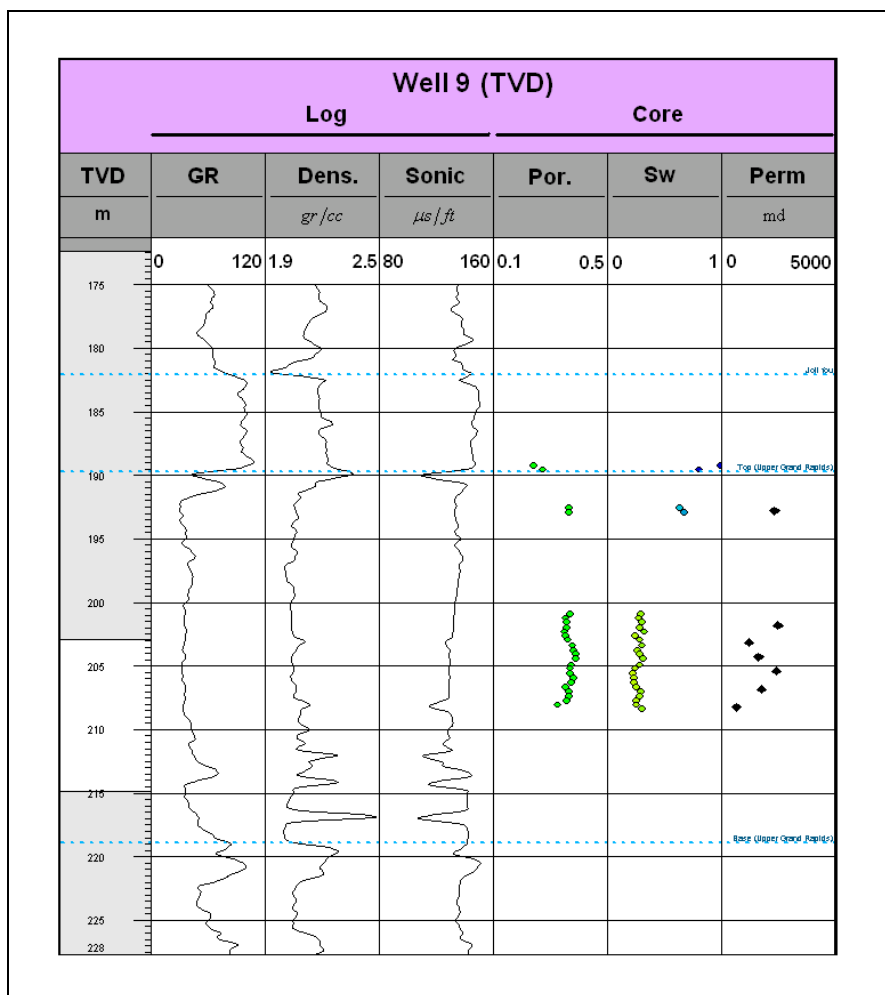


Figure 6-10: The log and core data available at the receiver well (well 9).

The sonic log frequency is much higher than the frequency of the crosswell seismic data. Within the zone of interest, which is saturated with bitumen and water, the sonic velocity is greater than the crosswell seismic velocity. This is in agreement with previous observations as shown in Figure 6-12 (Schmitt, 1999). This phenomenon is called the velocity dispersion, and the medium is called dispersive. As mentioned in Chapter 2, velocity changes with frequency in dispersive media.

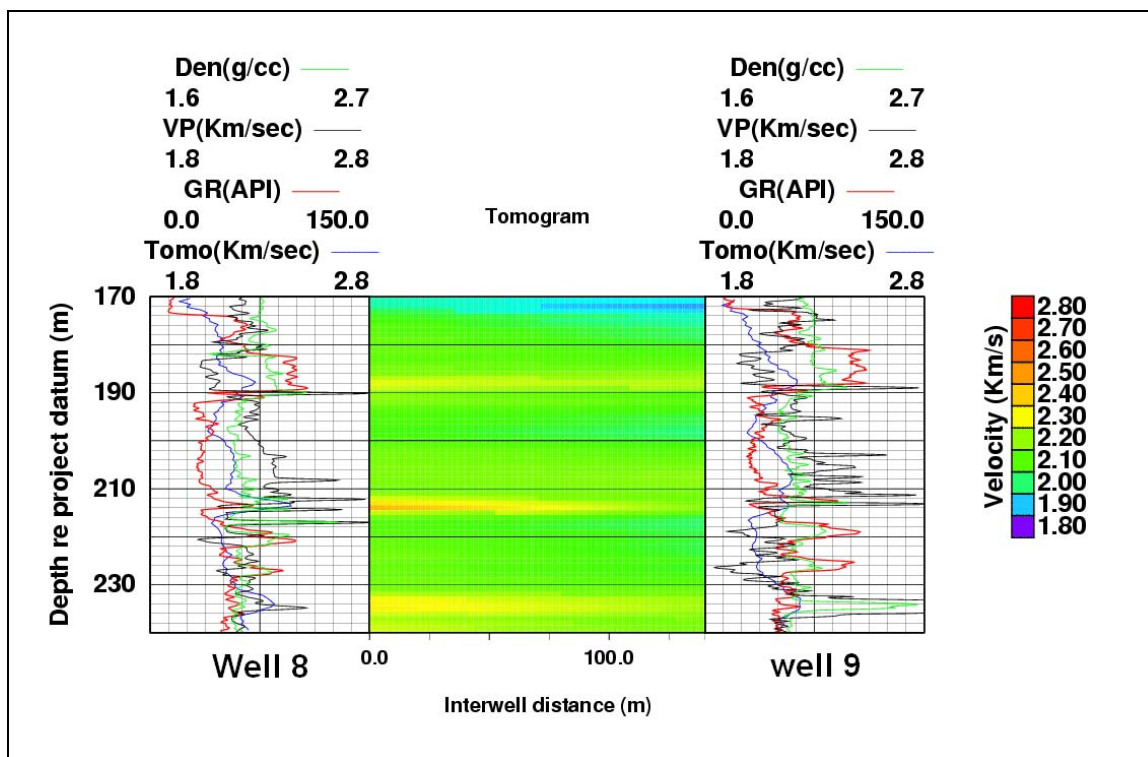


Figure 6-11: The velocity tomogram. The velocity dispersion observed at the well bore is because of the difference between sonic and crosswell seismic frequencies.

When the velocity increases with frequency, the dispersion is called inverse dispersion and it is a characteristic of the homogeneous viscoelastic media. On the other hand, in isotropic elastic media, velocity decreases with frequency and the dispersion is called normal (Bourbié et al., 1987). The reservoir of interest in the current study is filled with viscoelastic fluids and demonstrates inverse dispersion effects as expected.

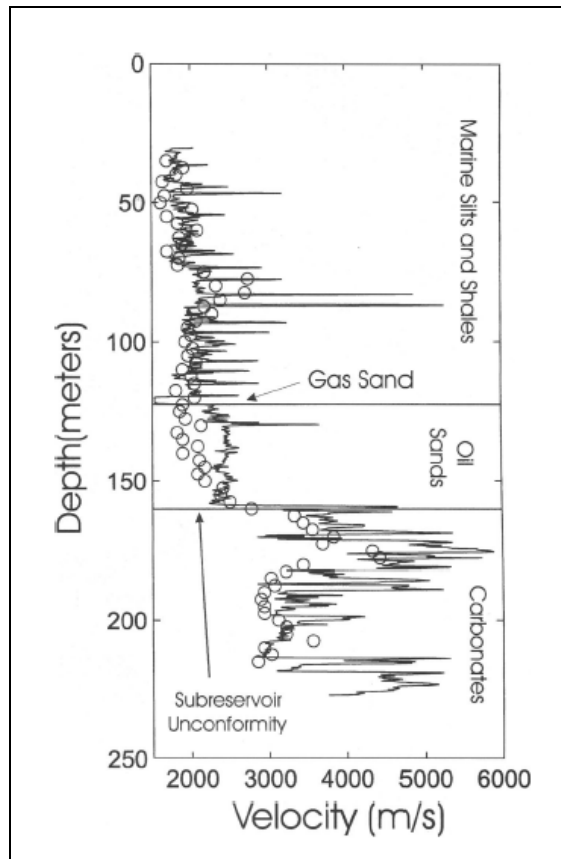


Figure 6-12: Velocity dispersion observed at the oil sands interval. Circles represent VSP derived interval velocities and the curve shows the sonic log velocity. (from Schmitt, 1999).

In order to complete the attenuation tomography, each of the layers, defined in the travel time tomography, is divided into 140 cells, 1 m by 1 m in size each. The tomography is then carried out using the pixilated tomography technique. The output is an attenuation coefficient tomogram shown in Figure 6-13.

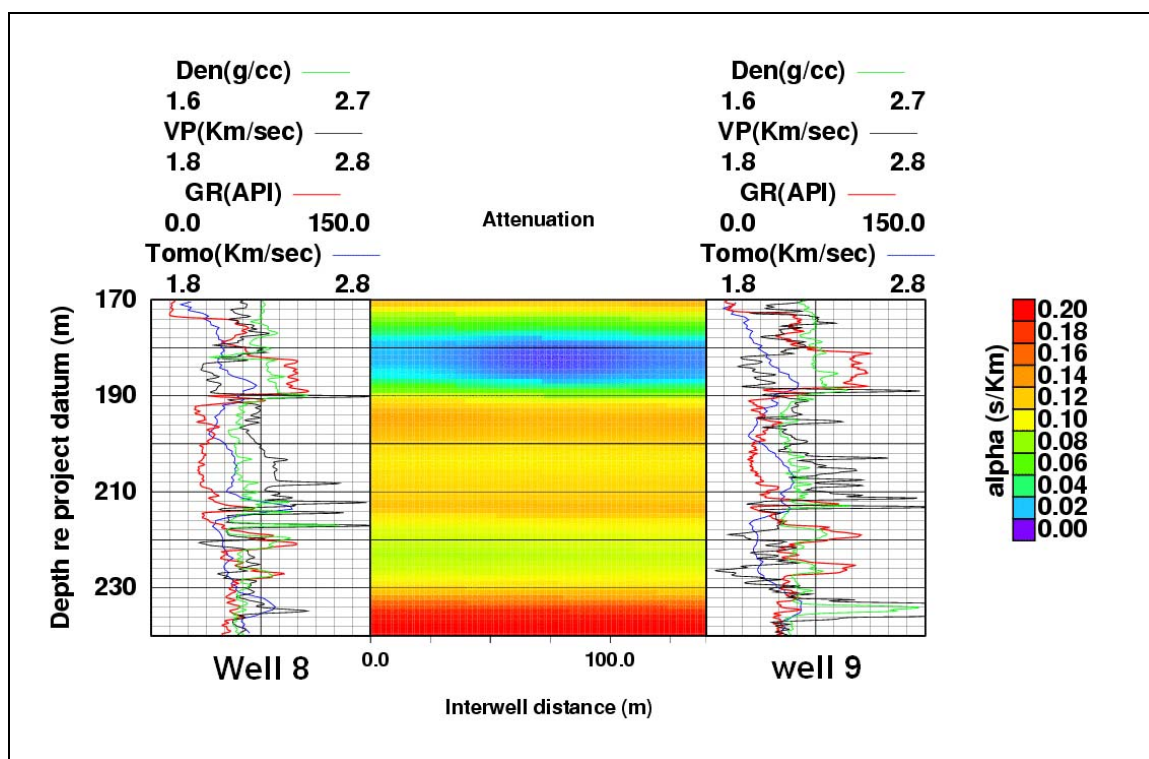


Figure 6-13: The attenuation tomogram.

Knowing the velocity of each cell (from travel time tomography), the attenuation coefficient values are converted into Q using equation (5.9). The resulting Q tomogram is shown in Figure 6-14. Figure 3-3 shows that at lower viscosities, close to viscosity of water (1 cp), saturated rocks act elastically and show higher Q values or lower attenuations. The zone of distinctly high values of Q above the zone of interest is an indicator of water saturated Joli Fou shales. Unlike the attenuation and Q tomograms, the velocity tomogram does not highlight the cap rock shales above the reservoir. This implies that attenuation or Q tomograms are potential candidates for cap rock studies, such as cap rock integrity analysis, at least in areas where the cap rock is believed to be water saturated shale.

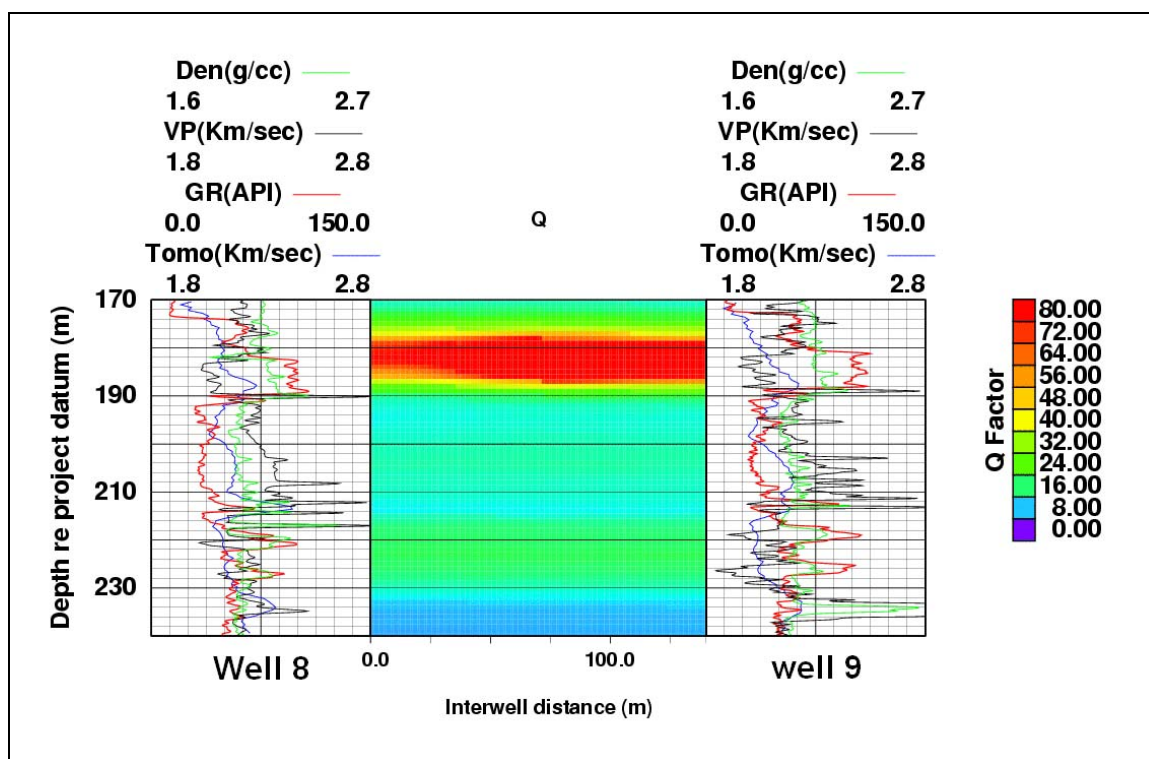


Figure 6-14: Q tomogram. The distinct red zone near the top of the tomogram (depth interval 178 m – 188 m) corresponds to the cap rock shales.

6.5 Reservoir parameters

According to the BISQ equations (3.6 and 3.8) and as mentioned in Chapter 5, in order to establish a direct relationship between Q and viscosity, the other reservoir parameters given in Table 6-2 should be known and therefore are needed as inputs.

One should note that knowledge of the density is not required because quality factor (or attenuation) is not a function of density. If equation (3.8) is substituted into equation (3.6), after some algebraic calculations, the density terms will cancel out from the final equation.

Reservoir parameter	
Porosity	ϕ
Permeability	k
Fluid bulk modulus	K_{fl}
Dry frame bulk modulus	K_{fr}
Dry frame shear modulus	μ_{fr}
Solid bulk modulus	K_m
Characteristic squirt flow length	R

Table 6-2: Reservoir parameters required as input values for BISQ inversion.

Porosity, permeability and water saturation of the rock are measured in the lab from the core samples. Although water saturation is not listed in Table 6-2 and does not appear explicitly in BISQ equations, it will be needed later in this chapter.

No measurement of the other parameters listed in Table 6-2 is available; therefore, they have to be calculated from known rock mechanical properties of the constituents of the rock. This can be done using rock physical relations. It is assumed that the solid frame of the reservoir rock is formed of sand and shale components only, therefore

$$V_{ss} + V_{sh} = 1, \quad (6.1)$$

where V_{ss} and V_{sh} represent the sand and shale volume fractions, respectively, which can be derived from well logs. It is also assumed that the reservoir rock is saturated with a mixture of oil and water with no free gas in the reservoir, which means

$$S_o + S_w = 1, \quad (6.2)$$

where S_o and S_w denote oil and water saturations, respectively. The reservoir rock is therefore assumed to be formed of shale, sand, oil and water. The total volume of each component in a unit bulk volume is given in Table 6-3.

	Component	Total volume
Dry frame	Sand	$(1-\varphi)(1-V_{sh})$
	Shale	$(1-\varphi)V_{sh}$
Pore space	Water	φS_w
	Oil	$\varphi(1-S_w)$

Table 6-3: Total volume of each rock component in a unit bulk volume.

So far the volume of each component in a unit bulk volume of the reservoir rock is known. All rock physics relations, that aim to calculate the effective elastic properties of the reservoir rock, require the previous knowledge of the elastic properties of the constituents as well. The values assumed for these intermediate parameters are summarized in Table 6-4.

As mentioned earlier, the porous media is assumed to be saturated with oil and water only, and no free gas or air exists in the reservoir. The air properties given in Table 6-4 will be used for calculating the empty (dry) frame properties.

6.5.1 Reservoir model preparation

The top and the bottom surfaces of the zone of interest are constructed from the upper Grand Rapids top and base well picks. The reservoir is divided into 30 layers. Since the top and base surfaces are nearly flat, the layers will have a nearly constant thickness of 1 m over the entire reservoir model. A 2.4 km by 2.5 km rectangle defines

the areal extent of the model, as shown in the base map (Figure 6-8). Each layer is discretized into 10 m by 10 m cells which will result in 240 cells in the i direction and 250 cells in the j direction (total of 1,800,000 cells). Using large number of cells allows us to capture the smaller scale reservoir heterogeneities.

Parameter	Value
Bulk modulus (quartz)	$36.6 \times 10^9 \text{ pa}$
Shear modulus (quartz)	$45 \times 10^9 \text{ pa}$
Bulk modulus (clay)	$25 \times 10^9 \text{ pa}$
Shear modulus (clay)	$9 \times 10^9 \text{ pa}$
Bulk modulus (water)	$2.2 \times 10^9 \text{ pa}$
Shear modulus (water)	0 pa
Bulk modulus (air)	$1.5 \times 10^5 \text{ pa}$
Shear modulus (air)	0 pa
Bulk modulus (oil)	$3 \times 10^9 \text{ pa}$
Characteristic squirt flow length	0.5 mm

Table 6-4: The values assumed for the reservoir rock and fluid properties.

6.5.2 Porosity and permeability

Porosity and permeability models are populated for the entire reservoir from the measured values at wellbore locations. There are eight wells with available core measurements of porosity and permeability as summarized in Table 6-1. Permeability estimation is performed independently of porosity. Sequential Gaussian simulation technique is used to generate 10 different realizations for each parameter. The averages of these realizations are used as the estimates of porosity and permeability of the reservoir, which are shown in Figures 6-15 and 6-16, respectively.

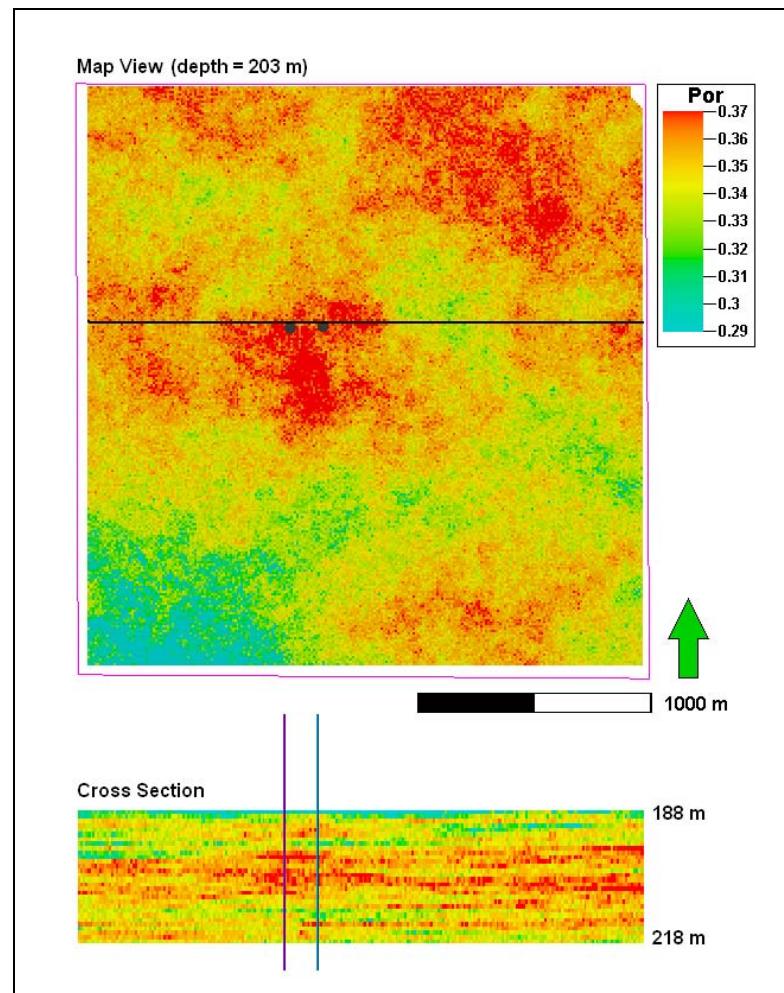


Figure 6-15: Map view (top) and cross section (bottom) of reservoir porosity.

The Figures show the map view of the middle layer ($k = 15$) and the cross section at the vicinity of the crosswell bore holes ($j = 103$). The vertical scale in the cross sectional profiles is exaggerated (20 times). The locations of the crosswell bore holes are shown with black dots on the map view and the vertical lines on the cross section.

According to the maps, the crosswell zone is located in high porosity and medium permeability zone of the model. Although the porosity is very high in the north eastern part of the reservoir, the permeability in this portion is the lowest.

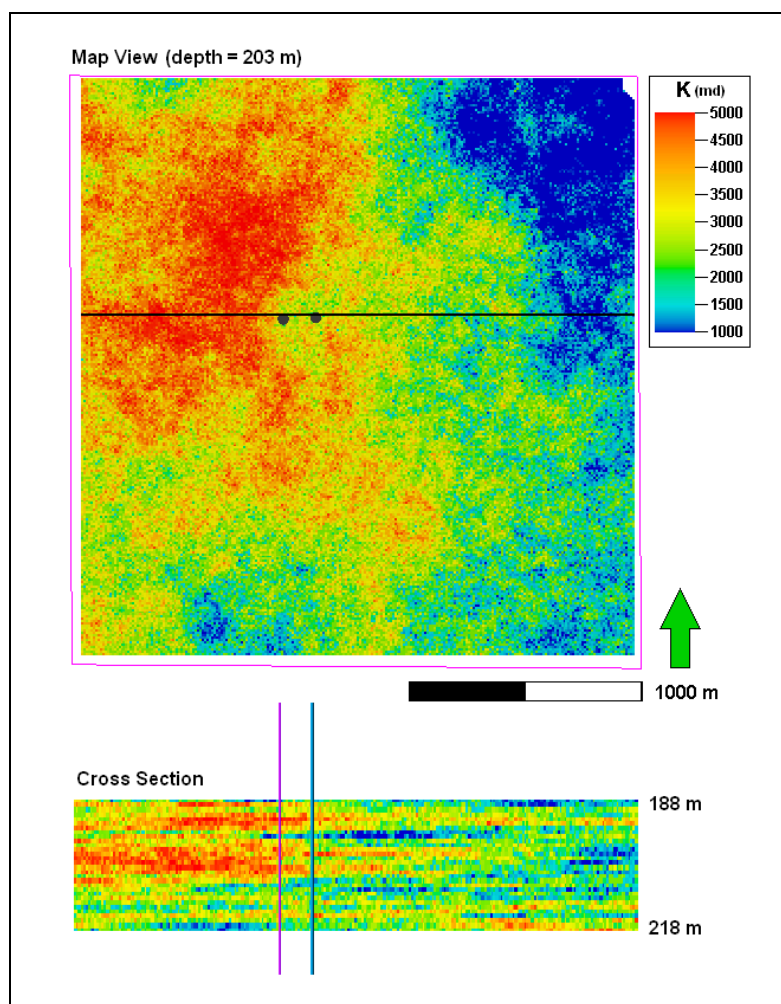


Figure 6-16: Map view (top) and cross section (bottom) of reservoir permeability.

Existing porosity-permeability correlations such as the Kozeny-Carman relation (Mavko et al., 2003) are not able to predict such behavior.

6.5.3 Bulk and shear moduli

Direct measurements of the elastic properties of the material such as bulk and shear moduli are not available at the wellbores; therefore these parameters are calculated using the rock mechanical formulas from the volume fraction of the various constituents of the reservoir rock, together with known elastic properties of each constituent.

Equations (6.1) and (6.2) confirm that knowledge of the volume fractions of the shale and water in the reservoir rock is sufficient for calculating the volume fraction of the other constituents (sand and oil). Therefore, the first step is to calculate V_{sh} and S_w for the entire reservoir model.

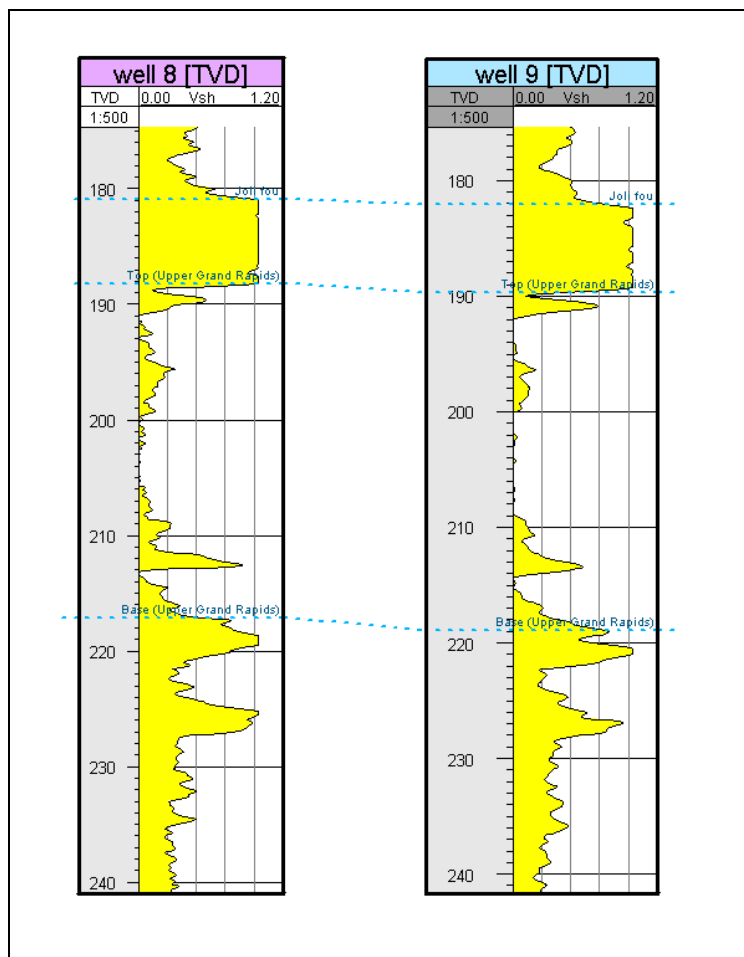


Figure 6-17: Shale volume logs at the source and receiver wells.

The volume fraction of shale (clay minerals) at each well location can be derived from the gamma ray log through the following familiar equation:

$$V_{sh} = \frac{GR_{log} - GR_{min}}{GR_{max} - GR_{min}}, \quad (6.3)$$

GR_{log} denotes the log reading at a certain depth, and GR_{min} and GR_{max} represent the lowest and highest log readings over a depth interval. This depth interval should be selected in such a way that GR_{min} corresponds to a clean sand zone, and GR_{max} corresponds to the shale layer. The shale volumes calculated at source and receiver wells are shown in Figure 6-17.

The gamma ray log is available at 16 well locations (Table 6-1). The V_{sh} logs calculated at these 16 wellbores are used for populating the 3D reservoir shale volume map using the sequential Gaussian simulation technique. Total of 10 realizations are generated and the average is used as the final product.

Figure 6-18 shows a map view and a cross section of the shale volume within the zone of interest. The Joli Fou shale is deposited on top of the zone of interest and is not shown in the cross section, however, it is indicated by high shale volume zone in the logs shown in Figure 6-17.

Water saturation measurements from core samples are available at 8 wells, as listed in Table 6-1. The same statistical modeling technique will be used to generate the 3D water saturation map over the entire area of study. Similar to the other parameters, the average of 10 realizations is considered as the final water saturation model.

A map view and a cross section of water saturation across the zone of interest are shown in Figure 6-19. The cross section suggests that there is a water zone at the top of the reservoir where the water saturation is greater than 80%.

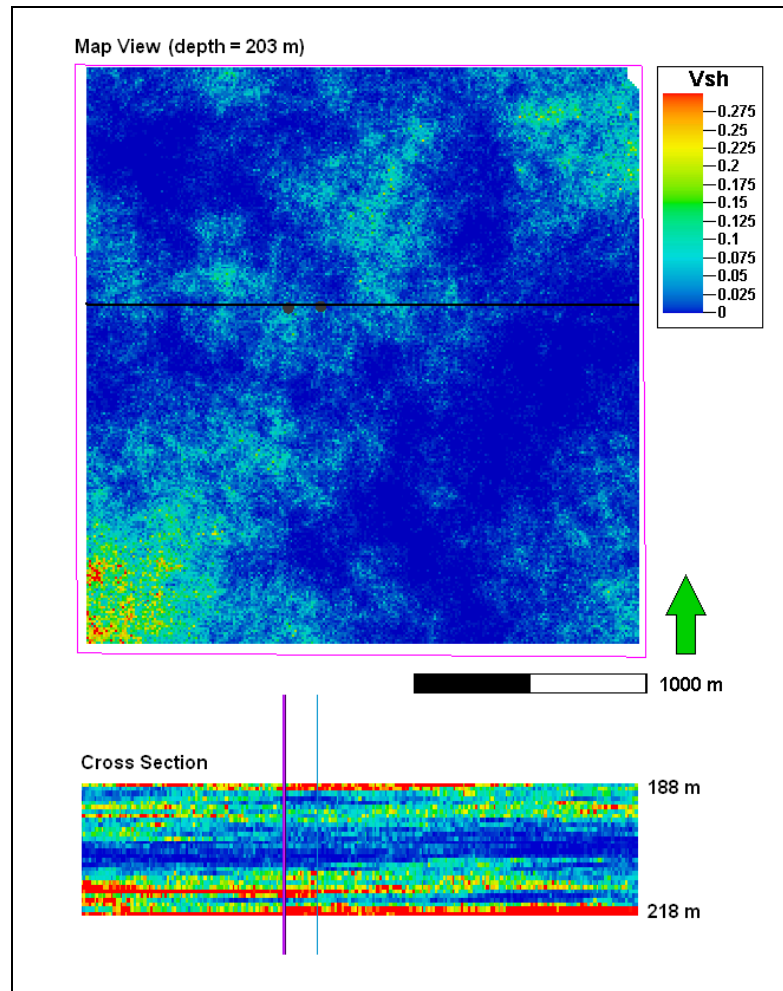


Figure 6-18: Map view (top) and cross section (bottom) of shale volume.

6.5.4 Effect of water

A key consideration in the use of current BISQ theory (equations 3.6 and 3.8) is that it takes only a single fluid viscosity into account. This is due to the fact that BISQ equations are derived with the assumption of single phase fluid flow in the porous media.

In the BISQ theory, it is assumed that the solid frame is the elastic part of the medium and the fluid inside the pores is the only viscous component, and attenuation is observed solely due to the presence of the viscous fluid.

From the graph shown in Figure 3-3, it is known that presence of liquids similar to water in the pore space creates infinitesimal attenuation, which means that the effect of such liquids on seismic response is very close to elastic.

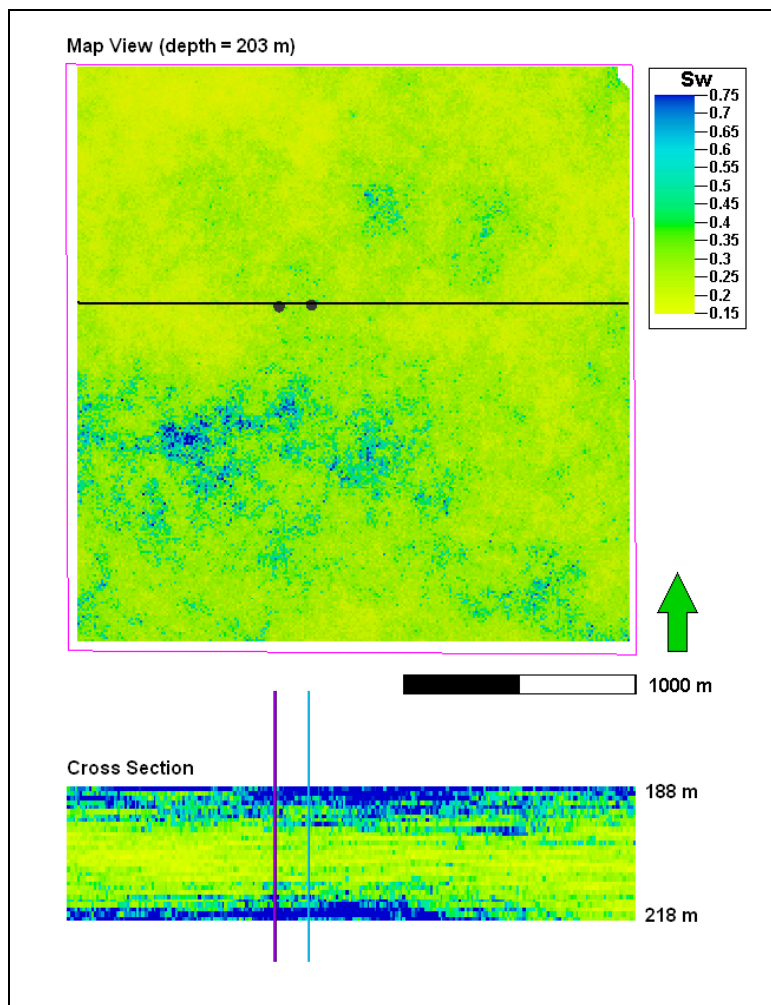


Figure 6-19: Map view (top) and cross section (bottom) of water saturation.

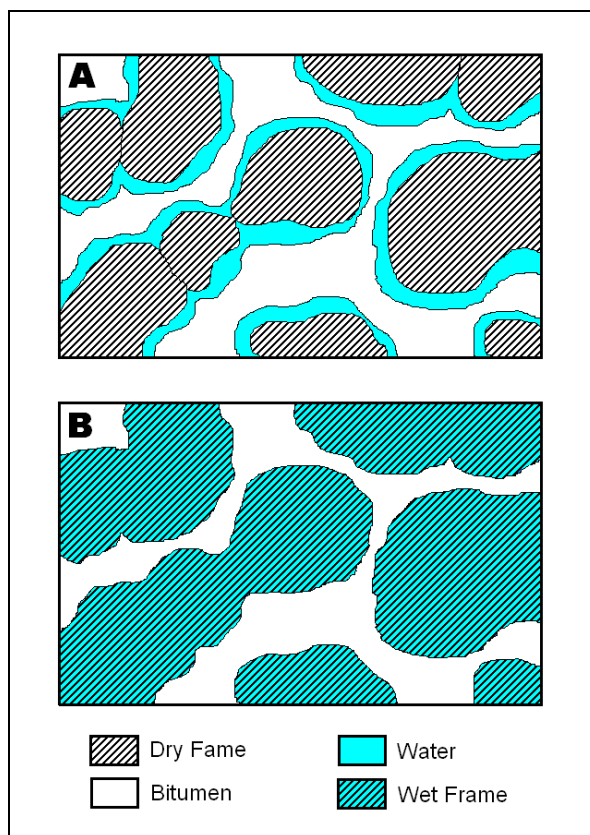


Figure 6-20: Model A: dry frame saturated with water and bitumen. Model B: wet frame saturated with bitumen.

Since water does not add to the total attenuation, or in other words, the seismic response of water is elastic, it can be considered a component of the elastic frame of the rock. This removes one fluid from pore space and adds it to the frame which helps bypass the limitation of the single fluid BISQ equations. Traditionally, rocks are considered to be formed of a dry frame saturated with pore fluids and the elastic properties of such saturated rocks are calculated using fluid replacement models such as Gassmann's equations (Gassmann, 1951). The new modifications require the definition of a new rock mechanical concept, a new frame which contains water phase as well as the solid phase, or a "wet frame". This new frame is in fact the dry frame plus water. Using this new

approach, it can be assumed that the saturated rock is formed of the wet frame filled with heavy oil as opposed to the conventional rock physics models in which the dry frame is filled with water and oil. This concept is illustrated in Figure 6-20. Since water acts elastically, the wet frame is still an elastic component; therefore, the assumption of the BISQ theory (elastic frame filled with viscous fluid) is honoured.

In order to implement the wet frame concept, several modifications have to be applied to the properties of the porous reservoir rock. This is necessary for maintaining the same overall fluid flow and seismic behaviors.

Since water is part of the frame, the new pore space is only filled with the heavy oil; therefore, in order to keep the same volume of heavy oil in the unit volume of rock, the porosity has to change. The new porosity is calculated using the following equation:

$$\varphi' = \varphi(1 - S_w), \quad (6.4)$$

where φ' is the modified porosity. By applying this equation, a portion of the pore space which is filled with water is taken away from the modified pore space and is added to frame. While the total volume of each constituent remains the same, the expressions for the fractional volumes in the wet frame change to the following:

$$V'_{ss} + V'_{sh} + V'_w = 1. \quad (6.5)$$

where V'_w denotes the fractional volume of the water in the wet frame, and V'_{ss} and V'_{sh} represent the modified fractional volumes of sand and shale in the wet frame and are calculated using the following set of equations:

$$\begin{aligned}
 V'_w &= \frac{\phi S_w}{1 - \phi'} \\
 V'_{ss} &= \frac{(1 - \phi)(1 - V_{sh})}{1 - \phi'} \\
 V'_{sh} &= \frac{(1 - \phi)V_{sh}}{1 - \phi'}
 \end{aligned}
 \tag{6.6}$$

Since oil fills the entire pore space of the new frame, the new oil saturation is given by

$$S'_o = 1. \tag{6.7}$$

The total volumes given in Table 6-3 can now be expressed in terms of new and modified parameters; however, their volumes remain the same. The new expressions are shown in Table 6-5.

	Component	Total volume
Wet frame	Sand	$(1 - \phi')V'_{ss}$
	Shale	$(1 - \phi')V'_{sh}$
	Water	$(1 - \phi')V'_w$
Pore space	Oil	ϕ'

Table 6-5: Total volume of each rock component in a unit bulk volume.

Another parameter that needs to be modified is the permeability. The permeability term in the BISQ equations is in fact the permeability of the rock to the viscous fluid.

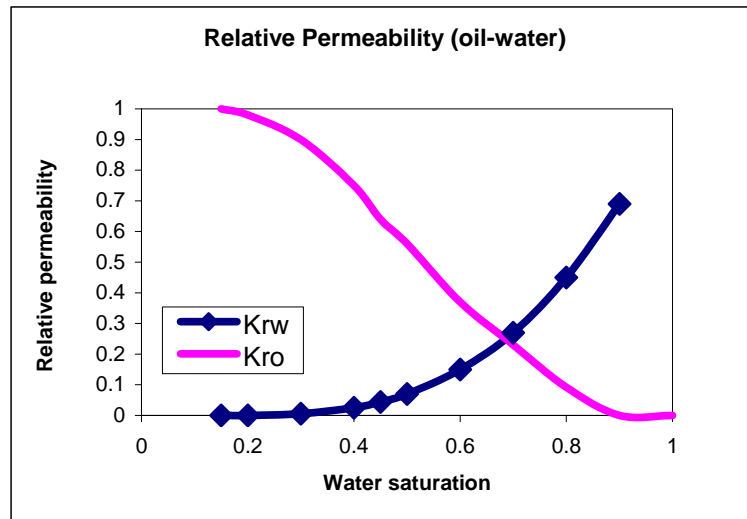


Figure 6-21: Relative permeability curves for water and oil in an oil-water system.

Presence of two liquid phases in the rock (water and oil) reduces the share of each phase from the absolute permeability of the rock. Permeability to each liquid is calculated using the concept of relative permeability. When more than one fluid phase exist in the reservoir rock, an adaptation of Darcy's law (equation 1.1) modified for multiphase flow is used which is given as

$$q_i = \frac{k_i}{\eta_i} \frac{dp_i}{dx}, \quad (6.8)$$

where subscript i represents each phase, and k_i is the permeability to a specific phase i , given by

$$k_i = k \cdot k_{ri}, \quad (6.9)$$

where k is the absolute permeability of the rock, and k_{ri} is the relative permeability of phase i in presence of other fluid phases.

Relative permeability is a function of fluid saturation. For the water-heavy oil system in the current reservoir, the relative permeability curves shown in Figure 6-21 are used. The curves are typical of the heavy oils in the Athabasca region (Edmunds, 2000).

In general if the volume fraction and elastic properties of each component as well as the geometric detail of the distribution of each component are known, the effective elastic properties of the medium can be theoretically predicted (Mavko et al., 2003). However, if the distribution configuration is not known, only the upper and lower limits of the elastic parameters can be estimated, and the actual values lie anywhere between these bounds depending on the geometric details of the mixture.

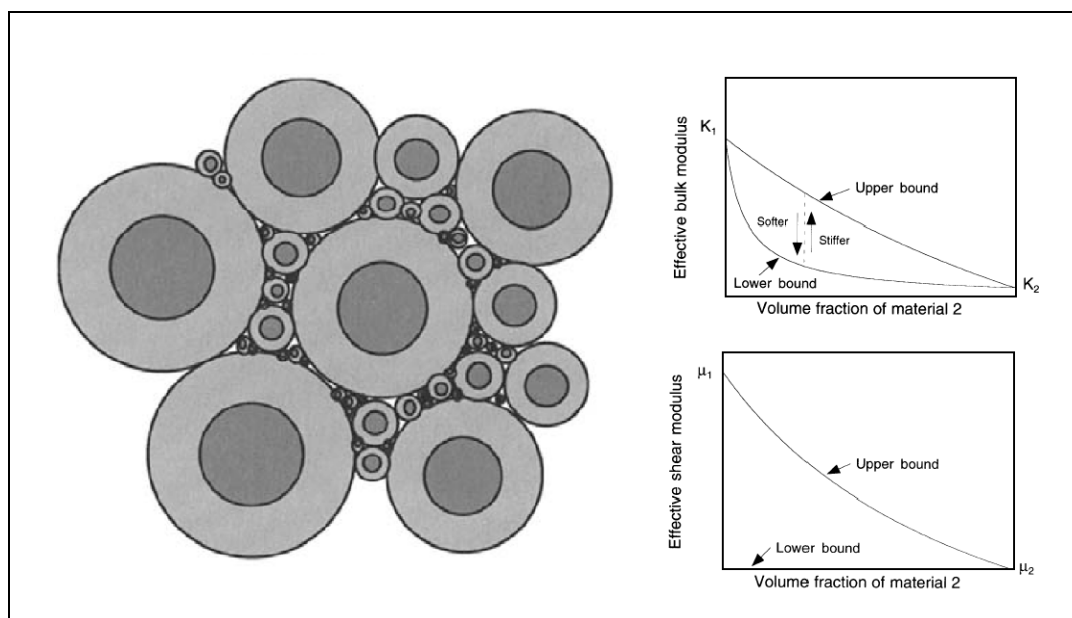


Figure 6-22: The Hashin-Shtrikman bounds of a two phase medium and the corresponding schematic upper and lower bound curves.

Hashin and Shtrikman (1963) derived the equations for the upper and lower limits of the elastic properties for two component systems. The interpretation of the bounds is

shown in Figure 6-22. The upper bound is realized when the softer material forms the core, while the lower bound is realized when the softer material forms the shell.

The Hashin-Shtrikman relations predict the narrowest range between the upper and lower bounds for the mixture of different components which in turn create less uncertainty. The generalized form of the Hashin-Shtrikman equations which can be applied to more than two components (Mavko et al., 2003) is used to calculate the elastic properties of the wet frame.

The equations for the upper and lower limits of the bulk and shear moduli are as follows:

$$\begin{aligned}
 K_{upper} &= f(\mu_{max}) \\
 K_{lower} &= f(\mu_{min}) \\
 \mu_{upper} &= g(h(K_{max}, \mu_{max})), \\
 \mu_{lower} &= g(h(K_{min}, \mu_{min}))
 \end{aligned} \tag{6.10}$$

where the functions f , g and h are given as

$$\begin{aligned}
 f(\mu) &= \left(\sum_i \frac{V_i}{K_i + 4/3 \mu} \right)^{-1} - \frac{4}{3} \mu \\
 g(H) &= \left(\sum_i \frac{V_i}{\mu_i + H} \right)^{-1} - H \\
 h(K, \mu) &= \frac{\mu}{6} \left(\frac{9K + 8\mu}{K + 2\mu} \right)
 \end{aligned}$$

In these equations, subscripts *min* and *max* represent the minimum and maximum value of a parameter between all the constituents, respectively, i denotes each component, and V_i shows the volume fraction of component i .

The elastic properties of the fluid and solid components given in Table 6-4 together with the volumes given in Table 6-5 (or similarly Table 6-3) are used for calculating the bulk and shear moduli of the wet frame K_{w-fr} and μ_{w-fr} , respectively, and the bulk modulus of the wet grains of the frame K_{w-m} . The combination of clay, quartz and water is used to calculate the bulk modulus of the wet grain. In order to calculate the properties of the wet frame, the properties of the air and its respective volume are also included in the calculations. The volume of the air is equal to the volume of the bitumen.

In summary, the following change of variables should be applied to the BISQ relations (equations 3.6 and 3.8) in order to implement the wet frame approach.

$$\begin{array}{llll}
 \text{frame bulk modulus} & K_{fr} & \rightarrow & K_{w-fr} \\
 \text{frame shear modulus} & \mu_{fr} & \rightarrow & \mu_{w-fr} \\
 \text{grain bulk modulus} & K_m & \rightarrow & K_{w-m} \\
 \text{fluid bulk modulus} & K_f & \rightarrow & K_o \quad , \\
 \text{porosity} & \varphi & \rightarrow & \varphi' \\
 \text{permeability} & k & \rightarrow & k_o \\
 \text{fluid viscosity} & \eta_f & \rightarrow & \eta_o
 \end{array}$$

where subscript o denotes oil. The modified BISQ will be used to convert the Q tomogram shown in Figure 6-14 to a viscosity tomogram.

6.6 Viscosity tomogram

The final step in the workflow shown in Figure 5-1 is to use Q values and the reservoir parameters to estimate the viscosity of the heavy oil in the zone of interest. This will be done through the use of the $Q-\eta_f$ curves (Figure 3-3) for each individual cell in

the crosswell grid. Each cell has a unique set of input reservoir parameter; therefore, a different $Q - \eta_f$ curve will be calculated and used for each cell. The nature of such curves implies that for every Q , two viscosity values can be predicted, one from the decreasing (left) side of the curve and another one from the increasing (right) side of the curve. Consequently, the resulting viscosity tomogram is non unique and ambiguous.

The viscosity tomograms, generated using the left and right slopes of the $Q - \eta_f$ curves, are shown in Figures 6-23 and 6-24, respectively. The top 5 meters of the reservoir is not shown in the tomograms because it corresponds to a water zone where the water saturation is greater than 80%. Measured viscosity values at the well locations are not available and as a result, it is not possible to validate the final viscosity estimates.

An observation from the two tomograms is that while the viscosity ranges are different, the viscosity trends in both are the same. Both tomograms show that viscosity is lower at the top and bottom of the reservoir and higher in the middle part.

In the Athabasca region, the observed viscosity values of the heavy oils range between 100,000 cp and 2 million cp. The viscosity tomogram in Figure 6-24, which is generated using the right side of the $Q - \eta_f$ curves, illustrates viscosity values that are closer in range to the typical Athabasca oil sand heavy oil viscosities.

Although lack of real measurements of the viscosity prevents the validation of the final results, these tomograms demonstrate that seismic data have the potential to be used for heavy oil viscosity characterization.

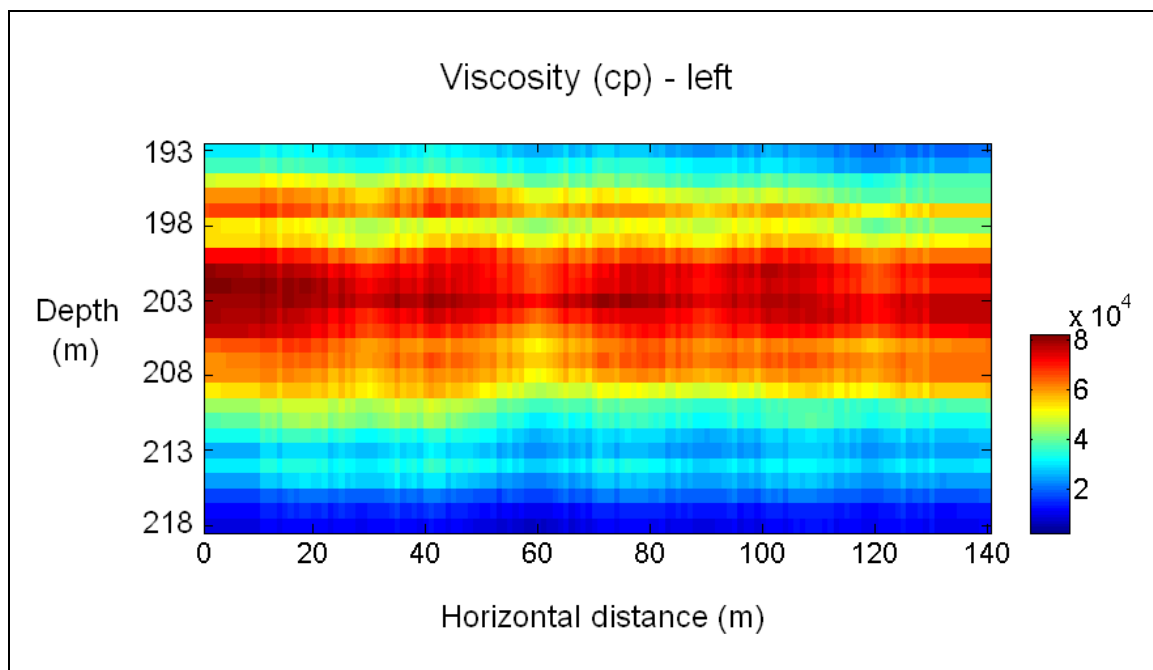


Figure 6-23: Viscosity tomogram generated using the left (decreasing) side of the BISQ curves.

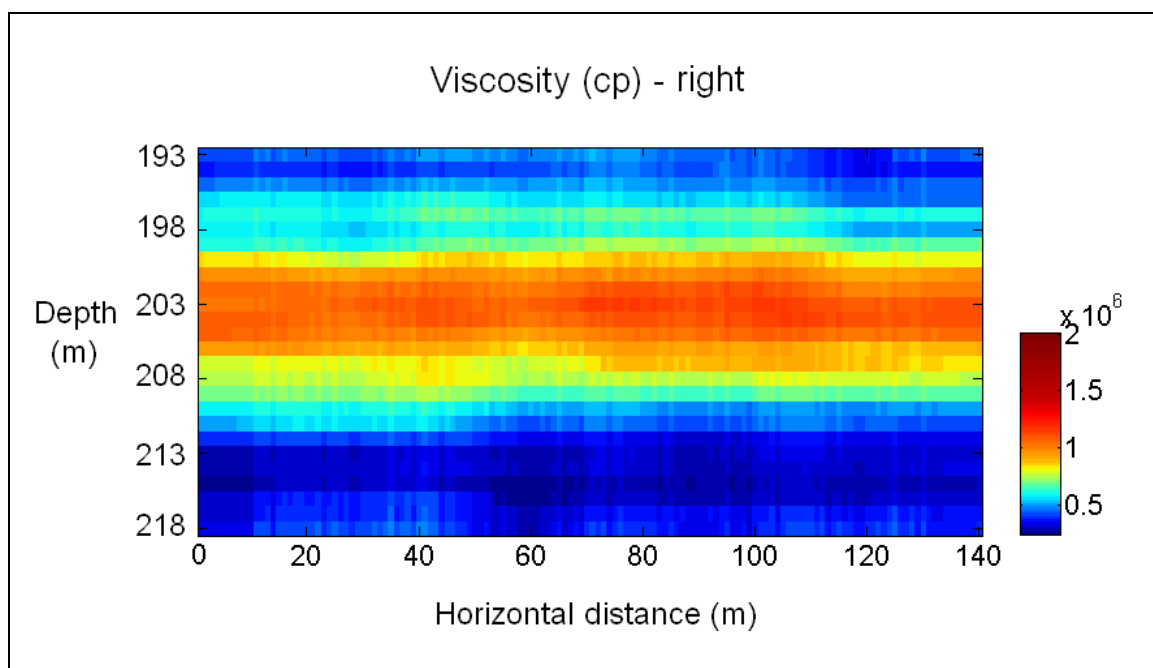


Figure 6-24: Viscosity tomogram generated using the right (increasing) side of the BISQ curves.

Best et al. (2008) showed a similar example of using BISQ relations to predict the viscosity of the oil; however, the measurements are made on the oils with lower viscosities and at higher frequencies. This workflow is not completely mature and more work is required to further develop this workflow and to reduce the uncertainty and remove the ambiguity.

6.7 Sensitivity analysis

Figure 1-2 summarizes the workflow for estimating viscosity from seismic data. It illustrates that the BISQ theory takes the quality factor Q along with the other reservoir parameters, as listed in Table 6-2, and transforms them into a viscosity value. The accuracy of the final viscosity values therefore depend on the accuracy of the input parameters. The error in the final result is not the same for the same relative error in each input parameter. In other words the accuracy of the final product is more sensitive to some parameters than others.

Sensitivity analysis is the study of how the variation in the final result can be related, qualitatively or quantitatively, to the variations in the inputs. To demonstrate the sensitivity of the estimated viscosity values to the accuracy of the quality factor and the reservoir parameters, a base case scenario with fixed input values is established as summarized in Table 6-6. The value of each input parameter is then changed within a specific range ($\pm 20\%$) while the other parameters are kept constant at their base case values. A range of output values is calculated for each varying parameter. The results will be illustrated in a sensitivity plot in which the horizontal axis shows the relative change in each input parameter with respect to the base case value of that parameter and the

vertical axis shows the relative deviation in the estimated viscosities from the base case estimates. For each parameter, the remaining parameters are kept constant at their base case values. The slope of each curve is an indicator of how sensitive the viscosity is to the variation in the corresponding input parameter.

Parameter	Value	Unit
Fluid density	1,000	<i>kg/m³</i>
Fluid bulk modulus	0.8	<i>GPa</i>
Porosity	0.25	
Permeability	2,000	<i>md</i>
Characteristic length	1	<i>mm</i>
Matrix bulk modulus	35	<i>GPa</i>
Matrix density	2,650	<i>kg/m³</i>
Dry frame bulk modulus	1.7	<i>GPa</i>
Dry frame shear modulus	1.35	<i>GPa</i>
Q	10	

Table 6-6: The base case parameters used in the sensitivity analysis.

For the base case given in Table 6-6, the viscosity values extracted from the left (decreasing) and right (increasing) sides of the BISQ curve are estimated to be 2,480 cp and 83,500 cp, respectively. The sensitivity plot for the left and right sides are shown in Figures 6-25 and 6-26, respectively. These plots show that the sensitivities of the left and right sides of the BISQ relation to input parameters are different. Also, it is important to note that that sensitivity plots change with the base case. Use of a different base case will result in sensitivity plots different from those shown in Figures 6-25 and 6-26.

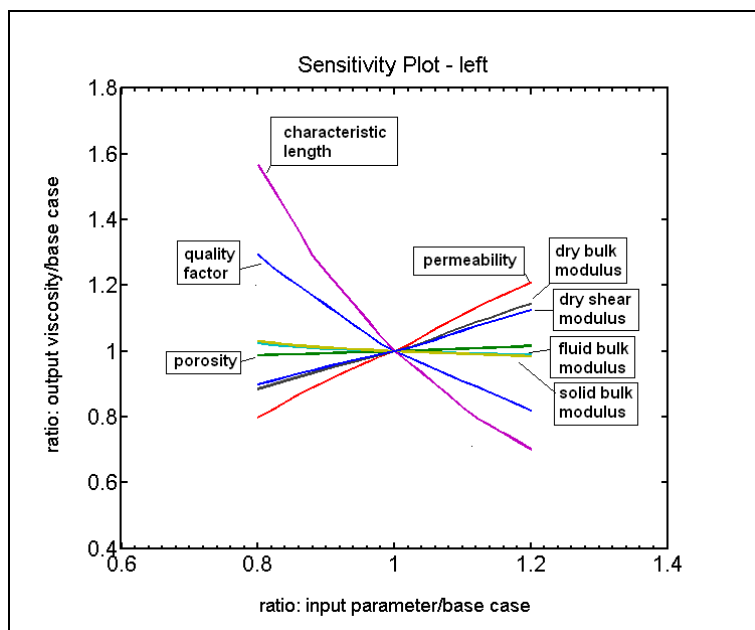


Figure 6-25: Sensitivity plot corresponding to the left side of the BISQ curve.

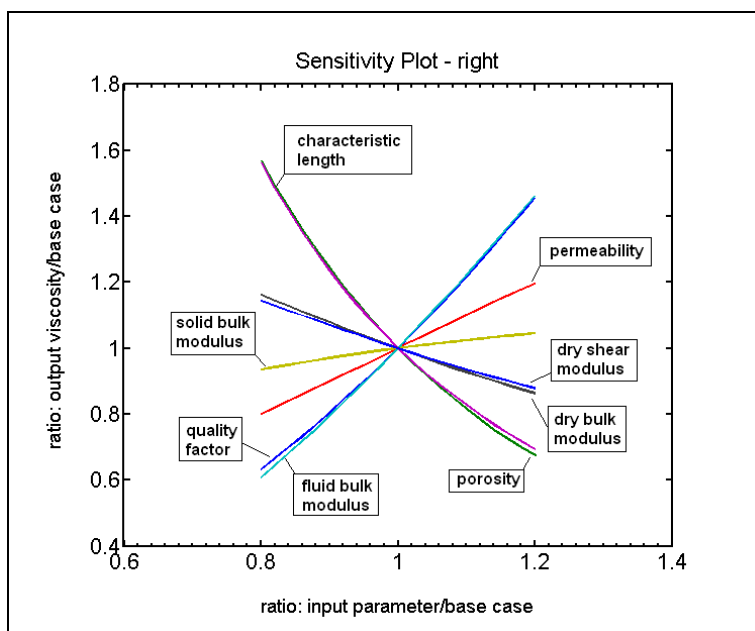


Figure 6-26: Sensitivity plot corresponding to the right side of the BISQ curve.

Chapter Seven: Conclusions

The answer to the question which was asked in Chapter 1 is that although further improvements are needed, the workflow described and tested in this thesis shows that seismic data have the potential to be used for estimating the viscosity of heavy oils.

Contrary to the conventional belief that fluids do not support shear, when dealing with the heavy oils in Alberta, Canada, the shear properties of the fluids should not be ignored. Heavy oils are viscoelastic materials and will cause the porous material to act viscoelastically. The effects of shear properties of heavy oils are reflected in the attenuation of seismic waves; therefore, seismic response is sensitive to the shear character of heavy oils. Attenuation is quantified with a parameter called quality factor Q .

Although viscoelastic models can establish a relationship between quality factor and viscosity, they only take into account the total effective viscosity of the porous media. It makes such models undesirable because their current form cannot be used for estimating the pore fluid viscosity.

On the other hand, poroviscoelastic theories take the solid and fluid properties into account separately. These models relate quality factor not only to fluid viscosity but also to the permeability. Two major attenuating mechanisms are involved and considered in the derivation of the poroviscoelastic models: Biot's mechanism and squirt flow. These two are interrelated and therefore can be expressed in a coupled form as BISQ theory. The behavior predicted by BISQ is observed in the lab measurements as well. At very low and very high viscosities, the overall behavior of the saturated porous rock is elastic. This is because fluids behave elastically at such viscosities. It is only at intermediate viscosities that the porous rock creates attenuation.

Quality factor can be obtained from seismic data through measuring the changes in amplitude, frequency or reflection coefficient. The presented analysis shows that the frequency shift method is the most robust. Also, presence of high frequencies leads to more significant shift in the frequency content; therefore combination of the high frequency seismic data (such as crosswell data) and the frequency shift method for Q estimation yields the preferred technique.

BISQ relations relate the quality factor to parameters other than viscosity and permeability, including porosity, and bulk and shear moduli. Quality factor is independent of density. In order to set up a direct relationship between Q and viscosity only, the other reservoir properties should be known for the entire study area. Such input parameters can be populated using the geostatistical methods from the measured data (logs and cores) at the well locations.

The current version of the BISQ equations only allows the presence of a single fluid phase in the pore space. In cases where water coexists with bitumen in the pores, water can be assumed to be part of the solid frame. The new frame is called the wet frame which is filled with bitumen as opposed to the original system in which the dry frame is filled with water and bitumen. This does not violate the assumptions of the BISQ relations; however, in order to implement the wet frame concept, porosity, permeability, and bulk and shear moduli should be modified.

The Q tomogram, which is the final product of the travel time and attenuation tomography techniques, can be converted to the viscosity tomogram using the established $Q-\eta_f$ relationship; however, the resulting viscosity tomogram is ambiguous because for every given quality factor, there is more than one value for viscosity. These viscosity

values are a few orders of magnitude apart; thus, previous knowledge of the fluid properties in the region can help identify the more realistic viscosity tomogram. Further research is needed to improve the workflow explained in this thesis. Suggestions for possible future work are given in the next section.

7.1 Future work recommendations

7.1.1 Physical models

Small scale models can be used in laboratory in order to have a closer look at the seismic response of various reservoir parameters. One advantage of the physical models is that they provide repeatability. Since the model properties are controlled by the researcher, the effect of each parameter can be carefully analyzed.

Given that the model scale is much smaller than the real reservoir, close attention should be paid to the design of the model and the experiments so that the model response simulates the real scenario. This can be done by taking into account the geometric, static and dynamic ratios between the model and the real case. Some of the parameters that are important are the thickness of the reservoir and over burden relative to the seismic wavelength, source power, source and receiver spacing, and frequency.

One challenge in this experimental approach is to carefully recognize the effects of the frequency. Seismic response is frequency dependent, so if for any reason the frequency in the lab experiments has to be different than the frequency used in the real case scenario (for example, in order to maintain the same thickness to wavelength ratio), the results should be corrected for frequency changes.

7.1.2 Velocity analysis

BISQ relations predict the seismic wave velocities as well as the quality factor (equation 3.5). For the reservoir parameters given in Table 3-2, the variation of P-wave velocity with fluid viscosity as predicted by the low frequency BISQ expressions is shown in Figure 7-1. The velocity trend obtained from theoretical calculation resembles the trend observed in laboratory measurements (Figure 3-4). Viscosity decreases when temperature increases thus moving toward higher temperatures on the x axis in Figure 3-4 is equivalent to moving toward lower viscosities on the x axis in Figure 7-1. The vertical axes can be converted to one another using a v_p/v_s ratio.

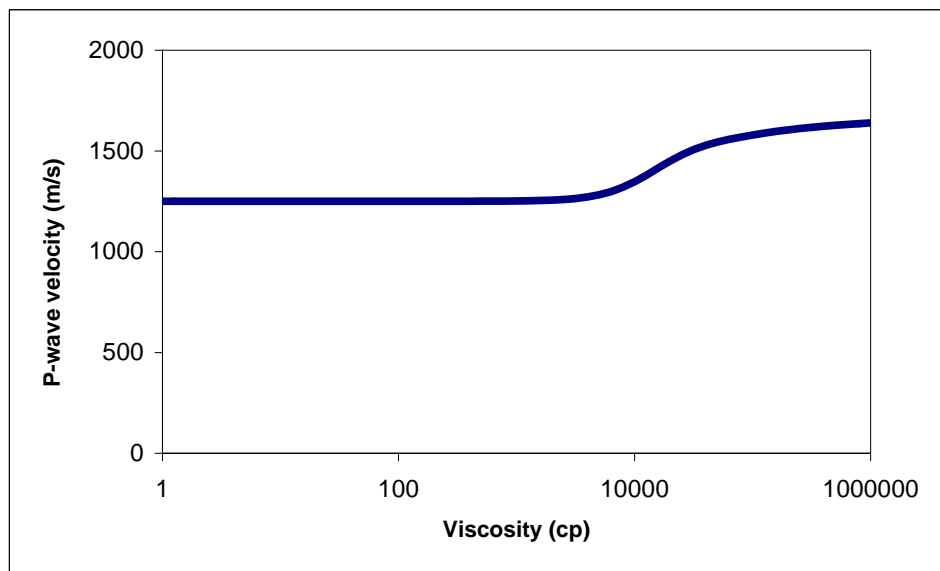


Figure 7-1: Variation of P-wave velocity with viscosity predicted by BISQ theory, computed from the reservoir parameters given in Table 3-2.

A major advantage of using velocity instead of quality factor for predicting the fluid viscosity is that the results are not ambiguous because there is only one value for

viscosity for any given P-wave velocity. One should note that the low and high viscosity limits generate near constant velocities because at such viscosity ranges, the material behaves elastically and variations in the shear properties of the fluids do no influence the seismic response. Such near constant trends create results that are very sensitive and should be carefully studied.

References

- Aki, K., and P. G. Richards, 2002. Quantitative Seismology, Second Edition, University Science Books.
- Batzle, M. L., D. Han, and R. Hofmann, 2006a, Fluid mobility and frequency-dependent seismic velocity - Direct measurements: *Geophysics*, **71**, N1-N9.
- Batzle, M., R. Hofmann, and D. Han, 2006b, Heavy oils - Seismic properties: *The Leading Edge*, **25**, 750-756.
- Batzle, M., R. Hofmann, M. Prasad, G. Kumar, L. Duranti, and D. Han, 2005, Seismic attenuation: Observations and mechanisms: 75th Annual International Meeting, SEG Expanded Abstracts, **24**, 1565-1569.
- Behura, J., M. Batzle, R. Hofmann, and J. Dorgan, 2007, Heavy oils: Their shear story: *Geophysics*, **72**, E175-E183.
- Best, A., C. McCann, and J. Sothcott, 2010, Prediction of pore fluid viscosity effects on P-wave attenuation in reservoir sandstones, in S. Chopra, L. Lines, D. R. Schmitt, and M. Batzle, *Heavy oils: Reservoir characterization and production monitoring: SEG Geophysical Developments No. 13*, 113-119.
- Biot, M. A., 1962, Mechanics of deformation and acoustic propagation in porous media: *Journal of Applied Physics*, **33**, 1482-1498.
- Bourbié, C. T., O. Coussy, and B. Zinszner, 1987, *Acoustics of Porous Media*: Gulf Publishing Co.
- Carcione, J. M., 2007, *Wave Fields in Real Media - Wave Propagation in Anisotropic, Anelastic, Porous and Electromagnetic Media*: Elsevier.

- Das, A., and M. Batzle, 2008, Modeling studies of heavy oil in between solid and fluid properties: *The Leading Edge*, **27**, 1116-1123.
- Dutta, N. C., and H. Odé, 1979, Attenuation and dispersion of compressional waves in fluid-filled porous rocks with partial gas saturation (White model) - part I: Biot Theory: *Geophysics*, **44**, 1777-1788.
- Dvorkin, J., and A. Nur, 1993, Dynamic poroelasticity: a unified model with the squirt flow and the Biot mechanism: *Geophysics*, **58**, 524-533.
- Dvorkin, J., R. Nolen-Hoeksema, and A. Nur, 1994, The squirt flow mechanism: macroscopic description: *Geophysics*, **59**, 428-438.
- Eastwood, J., 1993, Temperature-dependent propagation of P-waves and S-waves in Cold Lake oil sands: Comparison of theory and experiment: *Geophysics*, **58**, 863-872.
- Edmunds, N., 2000, Investigation of SAGD Steam Trap Control in Two and Three Dimensions: *Journal of Canadian Petroleum Technology*, **39**, 30-40.
- Futterman, W. I., 1962, Dispersive body waves: *Journal of Geophysical Research*, **67**, 5279-5291.
- Gassmann, F., 1951, Über die Elastizität poröser Medien: *Vierteljahrsschrift der Naturforschenden Gessellschaft in Zürich*, **96**, 1-23.
- Han, D., J. Liu, and M. Batzle, 2005, Measurement of shear wave velocity of heavy oil: 75th Annual International Meeting, SEG Expanded Abstracts, **24**, 1513-1517.
- Han, D., Q. Yao, and H.-Z. Zhao, 2007, Complex properties of heavy oil sand: 77th Annual International Meeting, SEG Expanded Abstracts, **26**, 1609-1613.
- Hardage, B., 1983, *Vertical Seismic Profiling*: Geophysical Press.

- Hashin, Z., and S. Shtrikman, 1963, A variational approach to the elastic behavior of multiphase materials: *Journal of the Mechanics and Physics of Solids*, **11**, 127-140.
- Jensen, J. L., L. W. Lake, P. W. M. Corbett, and D. J. Goggin, 2000, *Statistics for Petroleum Engineers and Geoscientists*, Second Edition: Elsevier.
- Krebes, E. S., 2004, *Seismic theory and methods*: University of Calgary.
- Larter, S.R., J. J. Adams, I. D. Gates, B. Bennett, and H. Huang, 2008, The origin, prediction and impact of oil viscosity heterogeneity on the production characteristics of tar sand and heavy oil reservoirs: *Journal of Canadian Petroleum Technology*, **47**, 52-61.
- Lines, L., 1991, Applications of tomography to borehole and reflection seismology: *The Leading Edge*, **10**, 11-17.
- Lines, L., F. Vasheghani, and S. Treitel, 2008. Reflections on Q: *CSEG Recorder*, **33**, 36-38.
- Mavko, G. M., and A. Nur, 1979, Wave attenuation in partially saturated rocks: *Geophysics*, **44**, 161-178.
- Mavko, G. M., T. Mukerji, and J. Dvorkin, 2003, *The Rock Physics Handbook: Tools for Seismic Analysis in Porous Media*: Cambridge University Press.
- Nur, A., C. Tosaya, and D. Vo-Thanh, 1984, Seismic monitoring of thermal enhanced oil recovery processes: 54th Annual International Meeting: *SEG Expanded Abstracts*, **3**, 337-340.
- Poynting, J. H., and J. J. Thomson, 1902, *Properties of Matter*: C. Griffin and Co.
- Quan, Y., and J. M. Harris, 1997, Seismic attenuation tomography using frequency shift method: *Geophysics*, **62**, 895-905.

- Schmitt, D. R., 1999, Seismic attributes for monitoring of a shallow heated heavy oil reservoir: A case study: *Geophysics*, **64**, 368-377.
- Shearer, P., 1999, *Introduction to seismology*: Cambridge University Press.
- Slawinski, M. A., 2003, *Seismic Waves and Rays in Elastic Media*: Elsevier.
- Spenser, T. W., J. R. Sonnad, and T. M. Butler, 1982, Seismic Q - stratigraphy or dissipation: *Geophysics*, **47**, 16-24.
- Toksöz, M. N., C. H. Cheng, and A. Timur, 1976, Velocities of seismic waves in porous rocks: *Geophysics*, **41**, 621-645.
- Udías, A., 1999, *Principles of Seismology*: Cambridge University Press.
- Vasheghani, F., and L. R. Lines, 2009, Viscosity and Q in heavy-oil reservoir characterization: *The Leading Edge*, **28**, 856-860.
- Washbourne, J. K., J. W. Rector, and K. P. Bube, 2002, Crosswell travelttime tomography in three dimensions: *Geophysics*, **67**, 853-871.
- Watson, I. A., K. F. Brittle, and L. R. Lines, 2001, Heavy-oil reservoir characterization using elastic wave properties: *CREWES Research Report*, **13**, 777-784.
- Wightman, D. M., M. N. Attalla, D. A. Wynne, R. S. Strobl, H. Berhane, D. K. Cotterill, and T. Bereznuik, 1995, *Resource Characterization of the McMurray/Wabiskaw Deposits in the Athabasca Oil Sands Area: A Synthesis*: Alberta Department of Energy.
- Wyllie, M. R. J., H. F. Gardner, and A. R. Gregory, 1962, Studies of elastic wave attenuation in porous media: *Geophysics*, **27**, 569-589.
- Zener, C., 1948, *Elasticity and Anelasticity of Metals*: University of Chicago Press.
- Zhou, S., H. Huang, and Y. Liu, 2008, Biodegradation and origin of oil sands in the Western Canada Sedimentary Basin: *Petroleum Science*, **5**, 87-94.